# Mineral Dust Optical Properties for Remote Sensing and Global Modeling: A Review

Patricia Castellanos[1*], Peter Colarco[2], W. Reed Espinosa[3], Scott D. Guzewich[4], Robert C. Levy[3], Ron L. Miller[5], Mian Chin[2], Ralph A. Kahn[3], Osku Kemppinen[2,6,12], Hans Moosmüller[7], Edward P. Nowottnick[8], Adriana Rocha-Lima[10], Michael D. Smith[11], John E. Yorks[8], Hongbin Yu[3]

[1]Global Modeling and Assimilation Office, NASA Goddard Space Flight Center, Greenbelt, MD, USA
[2]Atmospheric Chemistry and Dynamics Laboratory, NASA Goddard Space Flight Center, Greenbelt, MD, USA
[3]Climate and Radiation Laboratory, NASA Goddard Space Flight Center, Greenbelt, MD, USA
[4]Planetary Environments Laboratory, NASA Goddard Space Flight Center, Greenbelt, MD, USA
[5]NASA Goddard Institute for Space Studies, New York, NY, USA
[6]Earth System Science Interdisciplinary Center (ESSIC), University of Maryland, College Park, MD, USA
[7]Laboratory for Aerosol Science, Spectroscopy, and Optics, Desert Research Institute, NV, USA
[8]Mesoscale Atmospheric Processes Laboratory, NASA Goddard Space Flight Center, Greenbelt, MD, USA
[9]Goddard Earth Sciences Technology and Research II, University of Maryland Baltimore County, Baltimore, MD, USA
[10]Physics Department, University of Maryland Baltimore County, Baltimore, MD, USA
[11]Planetary Systems Laboratory, NASA Goddard Space Flight Center, Greenbelt, MD, USA
[12]Now with Meta Platforms, Inc., Menlo Park, CA, USA
**Corresponding Author:* patricia.castellanos@nasa.gov, NASA Goddard Space Flight Center, Code 610.1, Greenbelt, MD, 20771 USA

## Abstract

Dust plays a key role in many Earth system processes and is ubiquitous in the Martian atmosphere. Various intensive field campaigns, laboratory analyses, space-based remote sensing missions, and global modeling efforts aim to characterize dust optical properties. This is a bountiful time for dust scientists, and yet the interpretation of retrievals and comparison to models remains complicated by various conflicting assumptions that are part of each algorithm. For example, the conversion of satellite radiance measurements into products like aerosol optical depth for model evaluation depends upon aerosol properties like particle size and shape that are often prescribed and not part of the retrieval. Conversely, the model calculation of aerosol optical depth often uses different assumptions. The goal of this review is to first document algorithmic assumptions by various satellite retrieval products and models, and identify where there is consistency and where there are differences. In general, the differences documented in this paper reflect uncertainties resulting from incomplete observational characterization of dust aerosols and limitations in our understanding. Second, we note what observations might reduce uncertainties in our knowledge and bring greater consistency to retrievals and models, allowing for a more rigorous and harmonious comparison. The lack of comprehensive and realistic shape models for dust is an outstanding issue, such that closure between forward modeling from particle refractive index, shape, and size and observed optical properties cannot be achieved. Limitations in the computational methods that must be applied to model scattering from complex shapes also makes accurate optical modeling for dust challenging. Field observations indicate the persistence of coarse and giant dust particles at higher altitudes and farther downwind from their source than previously expected. Remote sensing retrieval algorithms based on observations at visible wavelengths have limited sensitivity to these particles and generally do not consider them, although a recent product based on longwave radiances is encouraging. Current measurements of the refractive index of bulk dust and fundamental dust minerology components such as hematite vary widely, inhibiting attempts to represent the variability in dust optical properties and forcing, as expected from different major dust source regions on Earth that have varying mineralogical composition. Some remote sensing retrieval algorithms allow for limited refractive index variability in their inversion solutions through mixing with other fine mode aerosol models, or optimizing the single scattering albedo, but Earth system models surveyed for this paper assume a globally uniform, size-invariant refractive index. Although no Martian dust samples have yet been returned to Earth, remote sensing observations indicate that Martian dust is globally homogenous in composition, and a single spectral refractive index assumption has been widely adopted to represent Martian dust. The lack of comprehensive, statistically representative measurements of dust particle microphysical properties (size distribution, morphology, complex index of refraction spectra, internal structure heterogeneity), and the resulting optical properties, limits our ability to verify the fidelity of these assumptions. A chain of measurements is needed, ranging from characterizing individual dust mineralogy components (e.g., pure hematite and goethite) to *in situ* sampling of complex atmospheric aerosol mixtures. Such results could be applied to both remote sensing retrievals that characterize the optical properties of the total aerosol burden in the atmosphere from total radiance measurements, and to global models that represent the total aerosol burden in the atmosphere by building it up from the balance of individual aerosol sources and sinks.

Keywords: aeolian dust, remote sensing, Earth system modeling, Mars dust

## 1. Introduction

Atmospheric mineral dust mostly originates from wind erosion of soils in the arid and semi-arid regions of Earth and is comprised of rock mineral fragments and other soil constituents. Dust from these land surfaces is entrained into the air when surface wind speeds create enough aerodynamic drag to dislodge and lift particles from the ground. Larger soil particles (diameter > ~40 μm) are lifted against gravity by the force of the wind, whereas direct entrainment of small dust particles (diameter < ~20 μm) is rarely observed due to electrostatic forces and other factors that bind these particles to the surface (Iversen and White, 1982). Instead, smaller particles are detached through bombardment by the larger particles that bounce (or ‘saltate’) along the surface (Gillette et al., 1974; Shao, 2001). Collections of smaller particles are created by shattering or fragmentation of the saltating particles and the bombarded soil grains in a process called sand blasting (Gillette et al., 1974; Gillies, 2013; Shao and Raupach, 1993).

Estimates of global wind-blown dust can vary widely among models due to incommensurate size ranges, but Kok et al. (2021) estimate 5000 Tg yr-1 for particles with geometric diameters below 20 µm, based upon a multi-model ensemble constrained with observations. The majority of emissions originate from the so-called dust belt: arid regions of Northern Africa, the Arabian Peninsula, Central Asia, and China (Yaping Shao et al., 2011). As the most abundant atmospheric aerosol by mass (Kinne et al., 2006), dust plays a significant role in the Earth system, linking land, ocean, atmosphere, and climate (Adebiyi et al., 2023; Kok et al., 2023; Ridgwell, 2002; Schepanski, 2018; Yaping Shao et al., 2011) through various processes such as: transporting essential minerals across ecosystems that can fertilize biological production over land and ocean (Jickells et al., 2005; Mills et al., 2004; Yu et al., 2019), diminishing air quality and increasing health risks for vulnerable people (Kwon et al., 2002; Lee et al., 2014; Liu et al., 2006; Tong et al., 2022; Yang et al., 2022), modulating the global energy budget directly via its interaction with radiation (Li et al., 2004; Yu et al., 2006) and indirectly via its effects on cloud formation, precipitation (DeMott et al., 2003; Sassen, 2002) and surface albedo, mostly from deposition on snow and ice (Painter et al., 2007; Skiles et al., 2018; Yasunari et al., 2015).

Thus, understanding and predicting the spatiotemporal distribution of dust and its properties is crucial for representing fundamental Earth System processes and how they could change under future climate scenarios. As such, the dust cycle and radiative interactions have been incorporated into a number of Earth system models (Huneeus et al., 2011; Kaiser et al., 2019; Pu and Ginoux, 2018). Intercomparison studies show large differences among the global models, particularly for dust deposition and long-range transport (Huneeus et al., 2011; Kim et al., 2019, 2014). Predicting spatial and seasonal patterns of dust optical depth and individual dust outbreaks is difficult as well (Pu and Ginoux, 2018; Wu et al., 2019; Yu et al., 2021). Furthermore, several studies have shown there is uncertainty in the dust direct radiative effect (DRE) related to particle size and composition (Di Biagio et al., 2020; Li et al., 2021; Song et al., 2022).

Space-based remote sensing of dust distributions provides important constraints on the global scale distribution and impact of dust. For example, satellite images can capture a continuous dust plume extending from the coast of North Africa to the Caribbean (Figure 1). These large-scale dust outbreaks transport significant amounts of dust across the Atlantic. Space-based remote sensing of dust distributions dates back to the 1960s and 70s with analysis of ESSA-5 satellite photographs (Prospero et al., 1970) and Very High Resolution Radiometer (VHRR) brightness temperature imagery (Carlson, 1979). This was followed by the identification of dust source regions and empirical estimates of dust amounts from the Total Ozone Mapping Spectrometer (TOMS) aerosol index observations in ultraviolet wavelengths (Ginoux and Torres, 2003; Prospero et al., 2002). The modern satellite era consists of a constellation of active and passive sensors with various observational capabilities for constraining dust concentrations and properties. Many studies have utilized satellite observations to detect and monitor dust storms (Butt and Mashat, 2018), quantify dust transport and deposition (Kaufman et al., 2005; H. Yu et al., 2015; Yu et al., 2019), derive maps of dust sources and dust source functions (Ginoux et al., 2012; Kim et al., 2017), and analyze long-term climate data records of dust optical depth (Voss and Evan, 2019; Yu et al., 2020). These analyses are in turn used to validate and constrain global Earth system models (Zhang et al., 2008).

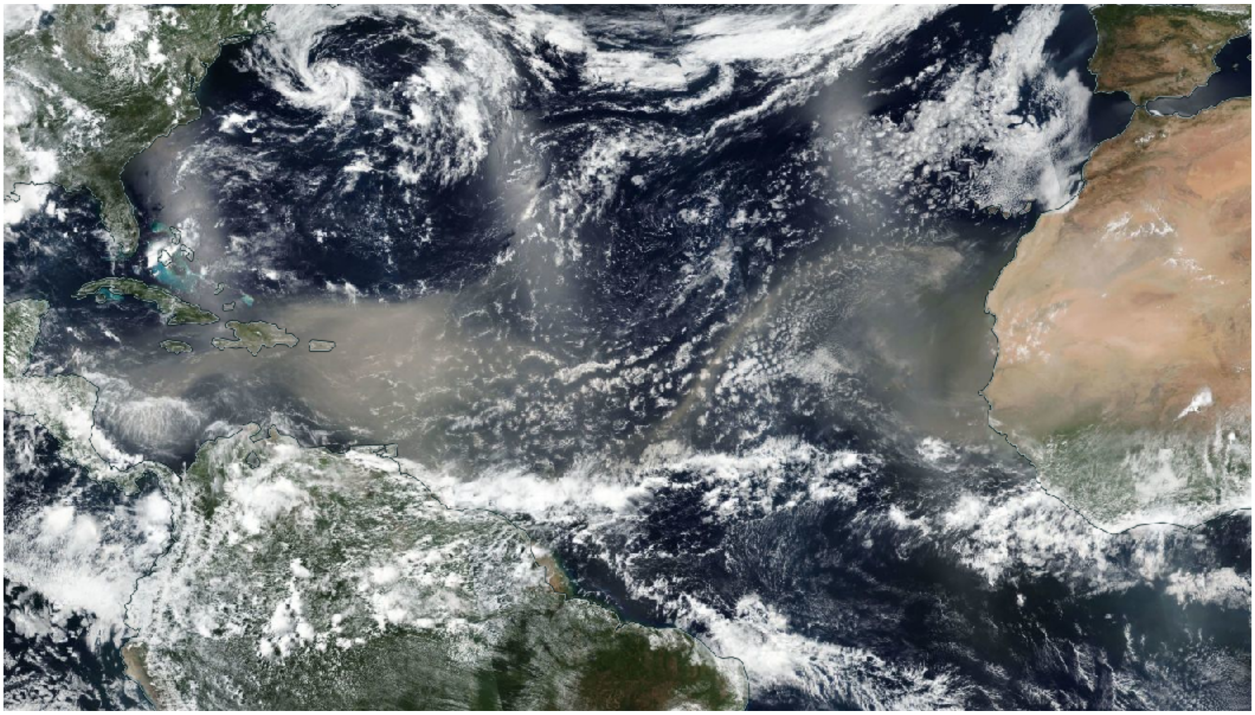

Figure 1. The Visible Near Infrared Instrument Suite (VIIRS) true color image from June 22, 2020 showing a vast dust plume over the Caribbean Sea followed by another weaker dust plume just off the coast of North Africa (image credit: NASA Worldview https://worldview.earthdata.nasa.gov/).

Quantitative remote sensing retrievals of dust properties yield optical constraints, such as aerosol optical depth (AOD) that indicates light extinction, whereas Earth system models track dust aerosol mass distributions. Thus, assimilation of remote sensing retrievals in Earth system models requires a translation from aerosol optical loading to aerosol mass loading, or vice versa, via mass extinction efficiencies. Furthermore, simulation of dust radiative effects, implicit within Earth system models, requires knowing the full dust spectral optical properties (i.e., the dust optical “model”) - the spectral extinction, single scattering albedo, and phase function. All these optical parameters depend greatly on particle microphysical properties – the particle morphology, size, and mineralogical composition. Due to dusts’ complex emission process and heterogeneity in the mineralogical composition of dust source regions, dust particle shape and composition are very irregular with significant consequences for their optical properties. Computational constraints in Earth system models limit the number and complexity of the aerosol tracers transported by the models, requiring that simplifications be made on the microphysical representation, and therefore the optical properties, of dust.

Although dust optical parameters can be constrained to some degree by remote sensing observations, given the indeterminate nature of the remote sensing inversion problem, remote sensing retrievals also require some degree of *a priori* constraint on dust optical properties. The nature of the dust model assumptions, whether it is a limitation on the spectral complex refractive index, size properties, or morphology, depends on the observational capabilities of the sensor. When intercomparing remote sensing retrieval products and Earth system models, many studies overlook the fundamental underlying differences in dust model assumptions and dust-related definitions. This paper seeks to document dust optical properties used across a broad range of remote sensing applications and global Earth system models, with the goal of highlighting where there is consistency and contradiction. To provide context for the assumptions and uncertainties in retrieval and modeling applications, this paper also provides a brief overview of measured *in situ* laboratory measurements and field experiments, and computational methods for deriving dust scattering properties. Several recent comprehensive reviews such as Adebiyi et al. (2023), Kok et al. (2023), Mahowald et al. (2014), Knippertz and Stutz (2014), Formenti et al. (2011), Nousiainen (2009), and Nousiainen and Kandler (2014) treat these topics more thoroughly.

Earth is not the only dusty planet in our solar system; dust is the predominant aerosol in the Martian atmosphere as well. Even more than for Earth, atmospheric thermal and dynamical structures of the Mars atmosphere depend on the distribution of dust. Our understanding of planetary processes on Mars provides insight into the processes that operate on Earth (Kahn, 1989; Smith et al., 2016). Therefore, this paper will also summarize the current understanding of Martian dust optical properties for remote sensing and planetary modeling applications.

The paper is organized into the following seven sections. Section 2 describes laboratory and field measurements of dust. Section 3 gives an overview of numerical methods to calculate dust optical properties from microphysics. Section 4 provides details of dust forward model assumptions in aerosol retrieval algorithms across space-borne and terrestrial remote sensing platforms. Section 5 summarizes dust model assumptions in global Earth system models. Section 6 describes models used to represent dust in Mars remote sensing and modeling. Finally, Sections 7 and 8 provide a summary and a discussion including suggestions for future work.

# 2. *In Situ* Field and Laboratory Measurements of Dust Properties

## 2.1 Particle size distribution

Particle size is fundamental to the climate impact of dust aerosols, including the effect of dust upon radiation, liquid water and ice nucleation, ocean productivity, and heterogeneous chemical reactions that consume ozone and form coatings of secondary aerosol species like sulfates and nitrates on the dust surface (Mahowald et al., 2014). The DRE of smaller particles is generally negative (associated globally with surface cooling), while larger particles contribute positive forcing and warming at both solar and thermal wavelengths (Tegen and Lacis, 1996).

Dust particle size is characterized by a variety of measurement techniques, leading to multiple size descriptors that cannot be directly compared without conversion factors that are often empirical and a source of uncertainty (J. S. Reid et al., 2003a). Size characterization is complicated by the irregular shape of dust particles that challenges complete description by only a few parameters. Microscopic visual analysis gives the particle geometric diameter. This technique is typically the only available methodology to characterize ambient particles of giant size (defined by their diameter greater than 75 μm) that are present in low numbers. The diameter of smaller particles, as detected by bulk particle sizers, are typically reported as equivalent spherical diameters, which are the diameters of spheres that would give the same measurement as the true sample (Jennings and Parslow, 1988; E. A. Reid et al., 2003). For example, an optical particle counter will report the diameter of a sphere that would produce a light scattering signal equivalent to the signal from sampled irregularly shaped dust particles. Meanwhile, a cascade impactor that draws air through a series of progressively finer nozzles and sorts particles by their aerodynamic resistance will report diameters of spheres with equivalent aerodynamic diameter as the sampled irregularly shaped dust particles. Several studies have emphasized the need to distinguish between geometric and equivalent sphere diameters when comparing different measurements or evaluating model simulations of dust with *in situ* observations (Adebiyi et al., 2023; Huang et al., 2021; Kim et al., 2021; J. S. Reid et al., 2003b; Yang et al., 2022). In practice, converting from equivalent sphere diameter to geometric diameter can be difficult and highly uncertain requiring knowledge of the particle density, shape, surface roughness and the index of refraction (Huang et al., 2021; Rosenberg et al., 2012). The goal of this section is to highlight observations that motivated choices made by remote sensing algorithms and modelers and emphasize current uncertainties. Thus, in this section, we will report diameters as they were reported in their respective citations without attempting to normalize to a single size descriptor with the understanding that this notion of particle size is qualitative, in practice being subject to multiple definitions and measurement conventions. In later sections 4-6, where particle size distributions are compared between global models and remote sensing algorithms, all non-spherical diameters are volume equivalent spherical diameters, which correspond to the diameter of a sphere with the same volume as the non-spherical particle. The reader is referred to the recent review of dust size in Adebiyi et al., (2023) for a thorough quantitative overview and comparison of *in situ* dust particle size measurements.

The range of particle size within a dust plume is initially set by the physical processes that mobilize soil particles. After entrainment into a plume, particles are sorted by size through gravitational removal. Larger particles fall out faster and closer to the source due to their smaller air resistance per mass (Tegen and Fung, 1994), decreasing the median particle size along the plume trajectory. The smallest particles are removed mainly by precipitation.

Early measurements of dust particle size near source regions suggested two overlapping log-normal modes: one spanning 1-20 μm diameter, and the other consisting of larger particles (10-100 μm diameter) that were measured under conditions of local wind erosion and moderate to heavy dust loading in the atmosphere (Patterson and Gillette, 1977). d'Almeida and Schütz (1983) measured aerosol particle size in the interior of North Africa at Matam, Senegal and Tombouktou, Mali, during both dusty conditions and intervening periods of relatively pristine air. In the latter case, the distribution of dust particle volume with diameter showed a single mode near 7 μm. During dusty conditions, a second mode with diameters near 40 μm was observed.

(Gillette, 1974)(Gillette et al., 1972)(d'Almeida and Schütz, 1983)(Huang et al., 2021; Rosenberg et al., 2012)(Gillette et al., 1972)(McMurry, 2000; Weiden et al., 2009)(Bullard et al., 2017)(2003b). The emitted dust particle size distribution is derived from size-resolved concentration measurements using two main techniques. According to the *gradient method*, the vertical fluxes of horizontal momentum and dust concentration (i.e., emitted dust) are assumed to be proportional to the vertical gradient of each quantity, derived from measurements at two levels near the surface (e.g., at 1.5 and 6 m height). The diffusivity coefficients relating the flux to the gradient are assumed to be identical for momentum and concentration, if particle settling rates are negligibly small, so that the particles are swept along flow trajectories together with other air components. The emitted flux can be derived from the differences of concentration and horizontal wind speed measured at the two levels along with the surface momentum flux (Gillette et al., 1972) Alternatively, the *eddy correlation method* derives emission by correlating high-frequency fluctuations in concentration and vertical velocity (Dupont et al., 2019; Porch and Gillette, 1977). This method requires a fast-response instrument like a nephelometer to measure rapid variations in concentration. Both methods are less certain for particles with diameters above 10 µm, whose larger mass and inertia cause them to cross flow streamlines, so that the particle and momentum diffusivities are different (Dupont et al., 2019; González-Flórez et al., 2022). Larger particles are also less numerous, requiring longer sampling times to compute eddy statistics resulting in lower temporal resolution (Dupont et al., 2019).

To create a globally integrative constraint for model evaluation, Kok et al. (2017) derived the global mean atmospheric dust size distribution as a maximum-likelihood estimate by combining size-resolved emission measurements from seven studies (Fratini et al., 2007; Gillette, 1974; Gillette et al., 1974, 1972; Rosenberg et al., 2014; Y. Shao et al., 2011; Sow et al., 2009) with model estimates of global size-dependent particle lifetimes. The analytical expression for the composite emitted size distribution was derived by fitting the emission measurements to a function predicted by brittle fragmentation theory (Kok, 2011), assuming that differences in the emitted distribution for different soils, terrain types, and wind speeds are small compared to the systematic error between data sets, and thus that the measurements are globally representative. The Kok et al. (2017) results showed that the emitted dust mass exhibits a single mode centered around 15 μm diameter, noting the comparative absence of dust emissions in the 5-20 μm diameter range in the global models considered in the Aerosol Comparisons between Observations and Models (AeroCom) experiment (Huneeus et al., 2011).

To calculate the global ambient dust size distribution from measurements of the emitted size distribution, Kok et al. (2017) incorporated the dust lifetime calculated by the AeroCom models. Because this lifetime was based upon global removal rates, the derived aerosol size distribution represents a global average along the entire particle trajectory, from emission to deposition. To circumvent the uncertain model estimate of lifetime that is biased low for larger particles, Adebiyi and Kok (2020) formed a normalized ambient dust size distribution by compositing in situ measurements. They concluded that the larger particles neglected by models were even more abundant than the Kok et al. (2017) estimate, although whether the measurements of dust size are sufficient to be globally representative is a remaining uncertainty.

Several field campaigns and routine measurements have corroborated the presence and persistence of larger particles in the atmosphere (Adebiyi et al., 2023). Some studies have found that even giant dust particles with geometric diameter greater than 75 μm can be transported thousands of kilometers from their source (van der Does et al., 2018). This is surprising because theoretical calculations, including simulations in Earth system models, do not simulate this long-range transport, which calls into question whether the life cycle and removal of these particles is fully understood. Maring et al. (2003) analyzed dust measurements near the African coast at

Izaña and downwind over Barbados, noting that the normalized size distribution was largely unchanged during transport for particles diameters up to 7 µm, despite the theoretical expectation that gravitational settling should substantially deplete particles with diameters larger than 2 µm during the ocean crossing.

The unexpected presence of larger particles during transport was clearly revealed during aircraft campaigns that were equipped with well characterized sampling inlets and a Cloud Imaging Probe (CIP) with a sampling volume three-hundred times larger than that of other instruments on board the aircraft (Ryder et al., 2013b). This allowed the ingestion of a greater number of large particles, despite their low ambient concentrations. The high speed of the aircraft relative to the dust plume also resulted in particle incident angles that are more uniformly aligned (opposite the flight direction), allowing the capture of large particles that might otherwise evade the inlet due to their large inertia and oblique approach within the weaker flows at the surface.

During the Fennec campaign in June 2011, the persistence of large particles was observed by aircraft near African source regions (Ryder et al., 2013a). The rate of loss of dust particles was nearly size-independent up to diameters of 20 µm (Ryder et al., 2013a). Downwind within the Saharan Air Layer (SAL), measurements show that particles with 20 µm diameter are as ubiquitous in mass as those at 1 µm, constituting up to 40% of total dust mass (Ryder et al., 2018). Large dust particles were also detected far downwind toward the Caribbean by the Saharan Aerosol Long-Range Transport and Aerosol–Cloud-Interaction Experiment (SALTRACE) in defiance of their expected settling speeds (Weinzierl et al., 2017).

The persistence of larger particles is also demonstrated by ocean measurements of total and size-resolved dust deposition along an east-west Atlantic traverse, where North African dust plumes from disparate upwind sources merge. Ocean sub-surface measurements of deposition avoid challenges of atmospheric deposition instruments, where smaller particles can evade detection by being swept away from the collection surface by deflected air flow. The normalized size distribution is similar in traps at 1 and 3 km depth, suggesting that few particles are displaced horizontally during descent through the water column (van der Does et al., 2016). However, the seafloor sediment traps exhibit a mode at smaller diameters, suggesting sediment reworking by frictionally driven mixing.

Figure 2a shows annual deposition measured in ocean sediment traps beneath the plume as it extends toward the Caribbean (van der Does et al., 2020, 2016); Figure2b-d show the size distribution of the deposited particles. The modal diameter of the deposited particles decreases from 16.4 μm to 9.4 μm downwind along the Atlantic traverse (Figure2b-d) with the preferential removal of the larger particles. At the upwind measurement location (23° W) there is evidence of a secondary mode at larger diameters near 70 μm indicating recent dust mobilization (Figure 2d). This mode is still evident even at the most downwind trap (49.2° W), nearly three-thousand kilometers from the African coast (Figure 2b). Median diameters of the deposited particles are highest during Northern Hemisphere summer (van der Does et al., 2016), when the particles travel within the elevated SAL (Carlson and Prospero, 1972). Figure 2 also shows total dust deposition and its size dependence along the Atlantic traverse as calculated by an Earth System model, the NASA Goddard Institute for Space Studies ModelE2.1 (Bauer et al., 2020). The modeled deposition between 8 and 16 μm diameter falls to near zero across the measurement sites (Figure 2b-d), indicating downwind depletion of dust mass at these diameters. At diameters between 16 and 32 μm, the model is already preferentially depleted at the site closest to the dust source (Figure 2d). This suggests insufficient emission of the largest particles by the model or excessively rapid removal near the source, possibly due to unrealistically weak vertical dispersal that confines the emitted particles too close to the surface. The model total deposition is three times larger than observed at the easternmost trap (23.0° W) with an even larger disparity if the measured total deposition is restricted to the maximum dust diameter considered by the model (D = 32 μm) (Figure 2a). Even at larger diameters outside the model size range (i.e., above 32 μm), the measurements show significant transport to the most downwind trap, where these particles contribute 8% to the total measured deposition. Other global dust models show deposition that is similarly excessive (van der Does et al., 2020).

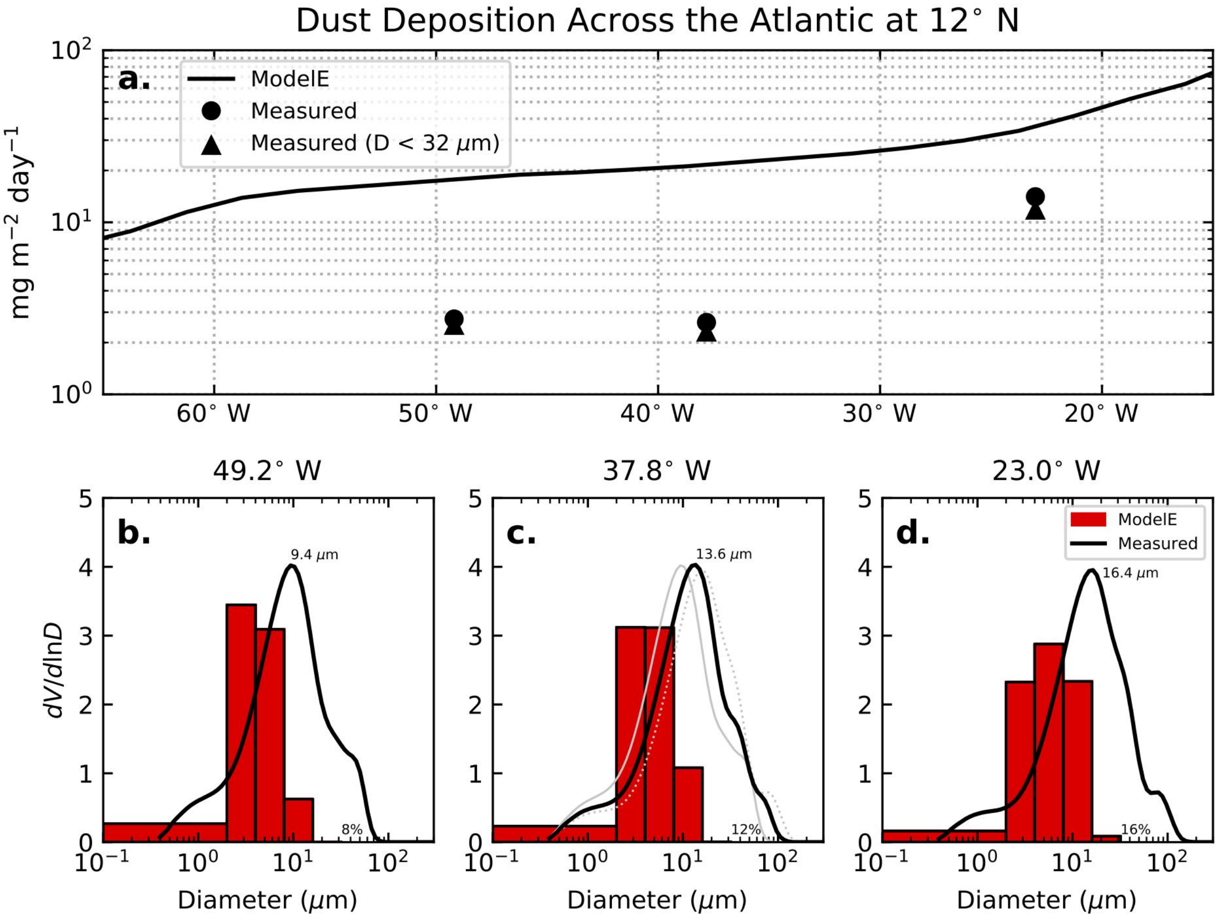

Figure 2. (a) Annual average of dust mass deposition rate (mg m$^{-2}$ day$^{-1}$) along 12° N in the tropical Atlantic Ocean measured from ocean sediment traps near 1200 m depth at 49.2° W,

37.8° W and 23.0° W by van der Does et al. (2020) (circles) and calculated by the NASA GISS ModelE2.1 (solid line). Triangles show measured deposition within the model size range (diameters less than 32 μm) estimated from size-resolved accumulation by van der Does et al. (2016). (b, c, d**)** Normalized volume size distribution of accumulated particle volume from undersea measurements by van der Does et al. (2016) (solid line) and ModelE2.1 (red bars). The measured percentage of particles with diameters larger than the model range (D>32 μm) is given in the lower right. In panel **c**, the measured size distributions of deposited particles at the other two stations (49.2° W and 23.0° W) are plotted in gray for comparison.

The ability to characterize dust size for model evalution is hindered by (Gasteiger et al., 2017)(Huang et al., 2020)(Toth III et al., 2020; Kok and Renno, 2006)(Ulanowski et al., 2007)(Li and Osada, 2007)(van der Does et al., 2018)(Daskalopoulou et al., 2020) a lack of comprehensive field measurements and large uncertainties in existing measurements of large particles. There is no single field-deployable instrument that can cover the full dust size range, and substantial uncertainty exists in piecing together size information from multiple instruments and techniques. Globally distributed surface remote sensing networks such as the Aerosol Robotic Network (AERONET) (Holben et al., 1998) provide routine retrievals of the aerosol size distribution (Dubovik et al., 2002). However, the AERONET size range is constrained to approach zero for particle diameters near 30 μm (Dubovik and King, 2000). Our physical understanding of dust emission is likewise less mature for diameters above 10 μm (Alfaro and Gomes, 2001; Grini et al., 2002; Kok, 2011; Shao, 2001) as field measurements of dust emission flux typically emphasize diameters smaller than 10 μm (Ishizuka et al., 2014), partly because of measurement difficulties at larger diameters related to the separation of flow streamlines and particle trajectories. There are few measurements of dust emission up to 20 μm diameter (Sow et al., 2009). Overall, understanding the persistence of larger particles in the atmosphere, and representing them within models, will require a broader measured size range for emission and ambient concentration to characterize the full life cycle of dust particles.

### 2.2 Particle Shape

The complex dust emission process results in particles with myriad, irregular shapes as revealed by electron microscopy (Buseck et al., 2000; Scheuvens and Kandler, 2014)(Figure 3). These shapes defy simple mathematical representation. Nevertheless, scientists have attempted to summarize dust shape properties through laborious analysis of dust imagery to derive measurements of dust particle dimensions, such as the aspect ratio (AR) that links the particle length and width, and the height to width ratio (HWR). By convention, length is the longest particle axis, while height is the smallest (Huang et al., 2020). The AR that characterizes two dimensions is most reported as it can be estimated from two-dimensional images (e.g., Nakajima et al., 1989; Ryder et al., 2018). However, this introduces the possibility of overestimating volume if the particles are preferentially oriented for stability with their (undetected) smallest dimension normal to the image. The complexity of particle shape means that different definitions are used in the literature for identifying the particle edge and defining particle width for measurements of cross-sectional area (Huang et al., 2020). Collections of non-spherical particles are often represented by fitting the HWR and departures of the AR from spherical shape to log-normal distributions (Huang et al., 2020).

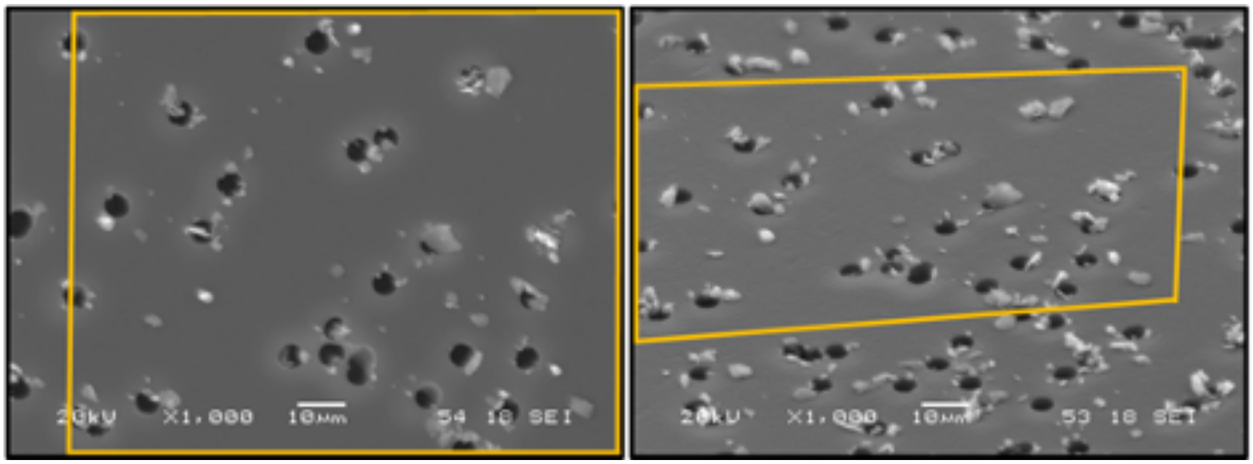

Figure 3. Scanning Electron Microscopy (SEM) images of typical Saharan dust collected at Bir Moghrein, Mauritania, using in situ filter collection at a height of 3-meters above soil during the Fennec campaign in 2011 (Rocha-Lima et al., 2018). Delimited area in both images shows the same particles seen at top view (on the left) and tilted at an angle of 45° (on the right). Image credit: Earth and Space Institute (ESI) – University of Maryland, Baltimore County (UMBC).

Huang et al. (2020) compiled and synthesized AR and HWR measurements from an extensive collection of studies. Distribution parameters (such as the median and standard deviation) of the AR are most prevalent. The HWR is provided by only four studies. The global median AR is 1.70 while the median HWR is 0.4. Thus, dust particles are flatter and longer than spheres. Regional variations of distribution parameters are statistically distinct but small (Huang et al., 2020), which offers hope for parsimonious representations of non-spherical particles in Earth system models and remote sensing retrieval algorithms. The median AR for North African dust is 1.6, while Asian particles are slightly more elongated with a median AR of 1.72. Asian dust has a typical HWR of 0.35 compared to rounder North African particles with an HWR of 0.6, although measurements of the latter region are available only for a single study (Jeong et al., 2016). Distributions of particle shape appear to be nearly independent of size for particle diameters up to 20 µm (Huang et al., 2020).

The irregular particle shapes result in greater aerodynamic resistance compared to spherical idealizations that are typically used to calculate model fall speeds. Huang et al. (2020) calculated that the mean fall speed of ellipsoidal particles with a globally averaged shape distribution of AR and HWR is reduced by 15% compared to spheres of equal volume, which increases particle lifetime by 20%. They invoke this reduction to interpret the increase of AR during transport downwind of Africa; nearly spherical particles (i.e., with AR near unity) fall out more rapidly and the remaining particles become more aspherical with increased AR. Huang et al. (2020) note that their calculation of aerodynamic drag assumes smooth ellipsoids and does not account for particle roughness and shape irregularities that would lead to further reductions in falling speed and increases in lifetime, especially for larger particles where gravitational settling is the most rapid removal process.

Ambient measurements suggest that the random orientation of dust particles assumed by most studies may not always be true. Ulanowski et al. (2007) inferred that freshly emitted dust particles are present in the atmosphere with their longest axis oriented along the vertical. The flat, elongated nature of dust particles thus has important implications for both modelling of radiative properties and remote sensing retrievals, as vertically aligned dust particles would have a reduced cross-sectional area, decreasing the optical thickness of the dust layer. The vertical orientation is hypothesized to result from electrical fields created during dust emission. The eventual dissipation of the field would eliminate the preferred vertical orientation, increasing the particle cross section and extinction, analogous to the closing of Venetian blinds.

### 2.3 Composition

Dust particles are typically mixtures of different minerals (Buseck et al., 2000; Scheuvens and Kandler, 2014) that depend upon the soil composition at the source. For example, particles traced to the northwestern Sahara show a greater illite fraction (a common phyllosilicate or clay mineral within dust) than particles from sources within the Sahel or eastern Sahara (Caquineau et al., 2002). Figure 4 shows soil samples from the Saharan and Israeli desert regions. The differences in color of the soil samples illustrates the high variability of mineral composition of dust sources. Dust composition is also modified during transport through coagulation with other aerosol species (Bauer et al., 2008) or heterogeneous reactions on the dust particle surface that add coatings of sulfate and nitrate (Dentener et al., 1996; Trochkine et al., 2003).

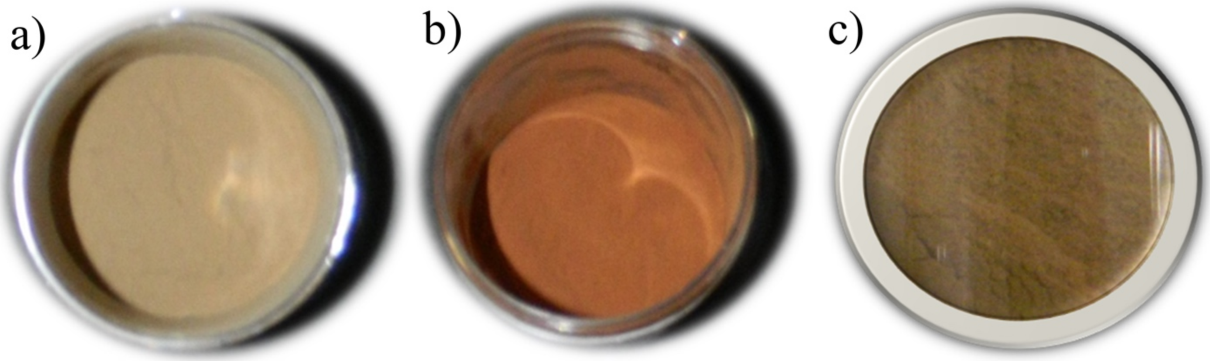

Figure 4. Soil samples from different desert regions, illustrating the high variability of mineral composition of dust sources. a) Saharan dust, Algeria, b) Saharan dust, Senegal, and c) Negev dust, Israel. Sample credit: : a) from the Fennec campaign, June 2011 (Washington et al., 2012), and (b-c) from the Statistical Evaluation of Aerosol Retrievals (STEAR) experiment (Schuster et al., 2019).

Claquin et al. (1999) give regionally varying soil fractions for eight common or climatically relevant minerals: quartz, feldspar, phyllosilicates (clay minerals like illite, kaolinite, and smectite), calcite, gypsum, and the trace mineral hematite that may dominate shortwave dust aerosol absorption (Moosmüller et al., 2012). Journet et al. (2014) added mica and the iron-bearing goethite along with two clays: chlorite and vermiculite. These minerals have distinct climate impacts. Calcite acts as a buffer to the acidic coatings of sulfates and nitrates on dust particle surfaces (Gassó et al., 2010), while (potassium) feldspar is possibly the most efficient ice nucleation site (Atkinson et al., 2013). Clays, along with hematite and goethite, provide iron that catalyzes ocean primary productivity (Jickells et al., 2005); atmospheric processing by photoreactions and processing within cloud and aerosol droplets during transport convert the iron into bioavailable forms (Hand et al., 2004; Moxim et al., 2011).

Mineral dust composition has been inferred by a variety of techniques mostly focused on bulk samples. In situ collection of dust particles on filters is the most widely used method to directly measure the sample mass, atmospheric mass concentration, microscopic shape, and chemical composition. Mass spectrometry is often used to characterize individual particles (Kandler et al., 2011, 2009, 2007) along with microscopy techniques (Kandler et al., 2007; E. A. Reid et al., 2003).

X-ray diffraction (XRD) is a method for determining mineralogical composition of low mass aerosol samples but is only semi-quantitative (Sadrian et al., 2022). Measurements by x-ray fluorescence (XRF) allow for quantitative determination of the total elemental composition of a sample (e.g., Watson et al., 1999). However, one limitation of this method is that while different iron oxides can produce chemical shifts in the elemental emission lines, current instrumentation lacks sufficient resolution to quantitatively differentiate them. Combinations of elements from mass spectrometer analysis are used to identify minerals, but it can be difficult to distinguish some minerals with similar elemental composition like clays and feldspars (Kandler et al., 2009).

This is a key uncertainty given the efficiency of potassium feldspar as a site for ice nucleation (Atkinson et al., 2013).

Measurements used to evaluate models with prognostic aerosol mineral composition or develop to climatology of regional dust composition are limited and probably insufficient at present (Perlwitz et al., 2015a). Measurements of elemental composition are comparatively abundant (e.g., Malm et al., 1994), but have only rarely been utilized in mineral identification and model evaluation (Pérez García-Pando et al., 2016; Y. Zhang et al., 2015).

### 2.4 Optical Properties

The ability of dust particles to scatter or absorb radiation depends upon their composition, size, and shape. The optical effect of composition is characterized by the index of refraction, which is generally a complex number. Total light extinction is a complicated function of the complex refractive index with light absorption dominated by the imaginary part of the refractive index (Moosmüller and Sorensen, 2018a, 2018b; Sorensen et al., 2019).

Figure 5a-b shows several estimates of the complex refractive index derived from analysis of bulk dust samples, either from soil or ambient aerosol samples. The range of visible wavelengths corresponding to half of the total solar irradiance are marked with green shading, with lighter shading indicating the near infrared that corresponds to one-quarter of total solar irradiance. Refractive index measurements in the shortwave made by Patterson et al. (1977) for ambient samples collected along the trajectory of a plume traversing the Atlantic from Africa, ranging from the Canary and Cape Verde Islands downwind to Barbados, are shown in blue triangles.

Recent optical analyses of bulk soil samples first suspend the samples in the laboratory then sort by size to create a dust sample that is representative of long-range transport (e.g. Di Biagio et al., 2014; Engelbrecht et al., 2016). The method assumes that the sizes and mineral fractions of the suspended aerosols created by mechanical vibration and fragmentation of soil aggregates within the suspension chamber resemble the natural aerosol fragments created by bombardment and sandblasting from windblown saltators. The gray shading in Figure 5a-b shows the range of indices of refraction from nineteen soil samples from source regions across five continents analyzed by Di Biagio et al. (2019, 2017). At solar wavelengths, the most absorbing sample corresponds to soil from Niger, while the least absorbing sample was collected from the Bodélé Depression, the dried-out bed of a former extensive lake containing calcium-rich lakebed sediments and silica-rich mixed diatom skeletons that disintegrate easily into erodible sizes (Abouchami et al., 2013; Engelbrecht et al., 2016).

Alternatively, some aerosol retrieval and modeling applications utilize a retrieved dust refractive index from AERONET and TOMS shortwave radiances at locations of high dust concentration (e.g., Colarco et al., 2014; Dubovik et al., 2002; Lee et al., 2017). The Todd et al. (2007) and Sinyuk et al. (2003) datasets shown in Figure 5a-b are two dust refractive index estimates informed by AERONET observations located in the Bodélé Depression during the BoDEx campaign and Cape Verde, respectively. At solar wavelengths, measurements of the real refractive index at solar wavelengths are in good agreement (Figure 5a), while the imaginary index, plotted on a logarithmic scale, shows greater variation among samples that reflects regional differences in composition (Figure 5b).

At thermal wavelengths, several modeling studies (e.g., Tegen and Lacis, 1996; Yoshioka et al., 2007) use the refractive index measured by Volz (1973). In contrast to measurements of aerosolized soil samples, Volz (1973) measured the reflectance and extinction by pellets formed from aerosols collected under ambient conditions in Barbados. The Optical Properties of

Aerosols and Clouds database (OPAC; Hess et al., 1998) is another index that is widely used by dust models (see Section 5 and Table 21) and that resembles measurements by Patterson et al. (1977) in the shortwave and Volz (1973) at thermal wavelengths. Within the 8-12 um atmospheric infrared window (Figure 5a-b, pink shading), where the dust longwave effect is largest, the real and imaginary parts of the index calculated by Volz (1973) and OPAC exceed or are at the upper end of the range of indices corresponding to the worldwide collection of soil samples by Di Biagio et al. (2019, 2017; gray shading). The difference is especially large for the real part. However, Di Biagio et al. (2014) note that neither the Volz (1973) or OPAC indices satisfy the Kramers-Kronig relationship, a physics-based constraint linking the real and imaginary indices. One implication is that the longwave radiative effect is overestimated in the widespread applications using the indices from Volz (1973) or OPAC, compared to applications using the chamber measurements that explicitly satisfy this constraint (gray shading). (1987)(e.g., Tegen and Lacis, 1996)(2017)Sections 4 and 5 show more comparisons of assumed dust refractive indices in specific global models and retrieval algorithms. The reader is referred to Di Biagio et al. (2019, 2017, 2014) for a more complete compilation of dust refractive index measurements.

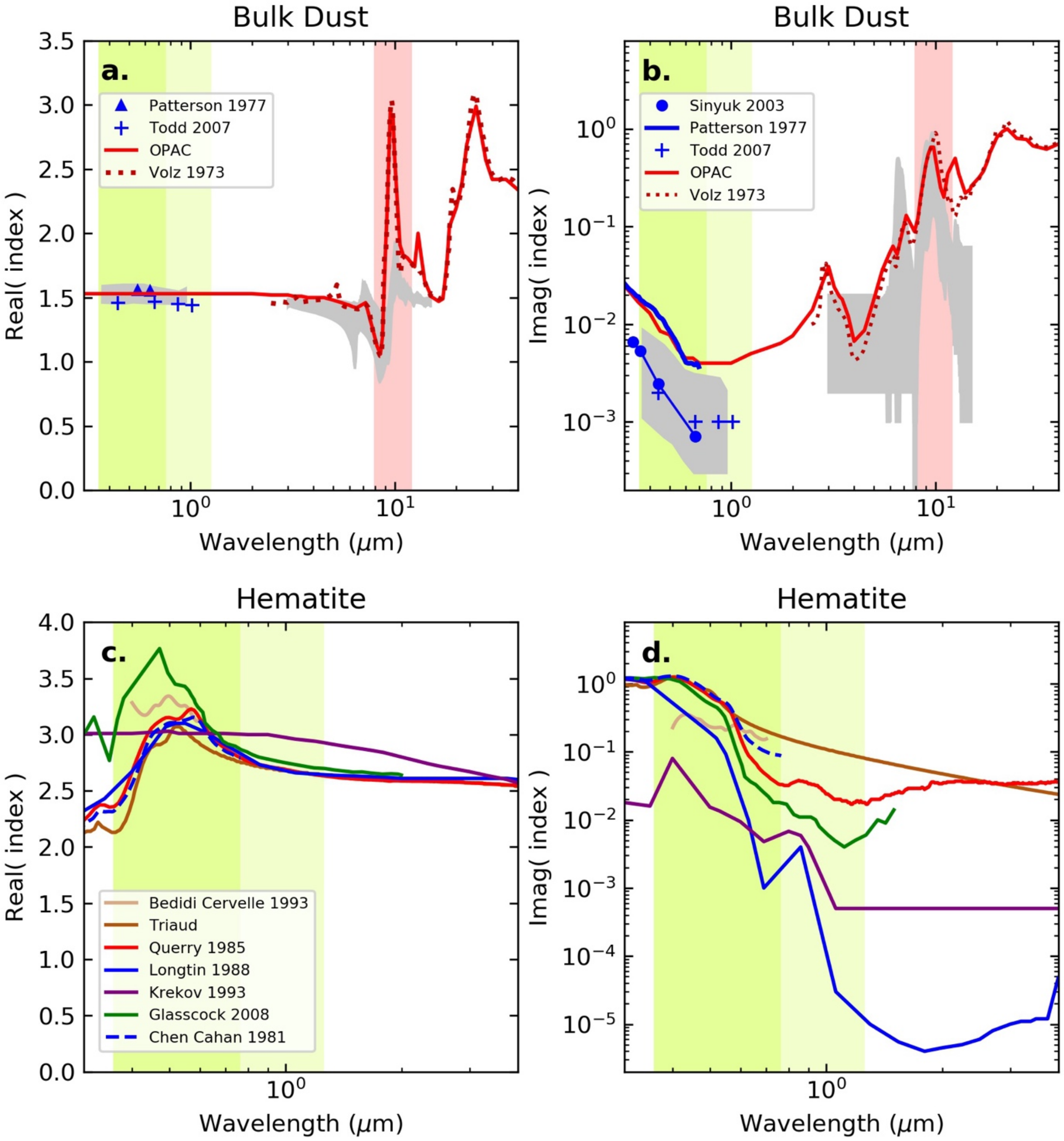

Figure 5. Real (a, c) and imaginary (b, d) parts of the index of refraction for bulk dust (a, b) and hematite (c, d). Gray shading shows the range of values from the nineteen soil samples analyzed by Di Biagio et al. (2019, 2017). The atmospheric 'window' where extinction of thermal radiation by dust is especially large is indicated by pink shading. Green shading shows visible wavelengths containing roughly half of total solar irradiance (TSI), while lighter green shading at

near-infrared wavelengths corresponds to one-quarter of TSI. The OPAC values correspond to the transported mineral dust category of that database. The indices in this figure are chosen to indicate the diversity within the literature or else widely used values like Patterson et al. (1977) or Volz (1973) and OPAC. The OPAC values correspond to the transported mineral dust category of that database. The indices in this figure are chosen to indicate the diversity within the literature or else widely used values like Patterson et al. (1977) or Volz (1973) and OPAC. More complete literature compilations are given by Di Biagio et al. (2014, 2017, 2019).

The bulk soil refractive index measurements in Figure 5a-b are often assumed by models and remote sensing retrieval algorithms to represent dust aerosols globally, and thus characterize dust radiative effects with a single wavelength-dependent but spatially invariant refractive index. Some versions of modern global models explicitly predict mineral composition to represent spatial and temporal variations in dust radiative effects (Li et al., 2021; Pérez García-Pando et al., 2016; Perlwitz et al., 2015a, 2015b; Scanza et al., 2015). This approach allows for representation of regional variations in the mineral composition of dust source regions. For example, soil mineral composition estimated by Claquin et al. (1999) identifies the Thar Desert and Sahel as dust sources that are enriched in the iron-oxide hematite.

Mixing rules are needed to relate the index of refraction of an aggregate particle to the indices of the individual minerals comprising the aggregate (Sokolik and Toon, 1999). However, these rules are often heuristic, or require assumptions about the spatial structure of minerals comprising the particle (Balkanski et al., 2007). Alternative to mixing rules are empirical relations that relate the fractional presence of a particular mineral like hematite or quartz to the index of refraction at specific wavelengths or absorption bands (Di Biagio et al., 2019; Moosmüller et al., 2012). For example, absorption in the visible is dominated by hematite and goethite (Di Biagio et al., 2019; Moosmüller et al., 2012), while long-wave absorption is mainly due to quartz, clays, and calcite (Di Biagio et al., 2017; Sadrian et al., 2023). These empirical relations are derived assuming an internal mixture of all minerals in the soil sample, as knowledge of the mixing state of individual particles is lacking. An additional difficulty of relating optical properties to composition is that the refractive index of strongly absorbing minerals like hematite shows wide variations within the literature (Zhang et al., 2015), making estimates of dust optical properties for particles containing this mineral uncertain.(2015) Several estimates for hematite are depicted in Figure 5c-d and show an order of magnitude difference. Moreover, we know of only one such spectrum for goethite (Bedidi and Cervelle, 1993), but it has been argued that this spectrum should be rejected (Warren et al., 2019). Therefore, more investigations into fundamental dust mineral optical properties are needed, in particular, to reconcile the conflicting measurements for individual minerals that are radiatively important.

Another important optical property is the single-scattering phase function, which describes the angular distribution of light intensity scattered by a particle or distribution of particles (Stamnes et al., 2017). However, there are few direct measurements of the dust phase function. One such set of measurements is the Amsterdam-Grenada light scattering database (Muñoz et al., 2012), which provides direct laboratory measurements of particle scattering phase functions for several dust samples collected from around the world (Martín et al., 2021; Muñoz et al., 2010, 2007). A drawback of the approach is that it requires suspension of high mass samples, which may not be representative of ambient dust. Recent progress has been made in directly measuring dust scattering phase functions of ambient aerosol samples with field-deployable, polar nephelometers (Barkey and Liou, 2001; Bian et al., 2020, 2017; Castagner and Bigio, 2006; Curtis et al., 2007; Dolgos and Martins, 2014; Espinosa et al., 2018; Muñoz et al., 2011, 2001).

Open-path imaging nephelometers that can be mounted on the outside of aircraft are promising for overcoming size sampling challenges characteristic of closed systems with inlets and tubing (Martins, 2016). However, only one study has characterized ambient dust phase functions. Horvath et al. (2018) measured 532-nm phase functions of transported Saharan dust plumes in the Sierra Nevada mountains of Spain, and found lower backscattering compared to non-dust plumes, as is characteristic of non-spherical particles like dust. Because of the absence of a comprehensive set of dust single scattering phase function measurements that can be shown to be globally representative, most remote sensing algorithms and global models rely on theoretical calculations of single scattering properties based on dust fundamental characteristics - complex refractive index, shape, and size - as the basis of dust optical models.

# 3 Theoretical Efforts Toward Modeling Dust Optical Properties

We use the term optical modeling to describe the process of calculating aerosol's single-scattering properties from fundamental microphysical characteristics, specifically particle size distribution, morphology, and complex refractive index (determined by chemical and mineralogical composition). In this section we will provide a brief overview of the common heritage that remote sensing algorithms and global models have with respect to optical modeling, and refer the reader to Nousiainen (2009) and Nousiainen and Kandler (2014) for a more complete review.

## 3.1 Definitions of Modeled Optical Properties

To begin, we define some common terms used to describe aerosol optical properties. The scattering matrix ***P*** is a 4 by 4 Mueller matrix that relates incident and scattered light represented by Stokes vectors, which encode the polarization state of the light. The single scattering phase function, $P_{11}$, is the first element of ***P***.

The Stokes vectors are usually represented as having four elements, *I*, *Q*, *U*, and *V*, where *I* is the light intensity, *Q* and *U* specify the plane of linear polarization, and *V* defines the sense of circular polarization. ***P*** can be reduced to just 6 independent non-zero elements if its constituent particles are (1) randomly distributed in space and orientation, and (2) present in equal numbers with their mirror symmetric counterparts or have at least one plane of symmetry (Mishchenko et al., 2006). Under these conditions the aerosol is said to be macroscopically isotropic and mirror-symmetric, and the scattering phase matrix simplifies to block-diagonal form:

$$\boldsymbol{P} = \begin{bmatrix} P_{11} & P_{12} & 0 & 0 \\ P_{12} & P_{22} & 0 & 0 \\ 0 & 0 & P_{33} & P_{34} \\ 0 & 0 & -P_{34} & P_{44} \end{bmatrix} \qquad \text{Eq 1.}$$

where each element is azimuthally independent, and therefore only a function of the scattering angle $\theta$. Here we adopt a common normalization scheme for $P_{11}$ based on the integral of $P_{11}$ over all angles, specifically:

$$\int_0^{\pi} P_{11}(\theta)\sin(\theta)d\theta = 2 \qquad \text{Eq 2.}$$

The block-diagonal form of ***P*** is generally thought to be valid for most naturally occurring aerosols, and almost all dust radiative calculations to date have assumed this reduced form. However, it should be noted that natural counterexamples are occasionally observed, such as the vertically aligned dust particles reported by Ulanowski et al. (2007). Cirrus particles can also have preferred orientations that are responsible for producing atmospheric optical phenomena such as sun dogs (parhelia), arcs, and pillars (Lynch and Livingston, 2001). However, there is considerable turbulent mixing in the atmosphere under most circumstance, and most aerosol particles are too small and symmetric to become aligned under typical atmospheric conditions.

The Degree of Linear Polarization (DoLP) represents the relative proportion of light that is linearly polarized. In terms of the first three elements of the Stokes vector, *I*, *Q*, and *U,* this quantity is defined as

$$DoLP = \sqrt{Q^2 + U^2}/I \qquad \text{Eq 3.}$$

Scattering matrix elements are frequently expressed in terms of the ratios $P_{ij}/P_{11}$ and the use of the ratio $-P_{12}/P_{11}$ is particularly common. In the case of unpolarized incident light, like that produced by the sun, the DoLP of light single-scattered by an aerosol is equal to $-P_{12}/P_{11}$.

Additionally, an important polarimetric quantity measured by many lidar systems is the linear depolarization ratio, which is defined as the ratio of intensities measured in the backscattering direction (π) perpendicular ($I_{\perp}$) and parallel ($I_{\parallel}$) to the transmitting laser's polarization axis:

$$\delta_L = \frac{I_{\perp}}{I_{\parallel}} = \frac{P_{11}(\pi) - P_{22}(\pi)}{P_{11}(\pi) + P_{22}(\pi)} \qquad \text{Eq 4.}$$

The single-scattering backscatter signal of a linearly polarized laser pulse from spherical particles is totally copolarized ($\delta_L = 0$). In the case of non-spherical particles, the backscatter signal contains a cross-polarized component and $0 < \delta_L < 1$. Typical values for mineral dust particles can range from 0.1 – 0.5 (Burton et al., 2012; Järvinen et al., 2016). Another variable that is fundamental to active measurements is the lidar ratio, which is defined as:

$$S = \frac{4\,\pi\beta_{ext}}{\beta_{sca}\,P_{11}(\pi)} = \frac{4\,\pi}{\omega\,P_{11}(\pi)} \qquad \text{Eq 5.}$$

Where $P_{11}(\pi)$ is the value of the phase function in the exact backscattering direction and $\beta_{ext}$ and $\beta_{sca}$ are the particle total extinction and scattering coefficients, respectively. The extinction and scattering coefficients are defined Eqs. 3 and 4 in the Supplementary Documentation. We note that Eq 5 gives lidar ratio in units of steradian when $P_{11}$ is normalized according to Eq 2. The aerosol single scattering albedo $\omega$ is defined by the ratio $\beta_{sca}/\beta_{ext}$.

## 3.2 Representation of Dust Particles

### 3.2.1 Size Parameter

The Scale Invariance Rule (SIR) states that, for a given particle shape and structure, the electromagnetic scattering properties at wavelength $\lambda$ for a scatterer with a characteristic length $r$ (e.g., the smallest or largest particle dimension) are constant for any fixed value of the ratio $r/\lambda$, provided the complex refractive index is constant with wavelength (Mishchenko, 2006). This feature conveniently permits single scattering properties to be specified in terms of the dimensionless quantity $x = 2\pi\, r/\lambda$, which is traditionally referred to as the size parameter. Furthermore, SIR permits measurements and theoretical calculations of optical properties performed at one wavelength to be applied in other spectral regions. For example, the so-called microwave analog technique utilizes measurements of complex but easily manufactured, centimeter-sized objects observed in the microwave to estimate scattering properties of much smaller particles observed at visible wavelengths with equivalent size parameters (Gustafson, 1996). Size parameters relevant to dust optics within the shortwave solar spectrum range from less than unity for SWIR applications to as high as several hundred for calculations pertaining to UV wavelengths.

### 3.2.2 Particle Shape

Despite the wide variety and complexity of dust particle shapes observed in nature, modeling of the corresponding optics has often been limited to Lorenz-Mie theory for homogeneous spheres

(Lorenz, 1890; Mie, 1908). Spherical particles generally produce very different scattering patterns than their non-spherical counterparts, especially at the side- and back-scattering angles viewed by many space-based remote-sensing instruments. However, a variety of other shapes have been used to improve fidelity of the modeled optical properties. In most cases, they have been rotationally symmetric solids with smooth surfaces. Spheroids, which correspond to the half rotation of an ellipse about one of its principal axes, are by far the most common non-spherical shapes used in dust optical modeling (Dubovik et al., 2006; Mishchenko et al., 1995; Nousiainen et al., 2006; Nousiainen and Vermeulen, 2003). Spheroids are completely described by two parameters (bi-axial), frequently a metric of their total size and the ratio of their major and minor axes. A related but slightly more complex shape that requires an additional axis ratio to fully define it is an ellipsoid (tri-axial). Several authors have made use of the extra degree of freedom afforded by this second axis ratio to better mimic dust scattering properties (Bi et al., 2009; Meng et al., 2010). It should be noted that spheroids and spheres are actually special cases of ellipsoids having a value of unity for one or both axis ratios, respectively. In addition to the aforementioned shapes defined by smooth quadratic surfaces, numerous dust modeling efforts have used more complex particle shapes, including super-spheroids that have an additional degree of freedom and can model particle sharp edges and concavities (Bi et al., 2018; Kong et al., 2022; Lin et al., 2021, 2018), gaussian random spheres (Muinonen et al., 1996; Liu et al., 2015; Nousiainen et al., 2011; Veihelmann et al., 2006), various polyhedra (Bi et al., 2010; Liu et al., 2013; Nousiainen et al., 2006; Saito and Yang, 2021), Chebyshev particles (Mishra and Tripathi, 2008; Mugnai and Wiscombe, 1986) and different aggregates thereof (Gasteiger et al., 2011), as well as aggregates of multiple cubes or spheres in different configurations (Kalashnikova et al., 2005). Models of highly irregular shapes also exist, such as agglomerated debris particles (Zubko et al., 2018). Some work has been done with shapes explicitly inverted from real dust particles (Lindqvist et al., 2014), as well as shapes that aim to emulate inhomogeneous grain-like structures of real dust (Kemppinen et al., 2015a).

The choice of particle shape can strongly impact the resulting single scattering properties; accounting for particles with non-spherical shapes is therefore critical to accurate inversions of multi-angle and polarimetric observations. In dust size regimes, polydisperse collections of non-spherical particles generally have flatter phase functions and larger values of $-P_{12}/P_{11}$ at side scattering angles than their spherical counterparts (Dubovik et al., 2006; Kalashnikova et al., 2005; Zhou et al., 2020). In addition to the variations in scattering properties that result from the transition from spherical to non-spherical classes of particles, deviations between different non-spherical particle shapes can also be significant. Kemppinen et al. (2015b) found that a scattering matrix measurement inversion that assumed ellipsoids in the presence of more complex irregular dust-like particles can produce large errors in the retrieved refractive index. They showed that the use of this erroneous refractive index in flux calculations may lead to TOA flux errors of over 100%.

At exact backscattering angles ($\theta = \pi$), scattering matrix elements tend to exhibit particularly strong sensitivity to particle shape (Wiegner et al., 2009), which makes accurate shape modeling especially important when interpreting lidar observations. Spherical shapes are ill-suited for simulations of dust lidar returns, particularly in studies involving measurements of $\delta_L$, which is always zero in the case of spherical particles. Traditionally, it has been thought that the impact of dust particle shape on quantities integrated over all scattering angles, such as $\beta_{ext}$ and $\beta_{sca}$, is much more limited (Mishchenko et al., 1997, 1995; Räisänen et al., 2013), implying that ignoring non-sphericity would have a negligible impact on radiative flux calculations. However, several studies have suggested that particle shape can meaningfully impact aerosol radiative forcing estimates (Kahnert et al., 2007, 2005; Kalashnikova and Sokolik, 2004; Nousiainen and Vermeulen, 2003; Yi et al., 2011). A few authors have concluded that, although particle shape can impact top-of-atmosphere (TOA) flux by 10% or more, the flux is considerably more sensitive to the choice of complex refractive index (Colarco et al., 2014; Mishra et al., 2008; Mishra and Tripathi, 2008).

### 3.2.3 Mixing State and Internal Structure

In addition to particle size and shape, the complex refractive index is also required to fully determine the single scattering properties of a particle. The majority of naturally occurring particles are chemically and mineralogically heterogeneous and cannot be modeled exactly using just one refractive index. A heterogeneous aerosol is said to be fully externally mixed when individual constituent particles are composed of just one species. By contrast, in an internally mixed aerosol, individual particles contain more than one species. The optical properties of aerosols are often highly dependent on the mixing state.

It is typically easier to calculate bulk optical properties for an external mixture than an internal mixture. This is because in external mixtures the single scattering properties of individual, homogenous particles can be calculated independently using their individual refractive index values; then combination rules are used to obtain the optical properties of the bulk, chemically heterogeneous aerosol. Internal mixtures require methods that can account for multiple refractive indices simultaneously. A hybrid approach is often taken using so-called Effective Medium Theories (EMTs), which derive a single “effective” refractive index that best reproduces the scattering properties of a multi-species, internally mixed particle. Two of the most commonly used EMTs are Maxwell-Garnett theory (Garnett, 1904) and Bruggeman theory (Bruggeman, 1935), with one study finding the latter better suited for dust (Xie et al., 2014).

Individual dust particles are rarely chemically homogenous. In addition to having heterogenous mineralogy, they are also frequently found coated with nitrate, sulfate, and black carbon (Kandler et al., 2011; Petzold et al., 2011; Sobanska et al., 2012). Unfortunately, the performance of EMTs tends to degrade with increasing size parameter, making their application to dust at solar wavelengths particularly tenuous (Nousiainen, 2009). Techniques for computing the single scattering properties of particles with internally heterogeneous refractive indices without employing EMT-based approximations are generally very computationally intensive, but some authors have attempted to model dust using these methods. Morphologies used in these studies include collections of porous cubes (Vilaplana et al., 2006) as well as various fluffy agglomerates (Zubko et al., 2013, 2008). Good agreement with measurements has also been achieved using an approximate, ad hoc scheme with randomly oriented Lambertian screens embedded in large host particles that are otherwise homogeneous (Muñoz et al., 2007; Nousiainen and Vermeulen, 2003).

#### 3.2.4 Surface Roughness

Electron microscope images of dust particles frequently reveal roughened surfaces (Figure 3) (Rocha-Lima et al., 2018). Roughness is observed both on the surface of single, large dust particles as well as through the agglomeration of small particles ($D < 1$ μm) onto a larger host particle. Empirical data regarding the impact of surface roughness on optical properties are limited. However, several numerical studies suggest that increased surface roughness produces smoother phase functions, especially in aerosols with narrow or monodisperse size distributions where high frequency oscillations in scattering properties are otherwise pervasive (Yang et al., 2007). Another feature generally associated with roughened particles is a decrease in the high phase function values that occur at backscattering angles (Zubko et al., 2007). However, the maxima of $|P_{12}|$ and $|P_{22}|$ tend to increase with surface roughness in the range of size parameters smaller than x ≤ 50 (Kemppinen et al., 2015a; Yang et al., 2007; Zubko et al., 2007); yet, this trend reverses as the particle size transitions into the geometric optics regime (Muñoz et al., 2007; Nousiainen et al., 2003).

## 3.3 Calculation of Single Scattering and Absorption Characteristics

### 3.3.1 Methods for Spherical Particles

The choice of algorithm for calculating aerosol single scattering properties is generally guided by a tradeoff among particle complexity, computational expense, and accuracy. The simplest and most computationally inexpensive approach is to assume homogeneous spherical particles for which publicly available Mie codes provide fast, accurate solutions within the particle size and refractive index ranges generally relevant to dust (Bohren and Huffman, 1998; Mishchenko et al., 2006; Sumlin et al., 2018; Wiscombe, 1980). Additional complexity can be added, without excessive loss of computational efficiency, with methods for internally mixed core-shell particles, which are spherical in shape but have a radial dependence in their refractive indices (Mishchenko et al., 2006; Toon and Ackerman, 1981). This approach has been used, for example, to simulate a spherical dust core with a uniform outer coating of sulfate (Bohren and Huffman, 1998; Pilinis and Li, 1998).

### 3.3.2 T-matrix Methods

The T-matrix is a quantity that conveys information about the scattering characteristics of a given particle, independent of the scattering geometry, particle orientation and polarization state of the incident light (Mishchenko, 2000). Waterman (1965) first proposed the use of the T-matrix for calculating optical properties through what is now commonly known as the T-matrix method, but also sometimes referred to as the extended boundary condition method (EBCM) or the null-field method. Other techniques utilizing the T-matrix have since been developed, including the Superposition (Mackowski and Mishchenko, 1996) and Invariant Imbedding methods (Bi et al., 2013; Johnson, 1988). Bi and Yang (2014) were the first to show that T-matrix methods can be applied to larger size parameter ranges (up to the geometric optics domain), inhomogenous particles, and arbitrary shapes that were not practical with the traditional EBCM. The T-matrix's lack of dependence on external geometry makes the corresponding approaches particularly efficient when calculating optical properties for randomly oriented ensembles of particles. In general, modern T-matrix approaches make it feasible to calculate single scattering properties of randomly oriented collections of particles with size parameters ranging from 0 to ~100 (Hu et al., 2020), although the exact computationally feasible upper bound on $x$ strongly depends on shape (Bi et al., 2013). T-matrix approaches lend themselves particularly well to smooth, spheroidal shapes, and the prevalence of these shape assumptions in dust optical modeling is largely due to the fast and reliable T-matrix code of Mishchenko and Travis (1998). Recent advances in dust optical models that represent dust as inhomogenous and/or irregular particles (Bi et al., 2022; Saito et al., 2021; Zong et al., 2021) rely on the Invariant Imbedding Method (IIM) T-matrix code of Bi et al. (2013) .

### 3.3.3 Methods for Particles with Arbitrary Morphologies

Although the above techniques are generally only accurate for limited subsets of particle shapes, others are much more broadly applicable. The Discrete Dipole Approximation (DDA) mimics arbitrary particle morphologies by representing them as a 3-D lattice of coupled dipole moments that respond to the surrounding electromagnetic field (Draine and Flatau, 1994; Purcell and Pennypacker, 1973). Because the number of dipole moments required to achieve a given accuracy typically scales with the volume of the scatterer, the computational cost of DDA grows rapidly for larger particles. When applied to randomly oriented and realistically polydisperse particle populations, DDA often becomes computationally infeasible for distributions with size parameters exceeding around 50 (Kalashnikova et al., 2005; Yang et al., 2019). The finite-Difference Time-Domain (FDTD) is another common approach for simulating arbitrary particle shapes and can be more computationally efficient than DDA in some cases (Taflove and Hagness, 2005; Yang et al., 2000; Yee, 1966). The related PseudoSpectral Time-Domain (PSTD; Liu, 1997) approach has also been applied to dust in at least one instance (Hu et al., 2018) and the method is often feasible for size parameters as large as 80 (Chen et al., 2008). Generally, the time-domain techniques outperform DDA for larger real refractive indices, with the breakeven point frequently occurring around 1.4 (Liu et al., 2013; Yurkin et al., 2007).

Unlike all the aforementioned techniques, the accuracy of geometric optics (raytracing) methods generally increases with increasing particle size. In its simplest form, the geometric optics approach approximates the incoming light as a collection of rays that obey the laws of reflection and refraction within and at the boundaries of the particle. Because conventional geometric optics does not account for effects like diffraction and interference, it only produces acceptable results in cases where the wavelength of the light is much smaller than the particle, generally size parameters greater than 200 (Yang et al., 2019). The Improved Geometric-Optics Method (IGOM; Yang and Liou, 1996) uses the electromagnetic equivalence theorem to partially overcome these limitations and has permitted modeling of dust particles with size parameters as small as 20 (Muinonen et al., 2009). More recently, Bi et al. (2011) have developed the Physical

Geometric-Optics Hybrid method (PGOH) that can occasionally permit accurate light scattering calculations at even smaller size parameters, especially for relatively simple particle morphologies. Note that both conventional and improved geometric optics methods do not account for the coherent backscattering mechanism in their calculations, resulting in systematic biases in the simulations of backscattering properties. However, the coherent backscattering effect is incorporated into physical geometric optics methods, which can accurately compute the backscattering properties of non-spherical particles. These methods are particularly useful for lidar-based remote sensing applications (Yang et al., 2019).

#### 3.3.4 Precomputed Databases of Dust Optical Properties

Owing to the difficulty and large computational costs associated with running most light-scattering codes, a few researchers have released precomputed databases of dust single scattering properties for use by the broader community by employing both exact and approximate light scattering computational methods across the size parameter range relevant for dust (Yang et al., 2019). Meng et al. (2010) produced a set of precomputed optics corresponding to tri-axial ellipsoids with semi-minor and semi-major aspect ratios extending down to 0.3. A similar database for a set of spheroids with a fixed axis ratio distribution has been packaged with the Generalized Retrieval of Aerosol and Surface Properties (GRASP) code (Dubovik et al., 2011, 2006) and is freely available for download (https://www.grasp-open.com). Most recently, Saito et al. (2021) released a database for an ensemble of irregular hexahedral geometries designed to mimic dust and volcanic ash particles. The authors found that the shapes used were particularly well suited for reproducing the backscattering signals of lidar returns that have traditionally been difficult for simpler ellipsoid-based models to reproduce. This database is also now freely available for download (https://github.com/masasaito/TAMUdust2020).

Given their ease of use, these precomputed databases of dust single scattering properties are the basis by which nearly all remote sensing retrieval algorithms and global models represent non-spherical dust light scattering in the atmosphere. In the following sections, we describe the microphysical assumptions and corresponding scattering properties for dust used in various remote sensing, Earth system modeling, and Mars modeling applications.

# 4 Remote Sensing Dust Models

*Remote sensing* is the process of inferring the physical characteristics of a scene by measuring its reflected and emitted radiation from a distance. The sensor (which may be an imager, polarimeter, spectrometer, lidar, or other device) observes the electromagnetic signature of the scene, and then an inversion technique is applied to determine what has contributed to that signature. However, the capabilities of the sensor, convolved with the scene it is observing and the property one wishes to derive, drive the retrieval technique and assumptions made during that retrieval.

*Passive* remote sensing uses measurements of the ambient radiation field, differentiated from *active* remote sensing that introduces radiation to the field. Passive space-based sensors measure the reflectance or radiance from the total system, from a vantage point at the top-of-atmosphere (TOA). Shortwave (SW; $\lambda < 4$ $\mu$m) techniques rely on observing scattered solar radiation, whereas longwave (LW; $\lambda > 4$ $\mu$m) techniques rely on observing the transmission of terrestrial thermal radiation. In this review we will focus on shortwave remote sensing techniques, which are so far the most widely available and utilized observations for validating and constraining global aerosol models, as thermal infrared retrievals face several difficulties that result in significant retrieval uncertainties. The dust infrared scattering signal is relatively weak requiring high measurement sensitivity and accurate correction for trace gas aborption. Furthermore, the thermal infrared retrieval requires knowledge of the dust vertical profile and temperature profile. For these reasons, most thermal infrared dust retrievals are based on hyperspectral sounder observations such as Infrared Atmospheric Sounding Interferometer (IASI) and the Atmospheric Infra-Red Sounder (AIRS) (Klüser et al., 2011; Peyridieu et al., 2009). However, these instruments are limited by their coarse spatial resolution. Recent progress has been made at retrieving dust optical depth with high spatial resolution imager observations in the thermal infrared by combining them with vertical profile information from other sensors (Zheng et al., 2023, 2022), and should be further explored in comparisons with models.

For aerosol applications, active remote sensing takes on the form of lidars that generate pulses of radiation to detect objects in the path of the pulse. The amount of time from pulse generation to backscattered signal detection is related to the distance traveled and the object detected. In general, as dust particle size is largely on the order of 0.1 – 10 $\mu$m diameter, much of its radiative interactions are with wavelengths of similar order, and many passive and active remote sensing techniques aim to characterize dust by using measurements in some part of the tropospheric SW ($0.3 < \lambda < 4$ $\mu$m) spectral range.

Although there is information content in both passive and active SW observations that can be exploited to retrieve aerosol properties, in general, and dust properties, specifically, the difficulty is that light interactions with the surface, gases, clouds, and non-dust aerosols can also contribute to the observed radiation signal, creating an indeterminate problem. Therefore, the strategy that aerosol retrieval algorithms adopt is to constrain both aerosol and non-aerosol contributions to the observed signal, making assumptions where necessary.

To account for the impact of trace gases, nearly all passive aerosol remote sensing retrievals work at “window” wavelengths. These are wavelengths where trace gas absorption is minimal or can be estimated accurately. In terms of clouds, most aerosol retrieval algorithms screen them out and only consider cloud-free conditions, which hinders the study of aerosol – cloud interactions in the interface region between clouds and cloud-free sky (Koren et al., 2007; Marshak et al., 2021). To isolate the aerosol signal from the surface, algorithms use different strategies that are tailored to the capabilities of the sensor. For example, some algorithms attempt to observe the contrast between light scattering (bright) aerosols over dark surfaces, such as vegetated surfaces and the deep ocean that have low reflectance in selected VIS, NIR, and SWIR bands (e.g., the Moderate Resolution Imaging Spectrometer (MODIS) “Dark-Target” algorithm; e.g., Remer et al., 2020). Other algorithms utilize the relative contrast of light-absorbing (dark) aerosol above a reflective surface, such as the OMI UV aerosol algorithm (OMAERUS; e.g., Torres et al., 2007) that uses strong Rayleigh scattering or underlying cloud as the contrasting “surface.” Still others attempt to characterize both scattering and absorption, either by using observations acquired at multiple angles (e.g., the Multi-angle Imaging Spectroradiometer (MISR) algorithms; e.g., Kahn et al., 2009) and/or invariance of surface features over timescales (e.g., the Multi-angle Imaging Spectroradiometer (MISR) algorithms; e.g., Lyapustin et al., 2018).

Despite these various strategies, passive sensors obtain information about the radiation field insufficient to uniquely determine the aerosol microphysical properties. Thus, all these strategies require some assumptions about the size, shape, and refractive indices of the aerosol particles, which is generally called an *aerosol optical model*. Moreover, given the diversity of aerosol types that can be present in the atmosphere, for each observation, the algorithm must devise a strategy to select an appropriate aerosol model for that scene. Thus, in the case of dust, first dust must be detected, then a *dust model* assumed.

In the case of active remote sensing, there are different types of lidars, including backscatter lidar and high spectral resolution lidar (HSRL) (Sugimoto and Huang, 2014). Differences between them primarily have to do with how the pulses are being generated, and whether the pulses are emitted as a single discrete wavelength or modulated to be emitted across a narrow range of wavelengths, as well as how the backscattered signal is detected. Backscatter lidars require an assumed aerosol model, specifically the aerosol lidar ratio, to retrieve aerosol properties. HSRL requires fewer assumptions, as the high spectral resolution of the signal allows for a better separation of the narrowband aerosol backscatter and the more broadband molecular backscatter. However, currently no HSRL is flying in space.

Because different algorithms have been created based on the chosen sensor's information content, there is diversity in how these aerosol models were developed and applied. Likewise, there is diversity in how a particular algorithm first detects that dust is present and assigns a model that represents dust. For example, the MODIS "Dark Target" (DT) algorithm was designed to be applied to the solar wavelength range (e.g., 0.47 – 2.1 $\mu$m) and viewing geometry of MODIS (Levy et al., 2013). Because the most significant dust sources are in the subtropics, the dust models have been designed to ensure that MODIS validation metrics are unbiased on average in this region. However, there is limited variability in the MODIS observing geometry for those observations of dust. For a similar VIS/NIR/SWIR imager in Geostationary orbit (e.g., Advanced Baseline Imager on the Geostationary Operational Environmental Satellites (GOES)) or an imager with more observing angles (e.g., MISR), the statistics of observing geometry can be very different. The optimized MODIS-DT dust model differs from a multi-angle optimized dust model. Likewise, as MODIS almost never observes direct backscatter (180° scattering angle), it was never necessary for a MODIS dust model to represent a nadir-viewing backscattering lidar observation or the near-backscatter observations of the Deep Space Climate Observatory (DSCOVR; Marshak et al., 2022) positioned at the L1 Lagrange point. Similarly, dust models optimized for VIS/NIR/SWIR observations may not adequately represent dust properties in the UV spectral region observed by the Ozone Monitoring Instrument (OMI), the thermal infrared, or the spectral polarization signal observed by polarimeters.

When the Plankton, Aerosol, Cloud, ocean Ecosystem (PACE; Chowdhary et al., 2019) satellite launches in the mid-early 2020s, and the Atmosphere Observing System (AOS; Braun et al., 2022) in the late 2020s, there will be a constellation of passive and active sensors in low-Earth orbit that will simultaneously observe dust. These sensors will comprise a unified Earth observation system for UV through IR radiation at multiple angles and polarization states and further motivate the need for a comprehensive comparison of dust models used by current retrieval algorithms.

In this section, we attempt to provide an overall summary of dust models applied in several aerosol retrieval algorithms widely used by the science community. These include algorithms related to both passive and active sensors. The summary provides a brief description of the sensor, the strategy behind the retrieval algorithm, the specific steps used to detect and characterize dust, and the key inputs (spectral refractive indices, size parameters/distributions, number of size modes, shape parameters/distributions, etc.) needed for describing the dust model and other relevant aerosol models. These inputs are supplied by literature or personal communication. We also summarize key similarities and differences in dust models assumed between the different algorithms. Specific sensors/algorithms we describe here include 1)

AERONET almucantar inversions, 2) various MODIS algorithms including Dark Target-ocean, Dark Target-land, Deep Blue-land, SOAR-ocean, MAIAC-land, and continuity and differences regarding MODIS algorithms ported to the Visible Infrared Imaging Radiometer Suite (VIIRS), 3) MISR standard and research algorithms, 4) OMI OMAERUV algorithm, and 5) algorithms applied to the backscatter lidars Cloud-Aerosol Lidar with Orthogonal Polarization (CALIOP) and Cloud-Aerosol Transport System (CATS).

### 4.1 Remote Sensing Representations of Particle Size Distributions

As aerosols in nature are not monodisperse, they are characterized by a particle size distribution (PSD), usually expressed as functions of radius $r$ or diameter $D$. PSDs may be defined in terms of number (nPSD as $n(r)$ or $n(D)$ ), cross-sectional area (aPSD) or volume (vPSD). PSD can also be defined via mass, where mass and volume are interchangeable if the particle's density (mass per volume) is independent of size. Unfortunately, there is often confusion when comparing descriptions of size distributions because different aerosol science communities tend to use different combinations of nPSD, vPSD, or aPSD, as functions of $r$ or $D$ to define PSDs. The remote sensing community tends to define via $r$, and are evenly split between using nPSD and vPSD, whereas $D$ is usually used when reporting in-situ measurements. One other key difference between remote sensing and in-situ science communities is that in remote sensing PSDs are often defined in terms of the quantity of particles in the entire atmospheric column (e.g., the number of particles above a unit area of the ground) rather than particle concentration at a particular location within the atmosphere. In the following, we will report PSDs as a function of $D$ to be consistent with the rest of this review.

It is convenient to model PSDs by continuous mathematical functions, and it is very common in remote sensing aerosol models to assume that PSDs are superpositions of multiple modes, where each mode is approximated by a lognormal distribution (LND). Being lognormal, each mode is easily described by a normal distribution of the logarithm of the particle size ($l = ln\ D$):

$$n_l(l) = \frac{dN(l)}{dl} = \frac{dN(ln\ D)}{d\ (ln\ D)} = \frac{N_0}{\sqrt{2\pi}}\frac{1}{\sigma} exp\left[-\frac{(l-\mu)^2}{2\sigma^2}\right] \qquad \text{Eq 6.}$$

where $N_0$ is the total number of particles, defined as the integral of the number density distribution $n(l)$ over infinitesimal bins of size $dl$:

$$N_0 = \int_{l=-\infty}^{l=\infty} n_l(l)dl = \int_{ln\ D=-\infty}^{ln\ D=\infty} \frac{dN(ln\ D)}{d(ln\ D)} d\ ln\ D \qquad \text{Eq 7.}$$

and $\mu$ and $\sigma$ are the mean and standard deviation of the log-diameter $l$, respectively:

$$\mu = \frac{1}{N_0}\int_{l=-\infty}^{l=\infty} l\ n_l(l)dl \qquad \text{Eq 8.}$$

$$\sigma = \sqrt{\frac{1}{N_0}\int_{-\infty}^{\infty} (l-\mu)^2 n_l(l)dl} \qquad \text{Eq 9.}$$

We use LNDs because they have the convenient property that the arithmetic mean, median, and mode of the log-diameter have the same values ($\mu = \tilde{l} = l_M$). Moreover, the standard deviation in log-diameter is the same for all xPSD (e.g., $\sigma_a = \sigma_v = \sigma$). Thus, with $\mu$ and $\sigma$, we have everything we need to know about a lognormal mode. Table 1 shows how properties commonly reported in the literature of the nPSD in linear diameter space can be calculated from $\mu$ and $\sigma$, including the arithmetic mean diameter $\overline{D}$, median $\widetilde{D}$ and mode $D_M$.

Table 1. Conversion of metrics that describe a LND with mean log-size $\mu$ and standard deviation $\sigma$. The equations for volume- and area-based metrics assume spherical particles.

| **Metric** | **Lognormal formulas** |
|---|---|
| Total number density $N_0$ | $N_0$ |
| Number median diameter $\widetilde{D}$ | $exp(\mu)$ |
| Number geometric mean diameter $D_g$ | $exp(\mu)$ |
| Number mode diameter $D_M$ | $D_M = exp\ (\mu - \sigma^2)\ = \widetilde{D}\ exp\ (-\sigma^2)$ |
| Number mean diameter $\overline{D}$ | $\frac{1}{N_0} N_0\ exp\ (\mu + \frac{\sigma^2}{2})\ =\ \widetilde{D}\ \ exp\ (\frac{\sigma^2}{2})$ |
| Variance $\sigma_0^2$ | $\widetilde{D}^2\ exp\ (2\sigma^2)\ -\ \widetilde{D}^2\ exp\ (\sigma^2)\ = \widetilde{D}^2\ exp\ (\sigma^2)\ [\ exp\ (\sigma^2) - 1\ ]$ |
| Total cross-sectional area density $A_0$ | $\pi N_0\ exp\ (2\mu +\ 2\sigma^2)\ =\ \pi N_0\ \widetilde{D}^2\ exp\ (2\sigma^2)$ |
| Total volume density $V_0$ | $\frac{\pi}{6} N_0\ exp\ (3\mu +\ 4.5\sigma^2)\ = \frac{\pi}{6} N_0\ \widetilde{D}^3\ exp\ (4.5\sigma^2)$ |
| Area median diameter $\widetilde{D}_a$. | $exp\ (\mu_a)\ = exp\ (\mu + 2\sigma^2)\ = \widetilde{D}\ exp\ (2\sigma^2)$ |
| Volume median diameter $\widetilde{D}_v$ | $(\mu + 3\sigma^2) = \widetilde{D}\ exp\ (3\sigma^2)$ |
| Area-weighted mean diameter $\overline{D}_a$ | $\widetilde{D}_a\ exp\ \left(\frac{1}{2}\sigma^2\right)\ = \widetilde{D}\ exp\ (\frac{5}{2}\sigma^2)$ |
| Volume-weighted mean diameter $\overline{D}_v$ | $\widetilde{D}_v\ exp\ \left(\frac{1}{2}\sigma^2\right)\ = \widetilde{D}\ exp\ (\frac{7}{2}\sigma^2)$ |
| Effective diameter $D_e$ | $\frac{exp\ (3\mu +\ 4.5\sigma^2)}{exp\ (2\mu +\ 2\sigma^2)} = \widetilde{D}\ exp\ (2.5\sigma^2)$ |
| Effective variance $v_e$ | $exp\ (\sigma^2) - 1$ |

In many cases, aerosol PSDs are modeled by combinations of $j$ lognormal modes, with some fractional weighting $\eta$ between the modes. The fractional weighting may be in terms of number ($\eta_{n,j}$), volume ($\eta_{v,j}$), or extinction ($\eta_{\lambda,j}$) at a particular wavelength (e.g., $\lambda$ = 0.55 μm). For example, many remote sensing algorithms assume that most aerosol PSDs can be represented by a combination of one *fine* ($D_e$< 1.0 μm) and one *coarse* mode ($D_e$>1.0 μm). Each mode $j$ $(= f\ or\ c)$ has its own combination of size distribution (e.g., $\widetilde{D}_j$, $\sigma_j$,) and refractive indices ($n_{j,\lambda} = m_{j,\lambda} + ik_{j,\lambda}$). When there are only two modes, the fractional weighting is referred to as *fine mode weighting* (FMW) or *fine mode fraction* (FMF). Note the possibility of confusion because different algorithm teams define this FMF or FMW in terms of number, volume, or extinction (for a given wavelength). See the Supplementary Documentation for additional discussion on calculating aerosol single scattering properties described by lognormal distributions.

### 4.2 AERONET Ground-Based Sun Photometer

Sometimes referred to as the “ground-based satellite”, the basis of AERONET is a federated, globally distributed network of CIMEL Electronique CE318 multiband sun photometers (Holben et al., 1998). Many AERONET sun photometers have been deployed in dust regimes, including on Cape Verde, which frequently samples the Saharan dust outflow. The AERONET site on Cape Verde, operated since 1994, has contributed significantly to a primary dataset of dust properties. Many satellite retrieval algorithms leverage the AERONET retrieval data from Cape Verde and other locations directly, both for creating dust (and other aerosol) models as well as for satellite retrieval product validation.

The multiband sun photometer employed by AERONET performs measurements of spectral sun irradiance and sky radiance. The basic sensor includes eight filters at 1020, 936, 870, 675, 500, 440, 380, and 340 nm, and the ability to perform measurements in sun mode (pointing directly at the sun) or sky mode (almucantar and principal plane radiance measurements). Since 2004, most sensors have been replaced with upgraded versions, having additional capabilities such as measuring polarization, additional wavelengths (e.g., 1640 nm), and improved tracking and robotic control (https://aeronet.gsfc.nasa.gov/new_web/system_descriptions_instrument.html) (Sinyuk et al., 2020).

The AERONET sun mode observation directly measures the water vapor total column (WV) from the 936 nm channel, and spectral AOD from the remaining channels. Dubovik et al. (2006; 2000) developed a retrieval algorithm to invert a column effective aerosol PSD, complex refractive index, and fraction of spherical particles from sky mode observations that was based on the work of Nakajima et al. (1996, 1986, 1983). The complex refractive index is assumed to be size invariant in the retrieval. From these retrieved parameters, additional optical properties are derived for several wavelengths, including the single scatter phase function at 83 scattering angles $P_{11}(\theta, \lambda)$, single scattering albedo $\omega(\lambda)$, and asymmetry parameter $g(\lambda)$. Details of the AERONET retrieval algorithm are summarized in the Supporting Documentation.

Notably, the AERONET sky mode inversion algorithm uses a precomputed database of single scattering properties of spheroids with a fixed axis ratio distribution to represent dust scattering that is documented in Dubovik et al. (2006). This is the same database packaged within the freely available GRASP code. The AERONET assumption for fixed axis ratio distribution $N(\varepsilon)$ of 25 axis ratios $\varepsilon$ is shown in Figure 6 (see Dubovik_25 values and Table S1 for specific values). By adding a volume fraction *f* of spherical particles ($\varepsilon = 1.0$) to the spheroids, the AERONET inversion algorithm leads to a satisfactory fit to the observed radiances in almost any case. These assumptions are used for the current Version 3 dataset  (Sinyuk et al., 2020), and are also adopted by several remote sensing algorithms surveyed for this paper and described below.

The original AERONET retrieval algorithm represented dust as spherical particles (Dubovik and King, 2000), which resulted in substantial errors to the retrieved volume size distribution and index of refraction for dust particles. The reason for these errors is that the phase function of spheroids exceeds that of volume-equivalent spheres at intermediate scattering angles. This contrast can be important at the angles where radiances are measured by AERONET sun photometers.

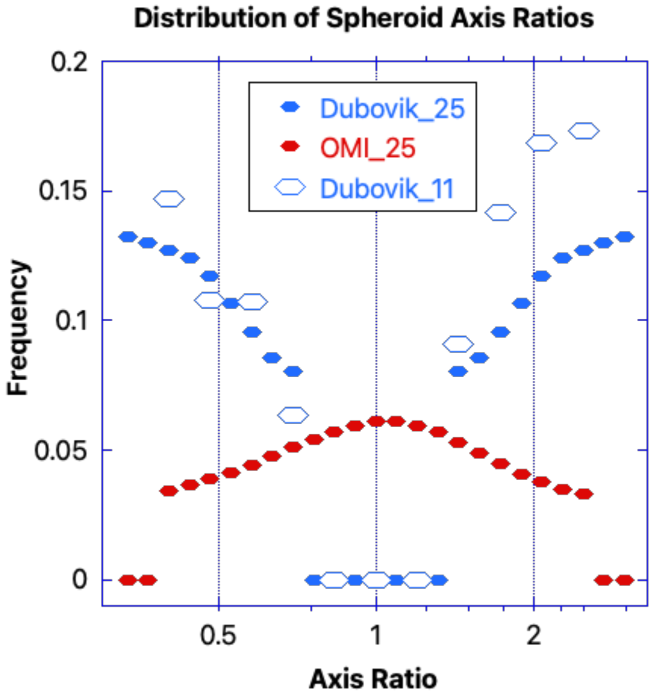

Figure 6. Distribution of axis ratios used by the remote sensing dust models described in this paper. Dubovik_25 is the 25-axis ratio spheroid distribution of Dubovik et al. (2006), assumed for the AERONET retrieval. Dubovik_11 is the 11-axis ratio spheroid distribution used by the DT-land retrieval (see Section 4.3). OMI_25 is the 25-axis ratio spheroid distribution used by the OMAERUV retrieval (see Section 4.6). Note that an axis ratio equal to one represents a sphere.

***Retrieved Size Distribution***

| ***Size Parameter*** | ***Mode*** | |
|---|---|---|
| | **Fine** | **Coarse** |
| **Volume Concentration ($C_v$)** | 0.094 | 1.593 |
| **Effective Diameter ($D_e$ [μm])** | 0.496 | 3.102 |

| | | |
|---|---|---|
| **Volume Median Diameter ($\widetilde{D}_v$ [µm])** | 0.582 | 3.594 |
| **Log-size standard deviation ($\sigma$)** | 0.481 | 0.534 |
| **Inflection Diameter ($D_{inf}$ [µm])** | 0.878 | |
| **Spherical Fraction (*f*)** | 0.0 | |

***Retrieved Optical Properties***

| ***Parameter*** | ***Wavelength* [nm]** | | | |
|---|---|---|---|---|
| | **440** | **675** | **870** | **1020** |
| **Sun-mode AOD** | 2.793 | 2.748 | 2.617 | 2.500 |
| **Real Refractive Index (*m*)** | 1.4749 | 1.4469 | 1.4379 | 1.419 |
| **Imaginary Refractive Index (*k*)** | 0.00377 | 0.00055 | 0.00059 | 0.0005 |
| **Extinction ($k_{ext}$) [km$^{-1}$]** | 2.826 | 2.766 | 2.628 | 2.512 |
| **SSA ($\omega_0$)** | 0.913 | 0.989 | 0.990 | 0.993 |
| **Asymmetry Parameter (*g*)** | 0.819 | 0.773 | 0.761 | 0.765 |
| **Lidar Ratio (*S*)** | 70.025 | 54.469 | 55.045 | 60.559 |
| **Lidar Depolarization Ratio ($\delta$)** | 0.296 | 0.314 | 0.323 | 0.332 |
| **Extinction FMF ($\eta$)** | 0.274 | 0.171 | 0.112 | 0.079 |

Table 2. AERONET retrieved PSD and optical parameters for the 9 Mar 2006 Cape Verde inversion. Note that original products in terms of radius have been converted to diameter. The AOD Fine Mode Fraction ($\eta$) represents the fine mode contribution to the total extinction. Additional parameters not reported in Table 2, but reported by AERONET include the original vPSD, $P_{11}$, $-P_{12}/P_{11}$, and higher order scattering functions.

Table 2 lists some of the retrieved size properties and observed and derived optical properties reported by AERONET for a dust plume observed at Cape Verde on 9 March 2006 at 10:24 UTC. For illustrative purposes, we adopted the scattering code utilized by the AERONET retrieval, referred to here as the "DSL" code in reference to its main developers Dubovik, Sinyuk, and Lapyonik) (Dubovik et al., 2006), as the forward model (the reverse of the AERONET inversion) to re-derive the AERONET properties.

As inputs, we took the reported AERONET PSD and refractive index parameters from Table 2 and use the same combination of 25 axis ratios as assumed for the inversion (Dubovik_25 values in Figure 6). We do this calculation twice, once with the assumption that there are separate fine and coarse lognormal modes (each having its own mean radius and standard deviation, but the same refractive index), and a second time using the retrieved total vPSD. In other words, as many satellite algorithms assume lognormal approximations, we compare the impact of assuming two lognormal modes versus an explicit unparameterized size distribution, to investigate the degree to which the output differences may be significant. Selected retrieval parameters are compared in Figure 7. Note that the vPSD is normalized to reflect a unit AOD (i.e., AOD = 1.0)

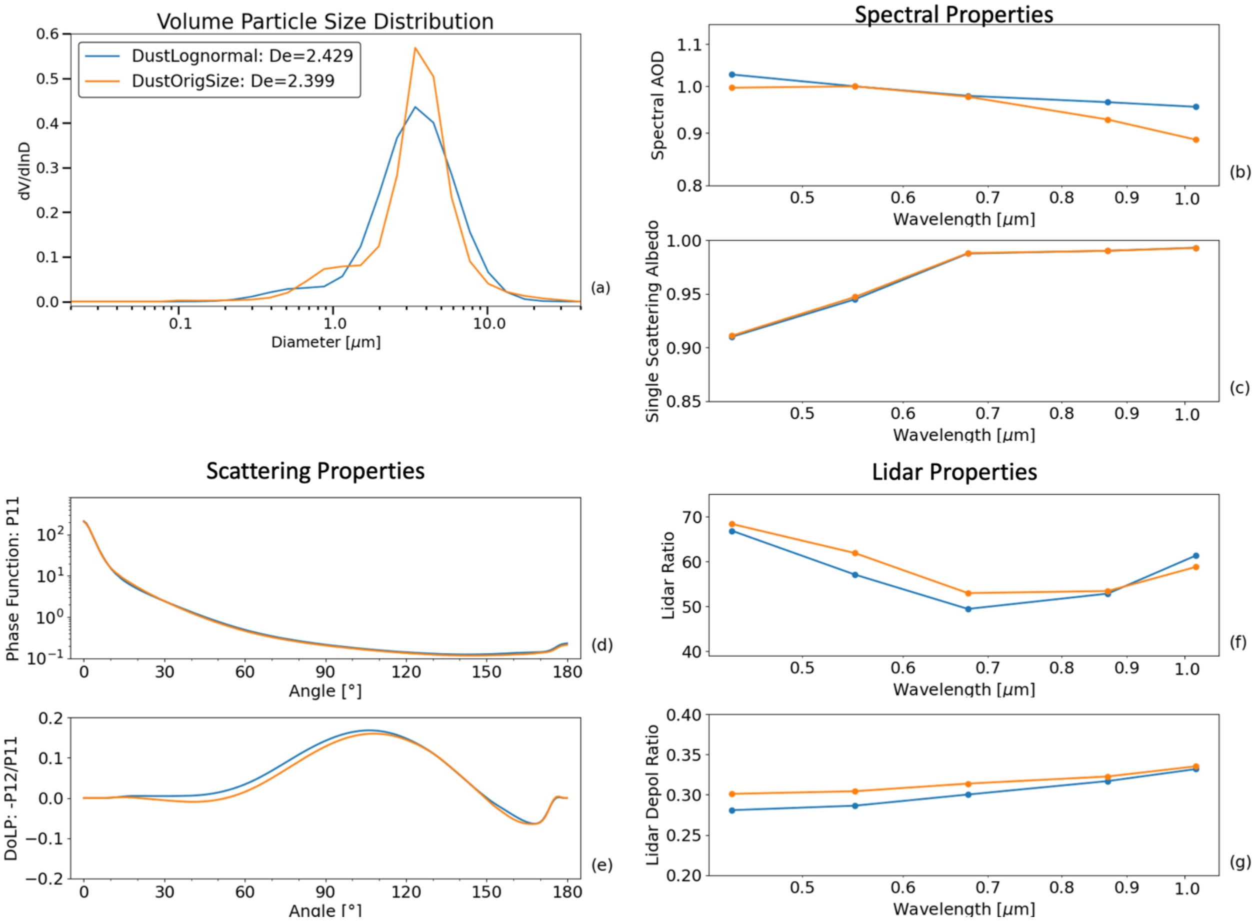

Figure 7. Revisiting the Lee et al., (2017) dust case at Cape Verde: (a) volume PSD assuming two lognormal modes (blue) and original retrieved total vPSD (orange), (b) spectral AOD, (c) spectral SSA, (d) phase function $P_{11}$ at 0.55 $\mu$m, (e) DoLP (-P12/P11) at 0.55 $\mu$m, (f) spectral lidar ratio, and (g) spectral lidar depolarization ratio ($\delta_L$).

Figure 7 shows how the differences in input vPSDs propagate throughout the DSL calculations. Even though the size distributions appear different (note appearance of a 'medium' mode around D=1 $\mu$m for the original retrieved size distribution in orange) (panel a), the effective diameters are nearly the same; 2.42 $\mu$m (DustLogormal) versus 2.40 $\mu$m (DustOrigSize). Most of the retrieved optical parameters are also very similar, although the bimodal lognormal distribution does lead to stronger spectral dependence in AOD (panel b), and minor differences in $P_{11}$ at 0.55 µm (panel d) in this case. Note that if P11 were plotted in linear scale, one would see sufficient differences in $P_{11}$ to lead to differences in spectral asymmetry parameter (not plotted) and spectral lidar ratio (panel f). Estimated DoLP ($-P_{12}/P_{11}$) values (panel f) show small differences and so does the spectral lidar depolarization ratio ($\delta_L$) (panel g). These differences illustrate the sensitivity of optical properties to relatively small changes in the underlying dust model size distribution assumptions. However, an important assumption here is that when the size distribution is represented by two modes, both modes have the same refractive indices. This probably helps minimize the differences in simulated optical properties between the two approaches, whereas in many real-world cases, there would be significant compositional differences between the fine and coarse-dominated components of the size distribution (e.g., smoke and dust; Samset et al., 2018; Schuster et al., 2016).

### 4.3 Passive Aerosol Retrieval (Single Angle, VIS/NIR/SWIR)

Although passive satellite remote sensing in the visible and near-infrared wavelength range has a long history, we limit this discussion to the currently flying MODIS that has been observing since 2000 (Salomonson et al., 2002) and VIIRS observing since 2011 (Hillger et al., 2013). We start with the MODIS aerosol retrieval algorithms, focusing specifically on the assumptions and approaches that are related to identifying and retrieving AOD when dust is present. Myriad of customized algorithms and techniques have been applied to MODIS observations to retrieve AOD, often optimized to a specific location or condition, but here we focus on global algorithms applied to the full MODIS data record. In addition, there are algorithms for detecting and retrieving aerosols for the purpose of atmospheric correction (AC) needed for land and/or ocean surface retrievals (e.g., Ibrahim et al., 2019; Vermote and Kotchenova, 2008), but in most cases these algorithms will retrieve aerosol information only if the scene might be appropriate for AC – in such algorithms, thick aerosol plumes including dust tend to be screened out. Therefore, we focus only on the algorithms specifically tasked with aerosol retrieval over many conditions, namely the 'Dark Target', 'Deep Blue', and 'MAIAC' algorithms for MODIS and/or VIIRS observations. For reference, Table S2 lists the MODIS and VIIRS wavelengths used for Dark Target, Deep Blue, and/or MAIAC retrievals. In the following, we report on the dust models used in each algorithm, and not the differences in algorithms due to differences in Rayleigh scattering, surface reflectance, gas absorption, or other non-aerosol constituents assumed within the aerosol retrieval algorithms.

### 4.3.1 Dark Target over land and ocean (MODIS and VIIRS)

The Dark Target (DT) aerosol retrieval algorithms exploit the relative contrast of 'bright' aerosol over a 'dark' background in the blue, green, red, NIR, and the three SWIR bands shown in Table S2. DT is separated into over-ocean (DT-O) and over-land versions (DT-L), the path chosen by a geolocation land/sea flag. DT uses the look-up-table (LUT) approach, where LUTs contain radiative transfer (RT) simulations of TOA spectral reflectance, calculated for each band's centroid reflectance value. By matching the LUTs with the spectral observations, the DT algorithm obtains solutions that represent the most likely aerosol conditions. Solutions represent total loadings of a mix of fine (e.g., effective diameter $D_e << 2.0$ μm), and coarse particles ($D_e \geq$

2.0 µm). Retrieved parameters include total AOD (at 0.55 µm), and fine model fraction (FMF, in terms of AOD at 0.55 µm). Over land, there is specifically a dust model, whereas over ocean, dust is inferred from the combination of retrieved AOD and FMF. Currently, DT is used for the latest version of MODIS aerosol products, Collection 6.1 (Wei et al., 2019), and by accounting for wavelength band shifts (Table S2), has been ported to additional sensors including VIIRS (Sawyer et al., 2020).

#### 4.3.1.1 DT-Ocean

The DT-O algorithm uses the ocean surface in green (0.55 µm) and longer reflective window bands as the 'dark' surface. DT-O assumes that ambient aerosol is a combination of exactly one fine and one coarse lognormal mode. The mathematical inversion searches LUTs to find a solution that combines the optical properties of possible fine and coarse modes to fit the observations. The sum of the two mode loadings is the total AOD at 0.55 µm, and their relative AOD weighting is the FMF. Note that due to differing spectral dependence of AOD between fine and coarse modes, FMF will vary by wavelength, but for DT-O, FMF is defined at 0.55 µm.

The retrieval considers nine theoretical aerosol models defined according to data from an early climatology of AERONET sun photometers (Holben et al., 1998) located near water bodies, and adjustments based on analyses and validation of retrieval products from the MODIS data record. Specifically, there are four fine models (F1-4) and five coarse models (C5-9), which all assume spherical particles (properties for all models are listed here http://darktarget.gsfc.nasa.gov/algorithm/ocean/aerosol-models, and properties for a few selected models are listed in Table 3). Spectral aerosol optical properties are calculated for each aerosol mode at seven wavelength bands (blue, green, red, NIR, and three SWIR) and are shown in Figure S1.

| | **Lognormal Distribution Parameters** | | **Complex Refractive Index** | | | | | | | |
|---|---|---|---|---|---|---|---|---|---|---|
| **Model** | | | **0.47 – 0.86 µm** | | **1.24 µm** | | **1.63 µm** | | **2.11 µm** | |
| | **$\widetilde{D}$ (µm)** | **σ** | ***m*** | ***k*** | ***m*** | ***k*** | ***m*** | ***k*** | ***m*** | ***k*** |
| **F4**<br>spherical | 0.2 | 0.6 | 1.40 | 0.002 | 1.40 | 0.002 | 1.39 | 0.005 | 1.36 | 0.003 |
| **C6**<br>spherical | 1.2 | 0.6 | 1.35 | 0.001 | 1.35 | 0.001 | 1.35 | 0.001 | 1.35 | 0.001 |
| **C8**<br>spherical | 1.2 | 0.6 | 1.53 | 0.47 µm: 0.003<br>0.55 µm: 0.001<br>0.65 µm: 0.000<br>0.86 µm: 0.000 | 1.46 | 0.000 | 1.46 | 0.001 | 1.46 | 0.000 |
| **C9**<br>spherical | 1.0 | 0.8 | | | | | | | | |
| **M10**<br>spheroidal – Dubovik_25 | 1.0 | 0.6 | | 0.47 µm: 0.003<br>0.55 µm: 0.001<br>0.65 µm: 0.0005<br>0.86 µm: 0.0005 | | 0.0005 | | | | 0.0005 |

Table 3. Size distribution parameters for select DT-O aerosol models. The F4 and C6 models are typically chosen by the retrieval for Saharan dust outflow. The C8 and C9 models were created to represent dust. The M10 model refers to the new spheroidal dust model introduced by Zhou et al. (2020).

Thus, the goal of the DT-O retrieval is to find which of the 20 combinations of F1-4 and C5-9 best match the observations. Out of the coarse models, two (C8 and C9) were created to represent "dust". They have spectral real refractive indices (~1.53 in the visible) and size distributions that are in line with observations of airborne dust. However, the retrieval can pick any coarse mode model, and in fact, combinations using C8 or C9 are rarely found for Saharan dust outflow. Rather, the retrieval often chooses a combination that mixes F4 and C6 with a FMF between 0.15 and 0.30 (i.e., F4mixC6_FMF0p15 and F4mixC6_FMF0p30 in Figure 8). The effective size distribution and complex refractive index of mixtures of F4 and C6 with FMF equal to 0.15 and 0.30 are shown in Figure 8 and Table 4.

Recently, Zhou et al. (2020) introduced a 'detect then retrieve' approach to DT-O, which forces the retrieval to use a new dust model referred to as M10 (Table 3). This dust model has refractive index and log-size standard deviation similar to C8. However, it assumes a reduced number median diameter ($\widetilde{D}$=1.0 µm vs $\widetilde{D}$=1.2 µm for C8) and the Dubovik_25 spheroid distribution for the shape model (same as the Version 3 AERONET retrievals) (Figure 6) (Sinyuk et al., 2020). The size distribution for the M10 model is also shown in Figure 8.

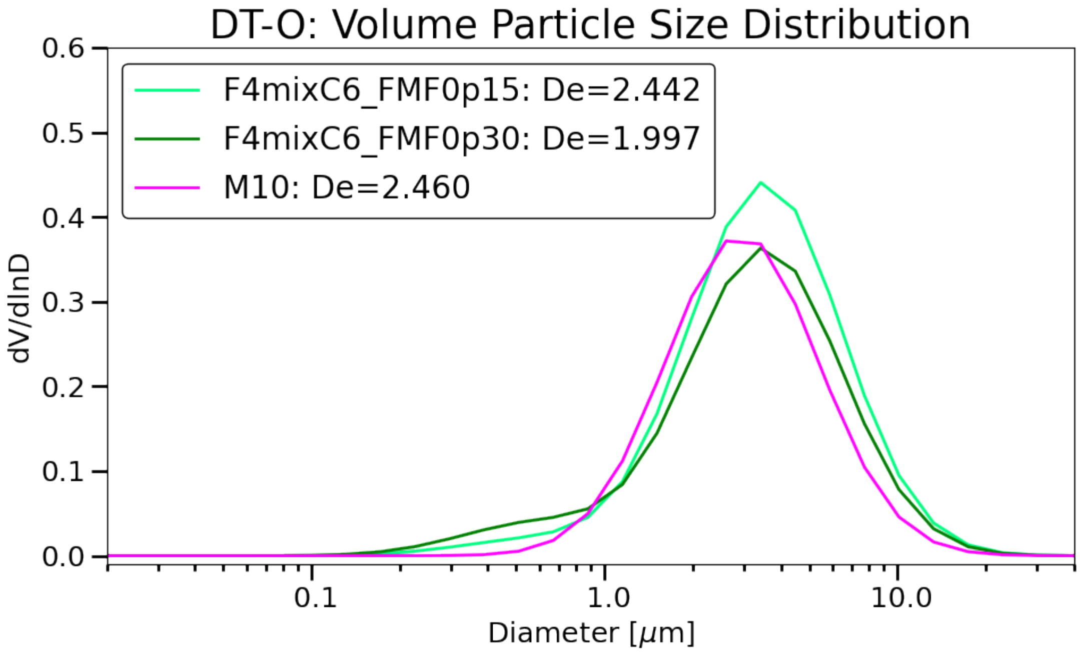

Figure 8. The effective volume particle size distribution of DT-O dust models, displayed for unit AOD at 0.55 $\mu$m. F4mixC6_FMF0p15 and F4mixC5_FMF0p30 refer to mixtures of the F4 and C6 aerosol models with FMF equal to 0.15 and 0.30, respectively. These mixtures are typically chosen by the retrieval for Saharan dust outflow. The M10 model refers to the new spheroidal dust model introduced by Zhou et al. (2020).

| **Dust Model** | **Refractive Index** | **Wavelength [MODIS/VIIRS]** | | | | | | |
|---|---|---|---|---|---|---|---|---|
| | | **0.47/ 0.49 µm** | **0.55/ 0.55 µm** | **0.65/ 0.67 µm** | **0.86/ 0.86 µm** | **1.24/ 1.24 µm** | **1.63/ 1.61 µm** | **2.11/ 2.26 µm** |
| | Real *m* | 1.359 | 1.358 | 1.356 | 1.354 | 1.352 | 1.351 | 1.350 |

| | | | | | | | | |
|---|---|---|---|---|---|---|---|---|
| **F4mixC6_ FMF0p15** | Imaginary *k* | 0.00170 | 0.00150 | 0.00122 | 0.00108 | 0.00104 | 0.00110 | 0.00102 |
| **F4mixC6_ FMF0p30** | Real *m* | 1.367 | 1.365 | 1.362 | 1.359 | 1.355 | 1.352 | 1.350 |
| | Imaginary *k* | 0.00134 | 0.00130 | 0.00125 | 0.00117 | 0.00110 | 0.00123 | 0.00106 |

Table 4. The effective imaginary refractive index of DT-O dust models reported at MODIS/VIIRS wavelengths. F4mixC6_FMF0p15 and F4mixC5_FMF0p30 refer to mixtures of the F4 and C6 aerosol models with FMF equal to 0.15 and 0.30, respectively. These mixtures are typically chosen by the retrieval for Saharan dust outflow. Note that for reporting the spectral refractive index of the mixtures, we weight by the FMF at that given wavelength.

#### 4.3.1.2 DT-Land

The DT-L algorithm also relies on the contrast between aerosols above a dark surface below. The retrieval is based on the assumption that vegetation appears dark in blue (e.g., 0.47 μm), red (0.65 μm) and mid-SWIR (2.11 μm) channels, and that the surface reflectance in one band is a known ratio of the surface reflectance in the other two bands (Kaufman et al., 1997). By assuming that one can constrain the surface using the ratios, one can isolate the aerosol information. Because vegetation reflectance is so bright at 0.55, 0.86 and 1.24 μm, there are fewer available bands for retrieval, and thus fewer degrees of freedom in the retrieval. Thus, unlike DT-O where the retrieval is free to mix any fine and coarse aerosol model, the DT-L algorithm must make further assumptions.

DT-L prescribes one of three ‘fine-dominated’ spherical aerosol models comprised of two lognormal modes based on meteorological season and geographical location. These aerosol models are based on a cluster analysis of AERONET Version 1 retrievals in non-dusty regions (Levy et al., 2007), and each has more volume (and number) in the fine mode (De << 2.0 μm) than in the coarse mode. The seasonal map of fine-dominated aerosol models was implemented in the Collection 5 version of the MODIS aerosol dataset (Levy et al., 2009), and modified for the Collection 6 version (Levy et al., 2013), and retained for C6.1.

In the retrieval, the inversion mixes via FMF at 0.55 µm the prescribed fine-dominated aerosol model with a bi-modal dust (coarse-dominated) model, which is based on the climatology of non-spherical AERONET (Version 1) retrievals over known dusty regions. Unlike the fine-dominated models, which are spherical, the coarse-dominated dust model uses the spheroidal assumptions of Version 1 of the AERONET inversion code (Dubovik et al., 2002). Specifically, the spheroidal distribution is a weighting of volume equivalent spheroids with 11 axis ratios covering the axis ratio range from 0.3 to 3.0 (see Figure 6 Dubovik_11 values and Table S3). Note that as the dust model is mixed with the prescribed fine-dominated model, this leads to an AOD and FMF solution having four lognormal modes. However, for heavy dust conditions, the algorithm tends to derive an FMF close to zero, meaning essentially the dust model alone.

All aerosol models in DT-L are ‘dynamic’, meaning their properties (size and complex refractive index) depend on the AOD (Remer and Kaufman, 1998). This is based on an empirical analysis of AERONET retrievals, which showed that AOD and aerosol size (especially fine-mode radius) are correlated, presumably because of hygroscopic effects (swelling) and proximity to the emissions source. This correlation can be explained by the fact that for small size parameters (<5) the extinction coefficient monotonically increases with size parameter. This dynamic aspect is kept in the DT-land aerosol models, so that physical and optical properties for a given model choice depend on the AOD. Although the dust model is much less dynamic than the fine-dominated models, there is still some dependence on AOD.

The PSD properties and refractive indices of each of the three fine-dominated and one coarse-dominated (dust) model are reported here https://darktarget.gsfc.nasa.gov/algorithm/land/aerosol-models, and the dust model properties are also listed in Table 5. The total effective size distribution and complex refractive index for the dust model is shown for several AOD values in Figure 9 and Table 6, respectively. Notably, the effective diameter decreases slightly with AOD, as the analysis of AERONET dust retrieval climatology showed a small increase in the contribution of particles with D < 0.1 μm.

| **Mode** | $\widetilde{D}_v$ **(μm)** | **σ** | **$V_0$ (μm³/μm²)** |
|---|---|---|---|
| **Fine**<br>spherical | $0.2832\tau^{-0.0519}$ | $0.7561\tau^{0.148}$ | $0.0871\tau^{1.026}$ |
| **Coarse**<br>spheroidal - Dubovik_11 | 4.4 | $0.554\tau^{-0.0519}$ | $0.6786\tau^{1.0569}$ |

Table 5. Particle size distribution properties of the DT-L dust model. Volume median diameter, log-size standard deviation, and total volume for the fine (accumulation) and coarse modes of the DT-L dust model. Note the dependence on AOD ($\tau$) which is defined at 0.55 μm. To compute when $\tau > 2.0$, the algorithm assumes $\tau = 2.0$.

| | | **Wavelength [MODIS/VIIRS]** | | | |
|---|---|---|---|---|---|
| **Mode** | | **0.47/0.49 μm** | **0.55/0.55 μm** | **0.65/0.67 μm** | **2.12/2.26 μm** |
| Fine | Real *m* | $1.48\tau^{-0.021}$ | $1.48\tau^{-0.021}$ | $1.48\tau^{-0.021}$ | $1.46\tau^{-0.040}$ |
| | Imaginary *k* | $0.0025\ \tau^{0.132}$ | 0.002 | $0.0018\ \tau^{-0.08}$ | $0.0018\ \tau^{-0.30}$ |
| Coarse | Real *m* | $1.48\tau^{-0.021}$ | $1.48\tau^{-0.021}$ | $1.48\tau^{-0.021}$ | $1.46\tau^{-0.040}$ |
| | Imaginary *k* | $0.0025\ \tau^{0.132}$ | 0.002 | $0.0018\ \tau^{-0.08}$ | $0.0018\ \tau^{-0.30}$ |
| | | | | | |
| **$AOD_{550}$** | | | | | |
| 0.25 | Real *m* | 1.524 | 1.524 | 1.524 | 1.543 |
| | Imaginary *k* | 0.0021 | 0.0020 | 0.0020 | 0.0027 |
| 0.5 | Real *m* | 1.502 | 1.502 | 1.502 | 1.501 |
| | Imaginary *k* | 0.0023 | 0.0020 | 0.0019 | 0.0022 |
| 1.0 | Real *m* | 1.480 | 1.480 | 1.480 | 1.480 |
| | Imaginary *k* | 0.0025 | 0.0020 | 0.0018 | 0.0018 |
| ≥2.0 | Real *m* | 1.459 | 1.459 | 1.459 | 1.420 |
| | Imaginary *k* | 0.0027 | 0.0020 | 0.0017 | 0.0015 |

Table 6. Spectral complex refractive indices for the fine (accumulation) and coarse modes used of the DT-L dust model, and the total effective complex refractive index for several values of AOD at 0.55 μm for MODIS/VIIRS wavelengths. Note the dependence on AOD ($\tau$) which is

defined at 0.55 µm. To compute when $\tau > 2.0$, the algorithm assumes $\tau = 2.0$. For reporting the spectral refractive index of the mixtures, we weight by the FMF at that given wavelength.

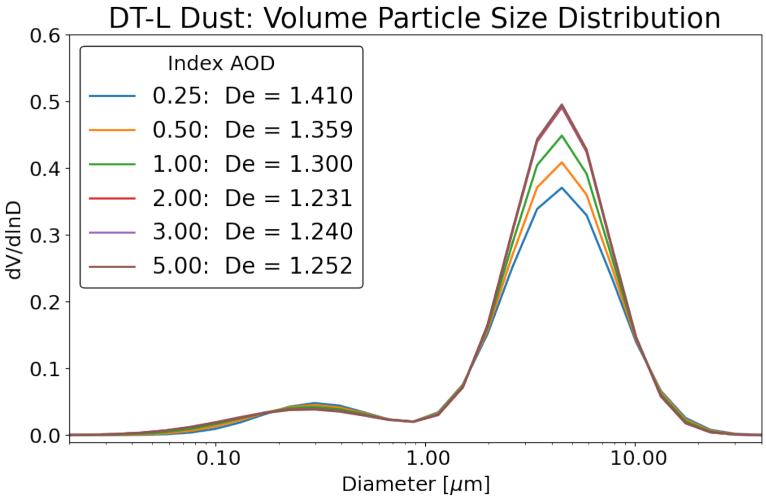

Figure 9. Properties of the dynamic DT-L dust model (derived for index AOD at 0.55 $\mu$m). Note that the plot shows the size distribution scaled by its AOD (e.g., total volume size distribution multiplied by its AOD value) to offset the curves for better visualization.

### 4.3.2 Deep Blue (MODIS and VIIRS) and SOAR (VIIRS) Algorithms

The Deep Blue algorithm over land (DB-L) was originally envisioned to retrieve over desert, semiarid, and other bright surfaces (Hsu et al., 2004) where DT-L is not applied. Over deserts, the reflectance in the near-UV (e.g., 0.41 µm or the "deep blue") is darker and more stable than the longer blue and red bands, and so can thereby be used as a surface for aerosol contrast. First implemented in the Collection 5 version of the MODIS dataset, over the years the DB-L algorithm has been enhanced to also retrieve aerosol properties over darker land surfaces including vegetation (Hsu et al., 2013), thus offering an alternative to DT-L. Additionally, the DB team has introduced retrievals over ocean using the Satellite Ocean Aerosol Retrieval (SOAR) algorithm (Sayer et al., 2012) in the VIIRS implementation of the Deep Blue algorithms. Thus for MODIS Collection 6.1 version, only the DB-L algorithm retrievals are included in the dataset, but the VIIRS implementation of the Deep Blue aerosol retrievals includes both DB-L and SOAR values (Hsu et al., 2019; Sayer et al., 2017).The SOAR algorithm takes a similar approach as the DB-O algorithm by assuming that ambient aerosol is characterized by a bi-modal distribution of one fine and one coarse lognormal mode, where the FMF is again defined by the 550 nm AOD. An inversion algorithm searches LUTs of forward model calculations of TOA reflectance at seven bands between 0.488 and 2.5 μm to find a solution that combines the optical properties of possible fine and coarse modes to fit the observations.

Similar to DT-L, the DB-L algorithm prescribes an aerosol model depending on regions and time of year (Hsu et al., 2019), whereas for the SOAR algorithm, the retrieval combines the dust-mode and fine-mode to best match the observations (Sayer et al., 2017). The dust models for both the DB-L and SOAR algorithms are based on statistics of AERONET inversion products (Version 2) over known dusty regions (Lee et al., 2017). The size distributions contain both fine and coarse lognormal modes. The fine mode is assumed spherical, and the coarse mode assumes the same spheroidal model as Dubovik et al. (2006) with fixed axis ratio distribution (Dubovik_25 in Figure 6). For DB-L, the FMF (of AOD at 0.55 μm) is fixed at 0.15. The assumed volume median diameter and log-size standard deviation ($\sigma$) for the fine and coarse mode lognormal distributions are listed in Table 7.

Figure 10 shows the SOAR size distribution for the coarse-mode model, fine-model model, and two mixtures of the coarse and fine-modes with nominal FMF values 0.15 and 0.30.

| **Mode** | $\widetilde{D}_v$ **(μm)** | $\sigma$ |
|---|---|---|

| | | |
|---|---|---|
| **Fine - SOAR & DB**<br>spherical | 0.38 | 0.44 |
| **Coarse - SOAR**<br>spheroidal - Dobovik_25 | 3.384 | 0.515 |
| **Coarse - DB**<br>spheroidal - Dubovik_25 | 3.392 | 0.515 |

Table 7. Volume median diameter ($\widetilde{D}_v$) and log-size standard deviation ($\sigma$) for the two modes of the dust aerosol model used in the SOAR and Deep Blue algorithms.

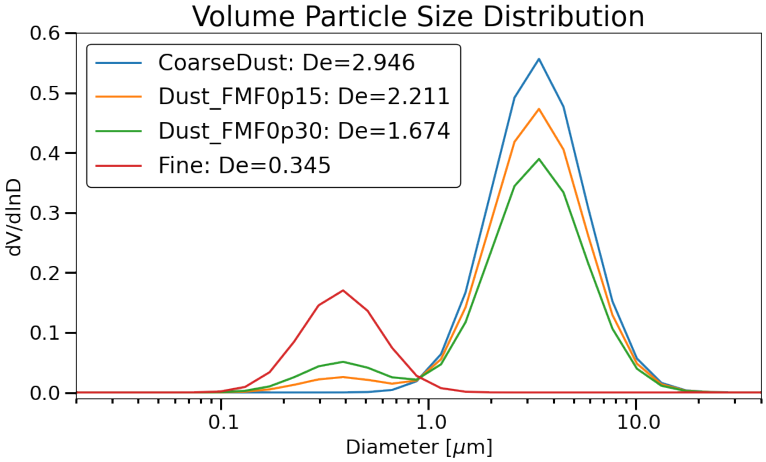

Figure 10. The total effective volume particle size distribution and effective diameter of SOAR dust models, plotted for unit AOD at 0.55 $\mu$m. Dust_FMF0p15 and Dust_FMF0p30 refer to mixtures of the coarse dust and fine-mode aerosol models with FMF (defined at 0.55 $\mu$m) equal to 0.15 and 0.30. The Dust_FMF0p15 curve is very similar to the DB-L dust model.

For the DB-L algorithm, the real part of the refractive index is assumed fixed at *m*=1.50 for the three wavelengths considered in the retrieval: the deep blue (0.41 $\mu$m for both MODIS and VIIRS), blue (0.47 or 0.49 $\mu$m) and red (0.65 or 0.67 $\mu$m). However, the imaginary part of the refractive index is allowed to vary for each wavelength and is represented by variable values of SSA in the retrieval LUT. Thus, the retrieval finds the SSA triplet in the deep blue, blue, and red that best matches the observations. A single complex refractive index value is assumed for both the coarse and fine modes. Table 8 lists the number and range of SSA nodes and corresponding ranges in complex refractive index in the DB-L algorithm LUTs.

Figure 11 shows the effect of the different SSA nodes (spanning the range of *k*) on particle scattering ($P_{11}$ and DoLP) properties at 0.41 $\mu$m as calculated by the DSL scattering code.

| **Wavelength MODIS/VIIRS** | **Number of nodes in LUT** | ***m*** | **$\omega$ range** | ***k* range** |
|---|---|---|---|---|
| 0.41/0.41 $\mu$m | 8 | 1.50 | $0.82 \leq \omega \leq 0.983$ | $0.0093 \geq k \geq 0.0005$ |
| 0.47/0.49 $\mu$m | 5 | 1.50 | $0.89 \leq \omega \leq 0.985$ | $0.0093 \geq k \geq 0.0005$ |
| 0.65/0.67 $\mu$m | 5 | 1.50 | $0.89 \leq \omega \leq 0.989$ | $0.0063 \geq k \geq 0.0005$ |

Table 8. Ranges for the single scattering albedo ($\omega$) and imaginary part of the complex refractive index ($k$) in the LUT for the DB algorithm dust model. The real part of the refractive index is fixed for all wavelengths.

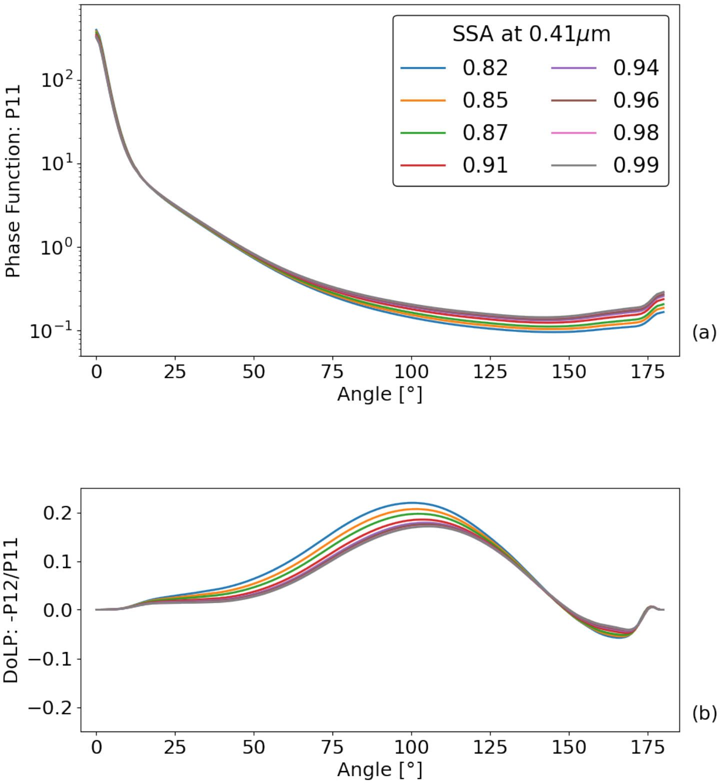

Figure 11. Properties of phase function (P11) and DoLP (-P12/P11) for the DB algorithm dust model at 0.41 $\mu$m as calculated by the DSL scattering code. Colors represent the index SSA for the eight nodes.

The spectral refractive indices for the SOAR algorithm coarse and fine-mode models are fixed (Table 9). However, as the retrieval combines fine and coarse-mode models to best match the observations, the effective refractive index can differ. In Table 9, we also list the SOAR effective refractive indices corresponding to FMF equal to 0.15 and 0.30.

| **Model** | **Refractive Index** | **0.49 $\mu$m** | **0.55 $\mu$m** | **0.67 $\mu$m** | **0.86 $\mu$m** | **1.24 $\mu$m** | **1.61 $\mu$m** | **2.26 $\mu$m** |
|---|---|---|---|---|---|---|---|---|
| Fine* | Real *m* | 1.43 | 1.43 | 1.43 | 1.43 | 1.41 | 1.4 | 1.38 |
| | Imaginary *k* | 0.001 | 0.001 | 0.001 | 0.001 | 0.001 | 0.001 | 0.001 |

| | | | | | | | | |
|---|---|---|---|---|---|---|---|---|
| Coarse* | Real *m* | 1.5228 | 1.5253 | 1.5301 | 1.5171 | 1.4963 | 1.4859 | 1.4701 |
| | Imaginary *k* | 0.00164 | 0.00107 | 0.0005 | 0.00051 | 0.0005 | 0.0005 | 0.0005 |
| FMF 0.15 | Real *m* | 1.5061 | 1.5110 | 1.5198 | 1.5120 | 1.4947 | 1.4851 | 1.4698 |
| | Imaginary *k* | 0.00153 | 0.00106 | 0.00055 | 0.00054 | 0.00051 | 0.00050 | 0.00050 |
| FMF 0.30 | Real *m* | 1.4906 | 1.4967 | 1.5082 | 1.5057 | 1.4924 | 1.4841 | 1.4695 |
| | Imaginary *k* | 0.00142 | 0.00105 | 0.00061 | 0.00057 | 0.00052 | 0.00051 | 0.00050 |

Table 9. Complex refractive index at VIIRS wavelengths for the SOAR algorithm dust model fine and coarse modes, and the effective refractive index for two mixtures of the fine and coarse modes with FMF values defined at 0.55 $\mu$m. For reporting the spectral refractive index of the mixtures, we weight by the FMF at that given wavelength.

*as found in Lee et al. (2017).

### 4.4 MAIAC

Instead of the single-view approach used by both DT and DB for MODIS, the Multi-Angle Instance of Atmospheric Correction (MAIAC) algorithm relies on the relative invariance of the surface properties over short time scales to help isolate the aerosol signal compared to the surface signal (Lyapustin et al., 2018, 2012). This, coupled with assumptions of spectral surface BRDF, allows the MAIAC algorithm to detect absorbing smoke and dust aerosol over land.

The smoke/dust detection algorithm described in Lyapustin et al. (2018, 2012) compares the measured reflectance at 0.41µm with that predicted for the red (0.65 µm) and blue (0.47 µm) bands using a background aerosol model. If absorbing aerosol is present, the measured aerosol reflectance at 0.41 µm will be lower than predicted by the background aerosol model due to both 1) more absorption caused by more multiple scattering at 0.41 µm, and 2) increased shortwave absorption (by brown and black carbon for smoke and by iron compounds for dust) as the imaginary part of the refractive index for these aerosols is higher at 0.41 µm than in the red-blue region. MAIAC limits dust detection to global regions where dust may be expected, including all major deserts and semi-arid regions (Sahara, Arabian Peninsula, Western U.S., southern Africa, Australia, and central Asia). Additional tests using infrared channels (4 μm and 11 μm channels) determine the thermal contrast (TH) which further helps separate dust from smoke in these regions.

Once dust is detected, MAIAC assumes a dynamic bimodal lognormal aerosol model that follows Dubovik et al. (2002), but with some empirical adjustments to the coarse mode radius and complex refractive index. This model, known as 'Model 6', has fixed fine and coarse mode median radii and standard deviations, but the ratio of fine and coarse mode volume is a function of AOD at 0.47 μm (see Table 10). For unit AOD = 1.0, this translates to 0.04/0.9 = 4.4% fine mode by volume. The MAIC dust model also assumes the Dubovik et al. (2006) spheroidal shape model with fixed axis ratio distribution (Dubovik_25 in Figure 6) for both modes. The total particle size distributions for various values of AOD are shown in Figure 12.

The MAIAC dust model assumes the same complex refractive index for the fine and coarse modes. The real part of the refractive index of the dust model is fixed at *m* = 1.56 in all bands, and the imaginary part of the refractive index is *k* = 0.001 for wavelengths greater than or equal to 0.66 μm. For wavelengths shorter than 0.66 μm, the spectral dependence of the imaginary part of the refractive index is defined by an assumed Absorption Ångström Exponent (AAE), which is set to 2.0 (see Table 11).

| **Mode** | $\tilde{D}_v$ **(μm)** | $\sigma$ | $\frac{C_v^{fine}}{C_v^{coarse}}$ |
|---|---|---|---|
| **Fine**<br>spheroidal - Dobovik_25 | 0.24 | 0.5 | $\frac{0.02(1+\tau_{0.47})}{0.9\tau_{0.47}}$ |

| | | | |
|---|---|---|---|
| **Coarse**<br>spheroidal - Dobovik_25 | 3.8 | 0.6 | |

Table 10. Particle size distribution properties of the MAIAC algorithm dust model based on Dubovik et al. (2002) including volume median diameter ($\widetilde{D}_v$) and log-size standard deviation ($\sigma$) for the fine and coarse modes and the ratio of the fine and coarse volume concentrations ($C_v^{fine}$ / $C_v^{coarse}$), which is a function of AOD at 0.47 µm ($\tau$).

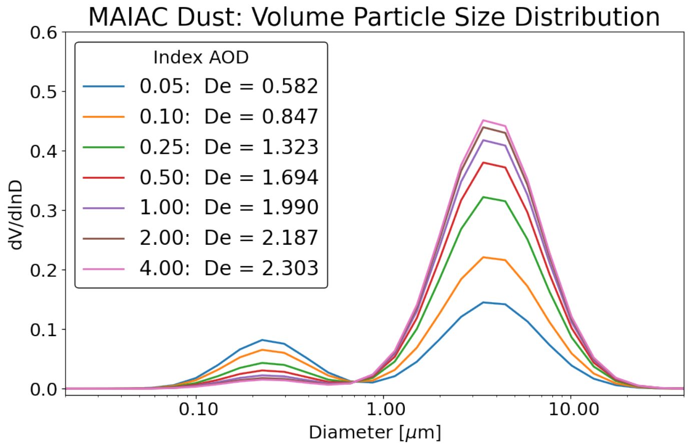

Figure 12. Total effective size distribution of the dynamic MAIAC dust model (derived for indexed AOD at 470 nm). Note that the plot shows size distributions scaled by their AOD (e.g., total volume size distribution multiplied by its AOD value) to offset the curves for better visualization.

| ***m*** | ***k*** | |
|---|---|---|
| **All Channels** | **λ < 0.66 µm** | **0.66 µm ≤ λ** |
| 1.56 | $\frac{0.001}{\left(\lambda/0.66\right)^{-AAE}}$<br>$AAE = 2.0$ | 0.001 |

Table 11. Complex refractive index properties of the MAIAC algorithm dust model. Note that the spectral dependence of *k* is defined by wavelength relative to 0.66 µm and an assumed Absorption Ångström Exponent (AAE = 2.0).

### 4.5 Passive Aerosol Retrieval (multiangle, VIS/NIR)

Multi-angle imagers measure radiance at multiple angles simultaneously, which provides additional constraints on aerosol properties in the retrieval. Therefore, the retrieval algorithm LUTs contain more degrees of freedom, and are constructed such that mixtures of multiple aerosol models can be chosen during the inversion (Martonchik et al., 2009). The fundamental goal of finding the most probable set of aerosol properties that fit the observations remains, but the actual measurements play a greater role in determining the reported aerosol properties.

In this section, we focus on dust models implemented for retrievals using the Multi-angle Imaging SpectroRadiometer (MISR) instrument, one of the first space-borne multi-angle, multi-wavelength imagers. It was launched aboard the Terra satellite in 1999 and continues to operate nominally. The instrument measures upwelling radiance at 446 nm (blue), 558 nm (green), 672 nm (red), and 866 nm (near-infrared, or NIR) (Diner et al., 1998). These measurements are taken for each of the nine MISR cameras, viewing in both the forward and aft directions along the satellite's orbit (±70.5°, ±60.0°, ±45.6°, ±26.1°, and 0.0° or nadir). As such, MISR observations sample a large range of scattering angles, between about 60° and 160° at midlatitudes, providing information about particle microphysical properties along with AOD and surface angular reflectance. MISR observations have been used in numerous aerosol studies for determination of AOD as well as aerosol type, a qualitative classification based on retrieved particle size, sphericity, and light-absorption-property constraints (Kahn et al., 2022; Kahn and

Gaitley, 2015; Martonchik et al., 2009). Future missions such as MAIA (Multi-Angle Imager for Aerosols), AOS, and PACE are building on this heritage.

### 4.5.1 MISR

For MISR, there is a Standard Algorithm (SA) used for global aerosol retrieval, and a research algorithm (RA), used to test retrieval concepts for possible application in the operational algorithm and for deriving more detailed aerosol characteristics in case studies. In the SA, there are 21 pre-defined lognormal models, and they are used to create 74 aerosol *mixtures*, where a mixture may be composed of number weighted fractions of 1, 2, or 3 of these models. Two of the models (so-called models #19 and #21) are meant to represent dust. Kalashnikova et al. (2005) and Kalashnikova and Kahn (2006) found that a medium sized, non-spherical aerosol type (model #19) tends to best fit dust-dominated observations over open water (transported dust), and a coarse sized aerosol type (model #21) sometimes fits better close to dust sources, although this ellipsoidal optical model is often a poor fit to the multi-angle, multi-spectral observations.

The medium-mode dust model (model #19) is assumed to be made up of grains that are modeled as aggregates of cubes (Kalashnikova et al., 2005). The scattering properties of this shape model are calculated using the Discrete Dipole Algorithm (DDA) (see Section 3.3.3). The shapes are based on electron microscope images of dust samples available at the time. The characteristic dimensions are the non-sphericity (NS = [particle surface area]/ [surface area of a volume-equivalent sphere]) and 3-D aspect ratio (3-D AR = longest/shortest dimensions). The model was constructed such that irregularity, measured by circularity (CIR = perimeter$^2$ / [4*π*area]), increases with particle size, also based on particle field observations available at the time. The MISR team ran the DDA only for the MISR green, red, and NIR spectral bands (i.e., excluding the blue band), because computational cost increases dramatically as the particle size parameter

($x$) increases. DDA calculations were run for $x \leq 12$, with maximum diameter of 2.0 µm. Over water, the SA uses only the red and NIR channels due to the darker surface at these wavelengths. Over-land, where the green and blue channels are also used, the phase function used for the blue channel is the one derived for the green wavelength, with the understanding that this is a limitation. The coarse-mode aerosols (model #21) are modeled as a mixture of prolate and oblate ellipsoids, and the scattering properties were generated with a T-Matrix code.

The size distributions of the dust models are represented by a number-weighted lognormal distribution, with properties shown in Table 12 (Kahn and Gaitley, 2015). Note that although the distributions are nominally lognormal, for calculating scattering properties, they are truncated on both the fine and coarse tails.

| **Dust Model** | $\widetilde{D}$ **(µm)** | $\sigma$ | $D_{min}$ **(µm)** | $D_{max}$ **(µm)** |
|---|---|---|---|---|
| **Medium-mode (#19)** grains | 1.0 | ln(1.5) | 0.2 | 2.0 |
| **Coarse-mode (#21)** ellipsoids | 2.0 | ln(2.0) | 0.2 | 12.0 |

Table 12. Size properties of the two dust models used in the MISR SA algorithm, including number median radius ($\widetilde{D}$), log-size standard deviation ($\sigma$), and minimum and maximum diameters ($D_{min}$ and $D_{max}$) used for calculating optical properties.

The dust composition assumptions for the two dust models are based on analysis of internally mixed hematite fractions of 1, 2, 4, and 10% by volume (Kalashnikova and Kahn, 2006). These values were based on laboratory measurements of hematite concentration in mineral dust samples available at the time. The analysis showed that over water, MISR observations can distinguish between weakly absorbing dust (1-4% hematite) and strongly absorbing dust (10%

hematite), but cannot discriminate among dust compositions having 4% hematite or less. As field campaign measurements at the time showed that both Saharan and Asian mineral dust contain less than 4% hematite, both the medium- and coarse-mode dust models used in the MISR SA assume 1% hematite. Note that there is a model #20 that is identical to model #19 for size and shape, but uses refractive indices representative of 4% hematite. However, it is not used in the current SA operational algorithm.

For the 1% hematite of both medium and coarse modes, the spectral complex refractive indices were calculated using the Bruggeman effective medium approximation (Sokolik and Toon, 1999) and are listed in Table 13. For the medium-mode particles, this yields SSA equal to 0.92, 0.98, 0.99, and 1.0 for the MISR blue, green, red, and NIR bands, respectively. For the coarse mode, the corresponding values are 0.81, 0.90, 0.97, and 0.98 (Kahn and Gaitley, 2015).

| **Refractive Index** | **Wavelength** | | | |
|---|---|---|---|---|
| | **0.446 µm** | **0.558 µm** | **0.672 µm** | **0.866 µm** |
| Real *m* | 1.51 | 1.51 | 1.51 | 1.51 |
| Imaginary *k* | 0.004110 | 0.002100 | 0.000650 | 0.000470 |

Table 13. Complex refractive index for the MISR SA algorithm medium-mode and coarse-mode dust models (#19 and #21).

Analysis of monthly MISR SA retrieval mixtures shows that combinations of model #19 and #21 are primarily chosen in the “dust-belt” arid regions along with Saharan dust outflow areas spanning the Atlantic from western Africa to the Caribbean (Kahn and Gaitley, 2015). However, in order to match the observed radiances to the degree defined by the algorithm acceptance criteria, the two dust models must also be mixed with one or more other models available in the algorithm. These include model #2 (small non-light-absorbing particles with $D_e$ = 0.24 µm), and/or model #6 (large non-absorbing particles with $D_e$= 5.60 µm). Kahn and Gaitley (2015) showed that mixture #57 (36% model #2, 4% model #6 and 60% model #19) is typical for transported dust over ocean, whereas mixture #63 (40% model #2, 48% model #19, and 12% model #21) is typical for dust close to major dust sources. Figure 13 shows the size distribution for the four individual aerosol models (models #2, #6, #19, and #21), as well the two mixtures (#57 and #63). Table 14 lists the effective complex refractive index for the two mixtures.

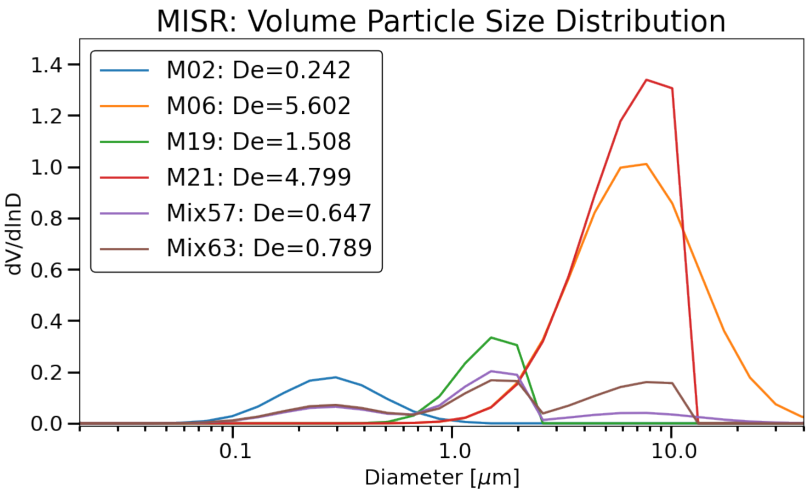

Figure 13. Volume size distributions and effective diameters derived for unit AOD at 558 nm for two MISR dust mixtures (#57 and #63) and their component models (#2, #6, #19, and #21).

| | **Refractive Index** | **Wavelength** | | | |
|---|---|---|---|---|---|
| | | **0.446 µm** | **0.558 µm** | **0.672 µm** | **0.866 µm** |
| **Mixture #57** | Real *m* | 1.4737 | 1.4860 | 1.4918 | 1.4977 |
| | Imaginary *k* | 0.00195 | 0.00126 | 0.00045 | 0.00037 |
| **Mixture #63** | Real *m* | 1.4746 | 1.4860 | 1.4923 | 1.4993 |
| | Imaginary *k* | 0.00193 | 0.00126 | 0.00046 | 0.00039 |

Table 14. Complex refractive index for two MISR dust mixtures (#57 and #63).

#### 4.5.1.1 Application to Research Algorithm

For the MISR research algorithm (RA), either the SA models described above or the MAIAC dust optical model is used, but other models are tested as well (Limbacher et al., 2022). For example, the RA was run for a number of cases near the AERONET site at Cape Verde at times when significant dust plumes were in the field-of-view. Tests to date for different ellipsoid concepts have not worked very well. Validation of MISR RA retrievals with the Cape Verde AERONET observations showed that the medium-mode grain dust model was by far the most successful (Kalashnikova and Kahn, 2006).

## 4.6 Passive Remote Sensing (single angle, UV/VIS)

In the UV wavelengths, atmospheric molecular scattering is strong enough to act as a partially reflective background (or ‘surface’) for monitoring aerosol. Mineral dust, with strong absorptive properties in the UV, can therefore appear dark compared to molecular scattering background, and UV algorithms make use of this property. The history of aerosol remote sensing in the UV starts from the 1970s with analysis of observations from TOMS onboard Nimbus-7 (Dave, 1978). Early sensors were intended to measure ozone, but it was quickly realized that aerosols that interfere with the ozone measurements could also be quantified (Herman et al., 1997).

### 4.6.1 OMAERUV

In addition to TOMS, a UV aerosol algorithm has been applied to observations from OMI onboard Aura (Torres et al., 2013), and from the Tropospheric Monitoring Instrument (TropOMI) onboard Sentinel-5P (Torres et al., 2020). The algorithm makes use of ‘pairs’ of UV wavelengths, such as 340/380 nm (TOMS) or 354/388 nm (OMI), to quantify the absorbing aerosol index (AAI) and then retrieve physical and optical properties of the aerosol. The current algorithm is nominally based on OMI wavelengths (and is referred to as the OMAERUV algorithm), and therefore retrieved aerosol properties are defined at 388 nm.

As the UV observations are sensitive to aerosol absorption, the OMAERUV algorithm dust aerosol model consists of seven sub-models that assume different complex refractive indices, and therefore variable SSAs (see Table 16) that can be chosen during the inversion to best fit the observations (Torres et al., 2007). However, the assumed particle size distribution is the same for the seven sub-models and is characterized by a bimodal volume-weighted lognormal distribution. The size distribution parameters are listed in Table 15, and are based on long-term statistics from AERONET retrievals (Torres et al., 2007).

| **Mode** | **$D_g$ (μm)** | **$\widetilde{D_v}$ (μm)** | **σ** | **$D_{min}$ (μm)** | **$D_{max}$ (μm)** | **$N_0$ (%)** |
|---|---|---|---|---|---|---|
| **Fine**<br>spheroidal -<br>land: Dobovik_25<br>ocean: OMI_25 | 0.104 | 0.24 | ln(1.697) | 0.01254 | 0.86250 | 99.565 |
| **Coarse**<br>spheroidal -<br>land: Dobovik_25<br>ocean: OMI_25 | 1.34 | 3.822 | ln(1.806) | 0.12596 | 14.2524 | 0.0435 |

Table 15. Geometric mean diameter ($D_g$), volume median diameter ($\widetilde{D_v}$), log-size standard deviation (σ), minimum diameter ($D_{min}$), maximum diameter ($D_{max}$), and number weighting fraction for the two modes of the dust aerosol model for OMAERUV.

The shape model for the dust particles is a mixture of randomly oriented spheroids with a fixed distribution of axis ratios. Over land, the axis ratio is the same distribution as Dubovik_25 (Dubovik et al., 2006). However, over ocean, where dust is presumed to have a less-extreme spheroid shape, the model assumes the OMI_25 distribution of axis ratios (Torres et al., 2018) as shown in Figure 6 (red markers).

All these dust models assume that the coarse and fine lognormal modes have the same complex refractive index. The real part of the refractive index is fixed at $m = 1.55$, whereas the imaginary part ($k$) varies by sub-model and by wavelength (Table 16). Analysis of the long-term OMAERUV dataset in dust-dominated areas shows that the majority of retrieved 388 nm SSA values for dust fall within the range of 0.85-0.95 (Jethva et al., 2014), which is covered by sub-models 3-5. For these three sub-models, the Absorption Ångström Exponent (AAE) (Moosmüller and Chakrabarty, 2011), which describes the absorption part of the spectral dependence of the SSA between 354 and 388 nm, takes on the value of AAE = 2.02, 2.27 and 2.73, respectively.

| **Model #** | **Complex Refractive Index and Single Scattering Albedo** | | | | | | |
|---|---|---|---|---|---|---|---|
| | **All Channels** | **354 nm** | | **388 nm** | | **500 nm** | |
| | $m$ | $k$ | $\omega$ | $k$ | $\omega$ | **k** | $\omega$ |
| 1 | 1.55 | 0.02303 | 0.74982 | 0.01662 | 0.77921 | 0.00720 | 0.86268 |
| 2 | 1.55 | 0.01279 | 0.80740 | 0.00923 | 0.83778 | 0.00400 | 0.91046 |
| 3 (M1) | 1.55 | 0.00832 | 0.84727 | 0.00600 | 0.87606 | 0.00260 | 0.93640 |
| 4 (M2) | 1.55 | 0.00561 | 0.88062 | 0.00405 | 0.90532 | 0.00176 | 0.95430 |
| 5 (M3) | 1.55 | 0.00256 | 0.93213 | 0.00185 | 0.94886 | 0.00080 | 0.97805 |
| 6 | 1.55 | 0.00128 | 0.96221 | 0.00092 | 0.97234 | 0.00040 | 0.98620 |
| 7 | 1.55 | 0.00000 | 1.00000 | 0.00000 | 1.00000 | 0.00000 | 1.00000 |

Table 16. Complex refractive index of mineral dust aerosol sub-models assumed in the operational aerosol algorithms of the UV-based sensors (TOMS, OMI, TropOMI). Note that for plotting purposes, the more common dust sub-types (3, 4 and 5) are renamed in this paper as M1, M2, and M3, respectively.

Figure 14 shows the size distribution and optical properties for the most common dust sub-types (3, 4, and 5) that are renamed here as M1, M2, and M3, respectively. In Figure 14a, we show the volume size distribution for the land (Dubovik_25) and ocean (OMI_25) shape models. A recent paper from Saito and Yang (2022) provides a generalized framework for comparing size distributions for particles of arbitrary shape. Notably, the choice of spheroid shape distribution leads to discernible differences in volume size distribution, likewise in scattering properties ($P_{11}$ and DoLP), and lidar properties. Figure 14b-c shows the range of spectral AOD and SSA values for the three sub-models assuming the land (Dubovik_25) shape model. There is no discernable difference in spectral AOD for the three sub-models as the real part of the refractive index is fixed for all sub-models.

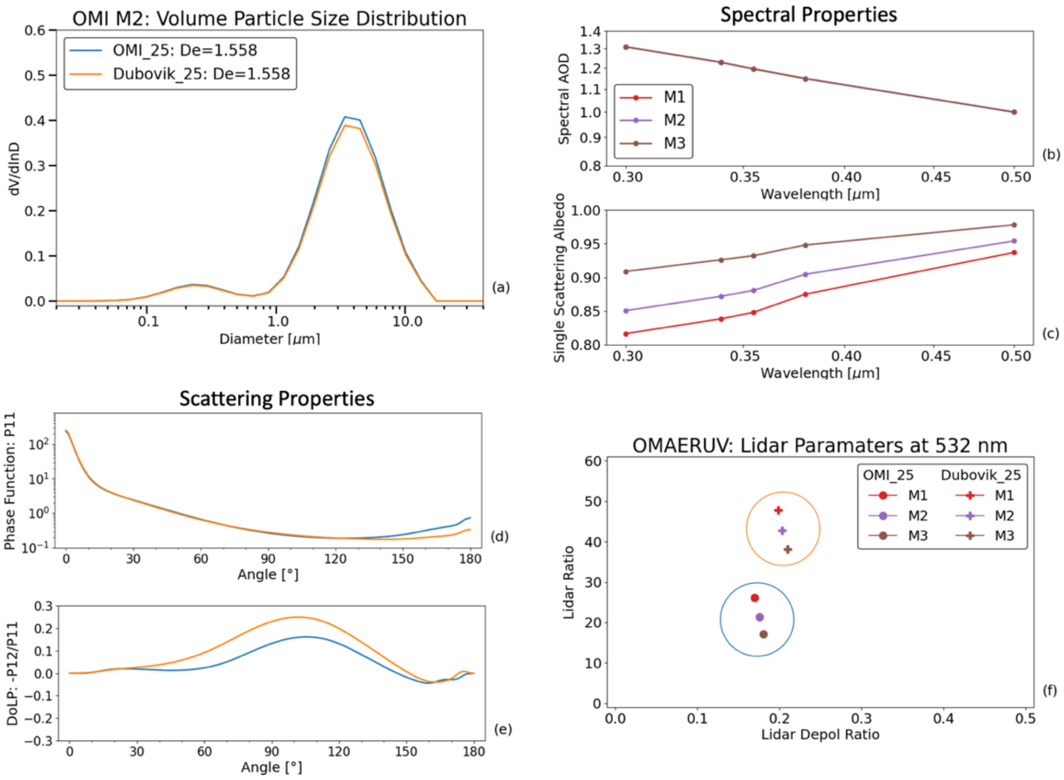

Figure 14. Volume Size distribution, scattering, spectral, and lidar properties for the OMAERUV dust model, derived for unit AOD at 500 nm. The size distribution and scattering properties (panels a, d, and e) are for sub-model M2, and illustrate the differences that arise from the two different shape models implemented over land (Dubovik_25) and ocean (OMI_25). The spectral

lidar properties in panels (b) and (c) were calculated with the land (Dubovik_25) shape model to illustrate differences in AOD and SSA that relate to the selection of the different sub-models. Panel (f) illustrates how differences in shape models and sub-models lead to different lidar properties.

### 4.7 Active Remote Sensing (Lidar)

Lidar methods for the observation of dust (Sugimoto and Huang, 2014), such as backscatter lidar (BL) and high spectral resolution lidar (HSRL), provide measurements of total attenuated backscatter and linear depolarization ratio ($\delta_L$) vertical profiles (BL), and retrievals of aerosol backscatter and extinction vertical profiles (HSRL), often at multiple wavelengths. Although backscatter lidar retrievals require assumptions about the aerosol lidar ratios (S) (Young and Vaughan, 2009), HSRL instruments with high signal-to-noise ratios can directly retrieve aerosol extinction coefficient ($\beta_{ext}$) profiles without any assumptions about aerosol scattering properties (Hair et al., 2008). However, even for the simpler backscatter lidars, observed parameters such as $\delta_L$ and backscatter color ratio (the ratio of attenuated backscatter at two wavelengths, typically 1064 and 532 nm) can be used to identify vertical layers that contain dust versus other particle types (Kim et al., 2018). This aids in assigning an appropriate lidar ratio to these aerosol features in backscatter lidar vertical profile observations, thereby aiding in retrieval of aerosol properties.

Although no successful HSRL instruments have been flown in space to date, ground-based and aircraft HSRL instruments have provided regional measurements (e.g., Burton et al., 2012). Only backscatter lidars have provided space-borne measurements, two of which are the Cloud-Aerosol Lidar with Orthogonal Polarization (CALIOP) operating onboard Cloud-Aerosol Lidar and Infrared Pathfinder Satellite Observation (CALIPSO) and the Cloud-Aerosol Transport System

(CATS) lidar that operated for 33 months on the International Space Station (ISS) (Winker et al., 2009; Yorks et al., 2016).

#### 4.7.1 Dust Identification and Lidar Ratio Assumptions for Backscatter Lidars CATS and CALIOP

Layer features in the lidar vertical profile measurements are identified as clouds or aerosol using observed quantities such as the total attenuated backscattered intensity and $\delta_L$. The latter is an intensive property (i.e., does not scale with aerosol load) that provides information on particle shape. Generally, non-spherical particles such as dust and ice exhibit $\delta_L > 0.0$, whereas for spherical particles $\delta_L = 0.0$. Ice crystals are typically more non-spherical than dust and exhibit higher values of $\delta_L$. Thus, dust layers are differentiated from other aerosols and ice in the lidar vertical profiles in part by imposing appropriate upper and lower bounds on $\delta_L$, and in part by external considerations such as surface type (Kim et al., 2018). The vertical distribution of backscatter is also used to help distinguish cirrus from dust in the CALIOP algorithm. However, as backscatter lidars measure the total (also referred to as volume) $\delta_L$, it includes contributions from both particle and molecular backscatter. For CALIOP, which measures $\delta_L$ at 532 nm, the molecular contribution can be significant, and $\delta_L$ must be corrected for molecular linear depolarization. The molecular linear depolarization ratio can be computed from theory, and this is used to estimate the particle linear depolarization ratio ($\delta_L^p$) (Omar et al., 2009). In the CALIOP retrieval algorithm, dust identification is done with the estimated $\delta_L^p$. For CATS, which measures $\delta_L$ at 1064 nm, the molecular contribution is assumed to be marginal, and dust identification is done with the measured $\delta_L$.

The CATS and CALIOP retrieval algorithms implement various thresholds for $\delta_L$, not just to nominally identify pure dust, but also mixtures of dust with other aerosols. This is to provide better fidelity in the estimate of the layer lidar ratio. $\delta_L$ thresholds for pure dust and commonly observed dust mixtures were determined empirically and are shown in Table 17. The "Dust Mixture" and "Dusty Marine" thresholds assumed by the CATS and CALIOP retrieval algorithms, respectively, attempt to identify aerosol layers that are mixtures of dust and marine aerosol. CALIOP also considers an additional "Polluted Dust" mixture that is used to identify aerosol layers that may be a mixture of dust and smoke or polluted continental aerosol. As non-dust aerosol types are typically spherical, the depolarization ratio thresholds for dust mixtures are lower than for pure dust.

| Instrument | Aerosol type | Depolarization Ratio | Wavelength |
|---|---|---|---|
| CALIOP V4 | Desert Dust | $0.20 < \delta_L^p$ | 532 nm |
| | Polluted Dust | $0.075 < \delta_L^p \leq 0.20$ | 532 nm |
| | Dusty Marine | $0.075 < \delta_L^p \leq 0.20$<br>over ocean, layer base < 2.5 km | 532 nm |
| CATS V3 | Dust | $0.25 < \delta_L$ | 1064 nm |
| | Dust Mixture | $0.15 < \delta_L \leq 0.25$ | 1064 nm |

Table 17. Depolarization ratio criteria for assigning dust and dust mixture types for CALIOP and CATS.

Once an aerosol layer is determined to contain dust or a dust mixture, a corresponding layer-average lidar ratio is assigned and used to calculate the aerosol backscatter and extinction coefficients. Table 18 shows the lidar ratio values for dust and dust mixtures assumed in the CALIOP and CATS retrieval algorithms (Kim et al., 2018; Yorks et al., 2016). The assumed lidar ratio values are based on measurements from two main sources: (1) ground-based observations from EARLINET (European Aerosol Research Lidar Network) (Matthias et al., 2004) and AERONET, and (2) techniques to directly estimate the AOD and layer-average lidar ratio from CALIOP and CATS observations. These techniques include constraining the AOD for aerosol layers that are located above opaque water clouds (Hu, 2007) or the Synergized Optical Depth of Aerosols (SODA) method that uses a combination of CALIOP and radar measurements of the ocean surface reflectance to derive AOD (Josset et al., 2011, 2008).

Table 19 shows the various measurements of dust lidar ratios used to determine the operational CATS Version 3 and CALIOP Version 4lidar ratio assumptions for pure dust. The lidar ratio values assumed for CATS and CALIOP "Dust Mixture" and "Dusty Marine" retrievals, respectively, are lower than the assumptions for pure dust because the 532 nm lidar ratio of marine aerosol is estimated to be 23 sr (Kim et al., 2018). For the CALIOP "Polluted Dust" mixture, the 532 nm lidar ratio is higher than the assumed pure dust lidar ratio, as the lidar ratio of smoke and polluted continental aerosols is estimated to be ~70 sr (Omar et al., 2009).

| Instrument | Aerosol type | $S_{532}$ (sr) | $S_{1064}$ (sr) |
|---|---|---|---|
| CALIOP V4 | Desert Dust | 44 ± 9 | 44 ± 13 |
| | Polluted Dust | 55 ± 22 | 48 ± 24 |
| | Dusty Marine | 37±15 | 37±15 |
| CATS V3 | Dust | 45 | 40 |
| | Dust Mixture | 35 | 40 |

Table 18. Lidar ratios assumed by CALIOP and CATS for dust and dust mixtures.

| Wavelength | Lidar Ratio (sr) | Location | Reference |
|---|---|---|---|
| 532 nm | 43.9 ± 9.3 | Saharan dust | Hu et al., (2007) |
| | 44.4 ± 8.8 | Saharan dust | Liu et al., (2015) |

| | | | |
|---|---|---|---|
| | 49.7 | African Sahel | Schuster et al., (2012) |
| | 42.6 | Middle East | |
| | 43.8 | Kanpur, India | |
| | 53 ± 6 | Saharan dust | Nisantzi et al., (2015) |
| | 41 ± 4 | Middle East | |
| | 45 ± 3 | Granada | Papagiannopoulos et al., (2016) |
| 1064 nm | 56 ±16 | Saharan dust | Omar et al., (2010) |
| | 50 | Saharan dust | Liu et al., (2011) |
| | 41 | Saharan dust | Vaughan et al., (2015) |
| | 40 ± 20 | Saharan dust | Pauly et al., (2017) |

Table 19. Observations of lidar ratios used to determine the assumed CALIOP V4 and CATS V3 lidar ratios for dust.

### 4.8 Comparison of Remote Sensing Dust Model Optical Properties

In the previous subsections, we have described a variety of dust models assumed or retrieved for different combinations of algorithms and sensors. Here, we examine a subset of 11 dust models listed in Table 20 and summarize key similarities and differences in physical and optical property assumptions between the different algorithms.

For comparison purposes, we use the DSL scattering code (Dubovik et al., 2006) to calculate dust optical property values for the various dust models. The DSL package contains precomputed tables (also referred to as “kernels”) of dust single scattering properties for discrete combinations of size parameter, complex refractive index, and spheroidal axis ratio. These tables facilitate fast calculation of dust optical properties as they can be easily interpolated to a desired set of microphysical properties. However, it can only be applied to dust models that assume spheroidal dust shape models. In this comparison, only the MISR retrievals use a non-spheroid, grain, or ellipsoid shape model. Thus, for this retrieval we report optical properties that were provided to the authors by the algorithm developers.

Optical property results shown in the following for each algorithm include spectral extinction, single scattering albedo $\omega$, lidar ratio $S$, lidar linear depolarization ratio $\delta_L$, phase function $P_{11}$, and degree of linear polarization $(-P_{12}/P_{11})$. Where our DSL-based computations are significantly different from what is used within the given algorithm, we report optical property values supplied by the algorithm teams. The most common reason for such differences in optical property outputs is due to truncation of size distribution.

| **Label** | **Algorithm** | **Shape Assumptions** | **Size Distribution assumptions (# of Modes)** | **Defining wavelength (µm)** | **Notes** |
|---|---|---|---|---|---|
| Cape Verde: Orig Size | AERONET | Dubovik_25 | No constraint | 0.440 | d |
| DT-L: Dust | Dark Target Land | Dubovik_11 | Lognormal (2) | 0.554 | a, c |
| DT-O: F4MixC6_FMF0p30 | Dark Target Ocean | Spheres | Lognormal (2) | 0.554 | c, e |
| DT-O: M10 | Dark Target Ocean | Dubovik_25 | Lognormal (1) | 0.554 | c, e |
| SOAR: Dust_FMF0p15 | SOAR | Dubovik_25 | Lognormal (2) | 0.551 | e |
| DB-L: Dust_FMF0p15 | Deep Blue | Spheres, Dubovik_25 | Lognormal (2) | 0.551 | e, f |
| MAIAC: Dust | MAIAC | Dubovik_25 | Lognormal (2) | 0.466 | a |
| MISR: Mix57 | MISR Standard Algorithm | Spheres, Grains | Lognormal (3) | 0.558 | b, c, e |
| MISR: Mix63 | MISR Standard Algorithm | Spheres, Grains, Spheroids | Lognormal (3) | 0.558 | b, c, e |
| OMI: M1 | OMAERUV | OMI_25 | Lognormal (2) | 0.500 | e |
| OMI: M3 | OMAERUV | OMI_25 | Lognormal (2) | 0.500 | e |
| Notes:<br>a: Dynamic models (function of AOD). Plotted for AOD=1.0 at index wavelength. | | | | | |

b: Truncated size distributions used for grains (aggregates of cubes) and spheroids as input to DDA.
c: Models are mixed with others during retrieval.
d: This model represents a retrieved mixture
e: This model represents a “characteristic” retrieval
f: Choice of imaginary refractive indices: 0.00304 @ 0.41 mm, 0.00195 @ 0.48 mm and 0.00161 @ 0.67 mm.

Table 20. List of 11 dust models compared in this section, including shape assumptions, size assumptions (with number of modes for the distribution), and additional notes.

Figure 15 shows a comparison of the particle size distribution and volume effective diameter for the 11 dust models. Nearly all models have a dominant coarse mode centered around approximately 2.5-3.5 µm diameter and a smaller fine mode centered at 0.2-0.3 µm diameter. However, the MISR and AERONET dust models are notable exceptions, showing three distinct modes. The median diameter of the coarse mode of the MISR dust models centered at 8-9 µm diameter is also significantly larger than the rest of the models, but the medium and fine modes also have significant weighting. Thus, the effective diameters shown in Figure 15 for the MISR models are roughly four times smaller than those of the other dust models.

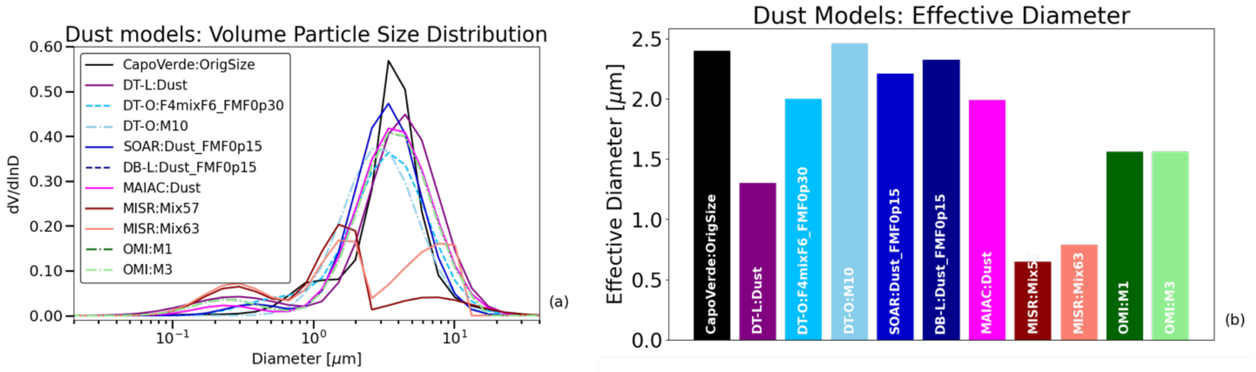

Figure 15. Comparison of (a) particle size distribution and (b) effective diameters of volume for the 11 dust models list in Table 20.

Figure 16 shows a comparison of the complex refractive index, spectral AOD, and single scattering albedo for the 11 dust models. Most values for the real refractive index fall within the range of 1.55 and 1.45, but the DT-O dust model that is a mixture of F4 and C6 sub-models is an outlier with a real refractive index value of 1.35. Most models assume little or no spectral dependence in the real refractive index, which departs from the AERONET retrieval at Cape Verde where the real refractive index decreases with wavelength. There is less diversity among the dust models for the imaginary refractive index with all falling within the range of the two OMI dust models that span the range of absorption retrieved for dust. Compared to what is reported for in situ measurements of bulk dust (Figure 5) and what is assumed by Earth system models (see Section 5, Figure 21), remote sensing dust models have little or no spectral dependence in the imaginary refractive index beyond 0.7 μm. This may be because the remote sensing algorithms make little or no use of these longer wavelengths in their retrievals, and thus make a simple choice that has no effect on the retrieval results. The variability in the spectral single scattering albedo closely matches the variability in the imaginary refractive index. Most of the models also have similar weak AOD spectral dependence, except for the MISR and OMI dust models that have stronger AOD spectral dependence (i.e., larger Ångström exponent). This is because these dust models have a larger contribution from medium and fine modes in the particle size distribution.

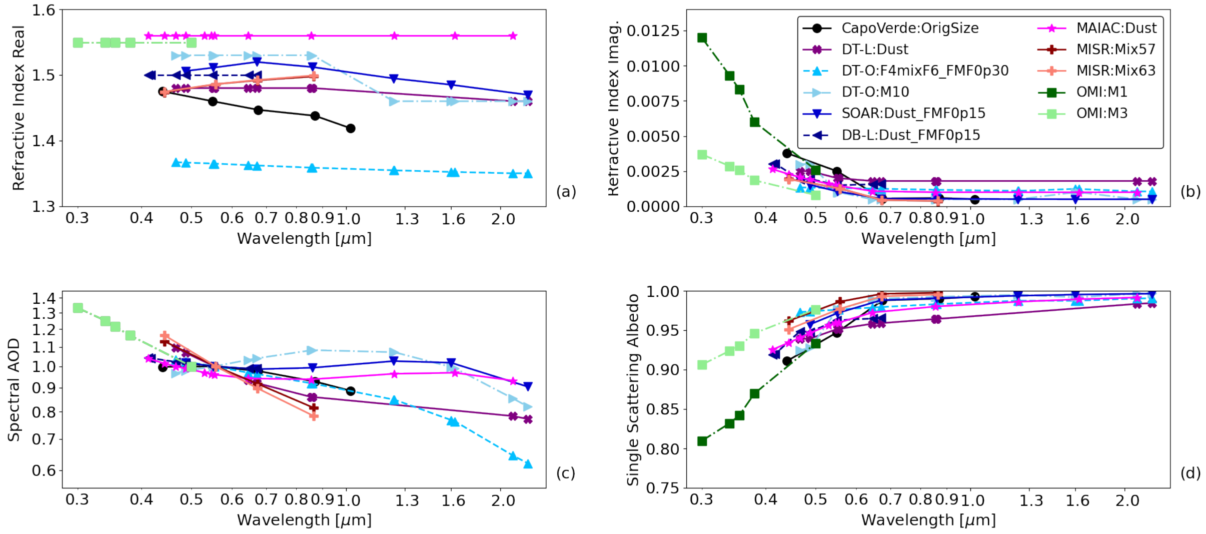

Figure 16. Comparison of the real refractive index (a), imaginary refractive index (b), spectral AOD (c), and single scattering albedo (d) for the 11 dust models list in Table 20.

Scattering properties for the 11 dust models are shown in Figure 17. At side scattering angles, the models that assume non-spherical particles have similar phase-function angular dependence. The spherical DT-O dust model is an outlier. However, the degree of linear polarization function shows significant variability in angular dependence among the dust models.

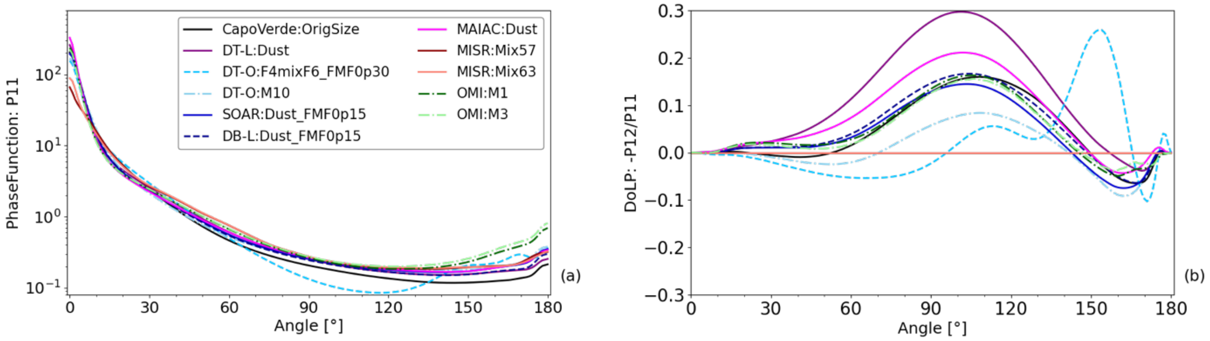

Figure 17. Scattering properties of the retrieval dust models defined at unit optical depth for index wavelength described in Table 20. Panels are (a) Normalized phase function (P11) and (b) DoLP (-P12/P11) defined at index wavelength and as function of the scattering angle.

At near backscattering angles there is significant divergence in the phase functions, which is apparent in the large variability in spectral lidar ratios among the dust models shown in Figure 18a. At 500 nm the range in lidar ratios from the various models is approximately 18-65. The OMI dust models, which here assume the ocean shape model, have the lowest lidar ratio values of all. The OMI lidar ratios are between 18-25, which is more indicative of marine aerosol (sea salt) than marine dust. However, the OMI over land shape model has lidar ratios in the range of 35-45 (see Figure 14 in the OMAERUV section). The AERONET Cape Verde retrieval and the DT-Land model have the highest lidar ratios equal to 62 and 55, respectively. These values are in the range of the CALIOP thresholds for polluted dust. The lidar ratios for the other models fall within the range of 38-42, within the range of measurements of pure dust (Table 19).

Notably, all the dust models (except for the spherical DT-O model) have lidar depolarization ratios above the CALIOP and CATS thresholds for pure 'Dust' detection (Figure 18b). The values at 500 nm range from 0.2-0.3, which agrees well with the range observed by laboratory measurements (Järvinen et al., 2016). The OMI over ocean dust models have the lowest depolarization values of the non-spherical dust models as their axis ratio spheroid distribution has a higher weighting for axis ratios equal to 1 (i.e., spherical particles) than the other dust models.

The two-dimensional projection of lidar ratio and depolarization ratio at 532 nm is shown in Figure 18c. Burton et al. (2012) created a similar figure from HSRL measurements taken during various field campaigns (see their Figure 12). The HSRL observations indicate that the “dusty mix” depolarization ratios lie in the range of 0.1-0.2, whereas “pure dust” depolarization ratios are greater than 0.3. Because of this, the distribution of lidar and depolarization ratios for the 11 dust models falls in between the HSRL observations that were classified as “dusty mix” and “pure dust”, and rather overlaps with the observations that are classified as “ice”. It is notable that both Järvinen et al. (2016) and Miffre et al. (2016) both measured individual dust samples in the laboratory with depolarization ratios > 0.3, however the bulk of the 201 samples analyzed by Järvinen et al. (2016) had depolarization ratios between ~0.12 and 0.28, while the Miffre et al. (2016) measurements were only for two dust samples. These discrepancies, and the large variability in the linear polarization function, highlight the difficulty that remote sensing algorithms face in fully representing the scattering properties of dust that will be required for future combined multi-instrument retrievals of both active and passive sensors, including observations of polarization.

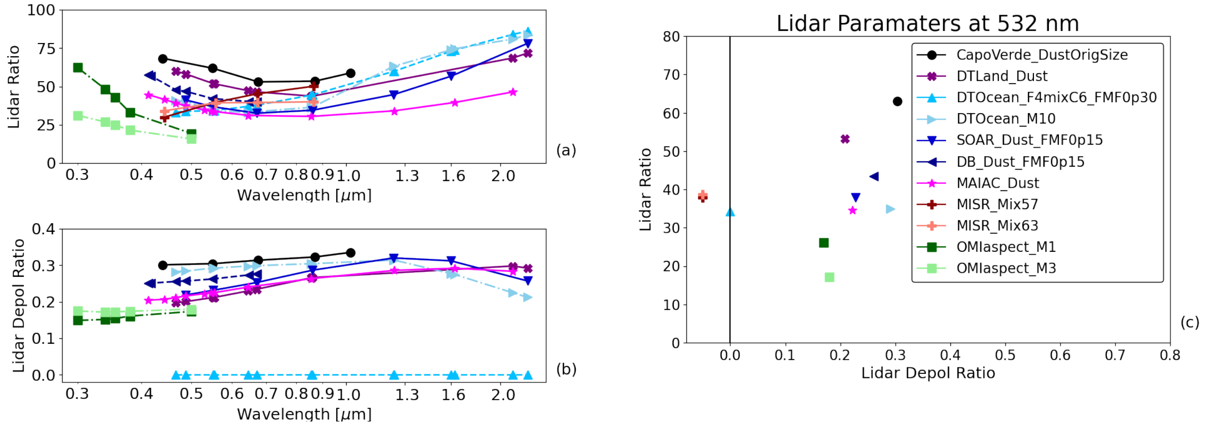

Figure 18. Lidar properties of the retrieval dust models defined at unit optical depth for index wavelength described in Table 20. Panels are (a) lidar ratio and (b) lidar depolarization ratios as function of wavelength, and (c) lidar parameters from (a) and (b) interpolated to 532 nm. Note

that no DoLP or lidar depolarization ratio is calculated for MISR models so they are not shown in (b) and are placed to the left of the 0.0 line in (c).

Finally, we took the dust density assumptions implemented by various global Earth system models (nominally 2500 kg m$^{-3}$, see Table 21) and converted the remote sensing retrieval aerosol extinction at 550 nm to aerosol mass extinction efficiency (MEE) shown in Figure 19. The MEE is the key parameter that facilitates comparisons of simulations of aerosol mass loading by atmospheric circulation models to remote sensing retrievals of AOD. Nearly all models converge to a value of roughly 0.6 m$^2$g$^{-1}$. However, the MISR models are outliers with higher MEEs of 1.26 and 0.96 m$^2$ g$^{-1}$ reflecting the more dominant fine and medium modes in the size distribution as compared to the other remote sensing dust models. This analysis shows that the MEE is sensitive to the underlying aerosol model assumptions implemented in remote sensing retrievals, and highlights the uncertainty and limitations of AOD retrievals for constraining simulations of atmospheric composition.

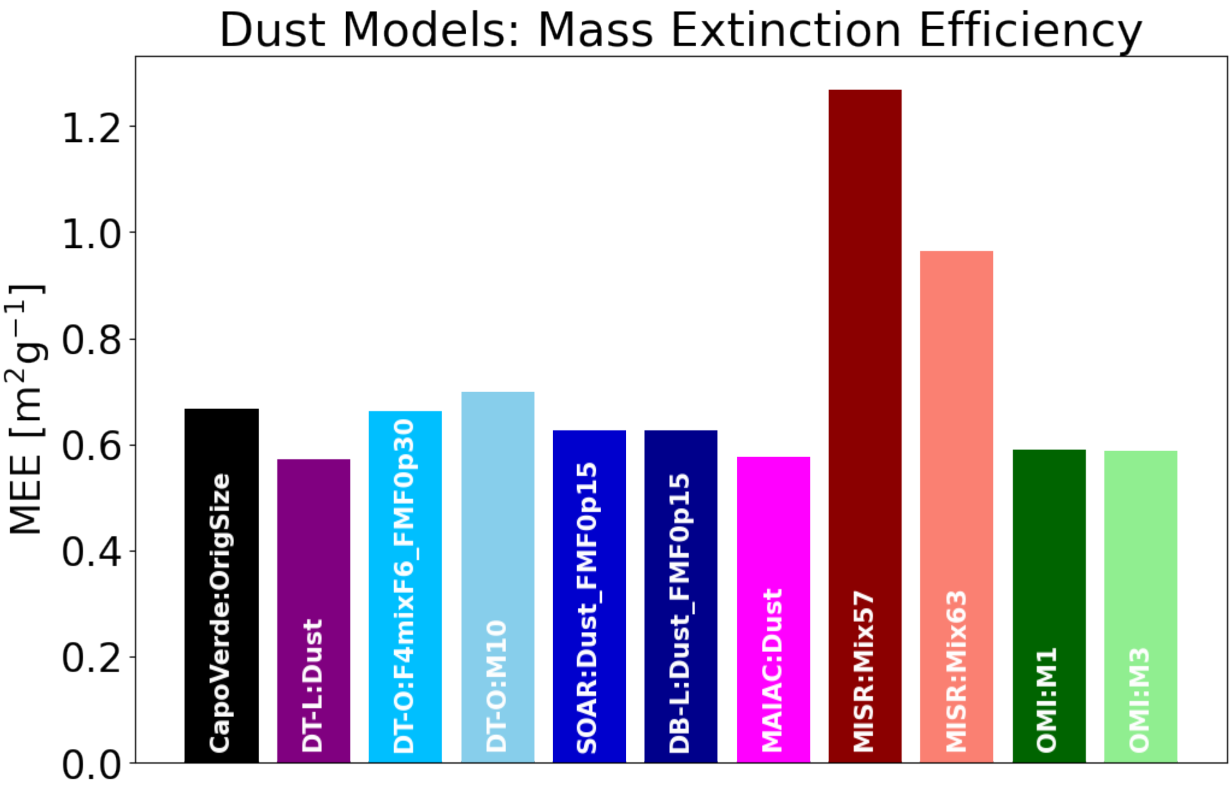

Figure 19. The 550 nm mass extinction efficiency (MEE) in $m^2$ $g^{-1}$ for the 11 remote sensing dust models assuming a dust particle density of 2500 kg $m^{-3}$; the nominal value assumed by most global earth system models. Note that the OMI MEE is calculated at 500 nm.

## 5 Representation of Dust in Earth System Models

The significant impacts of dust aerosols on the Earth system have driven their inclusion in a variety of atmospheric modeling frameworks since at least the 1980s (Schütz, 1980; Westphal et al., 1988, 1987). We focus the discussion here on the implementation of dust in global Earth system models (ESMs) and chemistry transport models (CTMs), with the distinction drawn between these two classes of models having to do with the presence of Earth system couplings (i.e., radiative or cloud feedbacks) in ESMs versus treatment of dust as a passive tracer species transported by prescribed winds as in CTMs. Early work on the inclusion of non-interactive dust species in global climate models and CTMs was presented in Joussaume (1990), Genthon (1992), Tegen and Fung (1994), Tegen and Lacis (1996), Mahowald et al. (1999), and Ginoux et al. (2001), and radiatively interactive dust in global ESMs in the work by Tegen and Miller (1998) and Woodward (2001). Dust is now a standard component in a number of CTMs and ESMs, with relatively recent multi-model evaluations reported in Huneeus et al. (2011), Kim et al. (2019, 2014), Checa-Garcia et al., (2021), and Zhao et al., (2022). Increasingly, dust has become a component of global, near-real time weather and aerosol forecasting systems (Benedetti et al., 2018; Xian et al., 2019).

In this section, we report on the current representation of dust properties in global aerosol models that have contributed to recent intercomparison efforts, drawing especially from those models that have contributed to the AeroCom project (Kinne et al., 2006; Schulz et al., 2006; Textor et al., 2006; and later) as well as the growing community of models contributing to the International Cooperative for Aerosol Prediction (ICAP) multi-model ensemble of operational/near-real time global aerosol forecasting systems (Xian et al., 2019). This cohort of models is generally representative of models contributing to the Climate Model Intercomparison Project (CMIP) that feeds into the Intergovernmental Panel on Climate Change (IPCC) reports. We do not discuss specifically the inclusion of dust in regional or limited area models here, although in general the treatment of dust physical and optical properties in such models is similar to what is presented here for global ESMs and CTMs (e.g., a version of the aerosol module in the NASA/GEOS model discussed below is an aerosol component in WRF-Chem).

We begin with a brief description of the processes affecting the dust lifecycle in models, followed by a description of approaches to representing dust aerosols in models, a survey of specific implementations of dust model parameters, including their microphysical and radiative properties, and an analysis of their sensitivity to underlying assumptions.

## 5.1 Dust Processes in ESMs and CTMs

Like other aerosol and gas species carried in models, a variety of source, sink, and transport processes determine the dust lifecycle. A detailed review of the implementation of these processes in models is beyond the scope of this paper, but we briefly cover here some aspects of these processes as they relate to the evolution of dust microphysical and optical properties during a simulation.

### 5.1.1 Dust Emission

The mechanisms for mobilization of dust particles small enough to remain suspended in the atmosphere ($D < \sim 20$ μm) are saltation and sand blasting (Gillette, 1974; Gillette et al., 1974; Gillies, 2013; Shao, 2001; Shao and Raupach, 1993). The details of these processes are complex and in principle require a comprehensive representation of the surface soil particle size distribution and composition, the distribution of surface roughness elements that impede emission processes, and so on (e.g., Klose et al., 2021; Kok et al., 2014; Marticorena and Bergametti, 1995; Shao, 2001). Often a pragmatic approach is taken in which the complicated physics of the mobilization process is reduced to calculating a dust vertical flux into the atmosphere that is scaled to some power of the near-surface wind speed in excess of a threshold that accounts for the physical barriers to mobilization (e.g., Ginoux et al., 2001). The precise form of this equation varies across models but is in general inspired by wind-tunnel and surface observations that have simultaneously characterized dust mobilization fluxes and wind speeds (e.g., Gillette and Passi, 1988). Because there are no global observations of the dust emission flux magnitude and because the scales in global models are much larger than the sub-grid scales of the emission processes, there is usually an *a posteriori* tuning coefficient applied to the emission flux equation that scales the total emissions so that the model reproduces some desired observable quantity, such as the AOD or deposition fluxes (Cakmur et al., 2006).

Once calculated, the total dust emission flux needs to be apportioned across the particle size distribution. In principle, the emitted particle size distribution is also a function of the surface and soil characteristics and varies with wind speed, which determines the kinetic energy that saltating particles impart when fragmenting aggregates (Alfaro et al., 1998; Grini et al., 2002). In practice, it is common in models for the emitted dust particle size distribution to have either only a weak dependence on wind speed (Ginoux et al., 2001), be constrained by downwind observations (Cakmur et al., 2006), or else be prescribed (Klose et al., 2021; Kok, 2011; Yaping Shao et al., 2011). The analysis in Kok et al. (2017) and Adebiyi and Kok (2020) showed that the emitted dust size distribution assumed by many models is much finer than measurements indicate, contributing to the consistent underestimation of larger particles in the atmosphere (as discussed in Section 2), causing a negative bias of dust DRE for a given global aerosol mass.

### 5.1.2 Dust Loss Processes

Dust loss processes in global models are also size dependent. Most models account for losses of aerosol through dry and wet processes. Commonly, dust loss by dry deposition is represented in a simple way with the size-dependent Stokes settling velocity applied to compute downward dust transport in the column (e.g., Ginoux et al., 2001). Dust particles are also removed by aerodynamic dry deposition near the surface, but the magnitude of this process is generally much smaller than that of the loss via gravitational settling except for particles with diameter less than 1 μm. Notably, models typically assume a spherical particle shape when calculating their settling speeds. Attempts to account for particle non-sphericity, which decreases the particle settling speeds, only partially address the underrepresentation of large dust particles in models (e.g., Colarco et al., 2003; Ginoux, 2003; Huang et al., 2020). Other possible mechanisms that may decrease dust particle losses, such as representing particle electrification and fine scale, unresolved turbulence in dust layer are not presently included in models, and so the ability of models to properly maintain the observed dust particle size distribution over long-range transport remains an outstanding issue.

In addition to its removal by dry processes, dust is also removed in the atmosphere by scavenging in cloud droplets and precipitation, as well as incorporation into ice crystals. For models that do not explicitly deal with aerosol-cloud interactions, the loss of dust by wet processes is parameterized. For in-cloud and below-cloud large-scale wet removal processes, in-cloud precipitation conversion rates and precipitation fluxes are used to parameterize dust removal, and for convective removal the convective updraft mass flux is used (e.g., Liu et al., 2001). Such wet removal schemes are not necessarily size-dependent like dry deposition, although there are approaches that account for size-dependent collection efficiencies which could explicitly alter the size distribution (e.g., Croft et al., 2010; Zender et al., 2003). Development of aerosol-cloud interactions in models (e.g., Barahona et al., 2014) could also resolve size-dependent dust wet-removal processes.

### 5.2 Representation of Dust in Global Models

Given the large computational expense of tracer transport, most global models, particularly those deployed for operational or near-real time forecasting, cannot represent dust properties with the same level of complexity that is implied by observations. Simplifications must be made with respect to the fidelity of the representation of composition, size, and morphology of the particles.

In the following, we discuss the common approaches to representing dust composition and size in global models.

### 5.2.1 Dust Composition

Dust mineral composition is fundamental to its climate impact. Despite known regional variations in the mineral composition of sources (Carlson and Prospero, 1972; Claquin et al., 1999; Journet et al., 2014), models typically assume a globally uniform mineral composition. However, there are on-going developments to represent variations in aerosol mineral content through dust emission schemes that depend on maps of soil mineral composition (Li et al., 2021; Pérez Pérez García-Pando et al., 2016; Perlwitz et al., 2015a, 2015b; Scanza et al., 2015). This complexity comes with the added computational expense of carrying several additional tracers, as well as uncertainties in the transformation of the soil mineral fractions into those of lofted dust particles and in the global maps of soil mineral content that are extrapolated from a limited number of local measurements (Claquin et al., 1999; Journet et al., 2014; Nickovic et al., 2012). The latter uncertainty is being addressed by NASA's Earth Mineral Dust Source Investigation (EMIT), which has placed a hyperspectral imaging spectrometer aboard the International Space Station to provide global retrievals of soil minerals whose spectral absorption features lie between the UV and near-infrared (0.38 – 2.5 μm) with unprecedented spatial detail (Green and Thompson, 2020). However, a remaining challenge for constraining models of dust composition is the dearth of atmospheric measurements of aerosol mineral concentration, especially for climatically significant minerals like hematite and goethite that are present only in trace amounts (e.g., Perlwitz et al., 2015b).

Notably, the models surveyed for this paper treat dust as a constituent that is distinct from other aerosol species, which together form an external mixture. However, some more complex models represent mixtures between dust and other species either in a core-shell configuration representing coagulation or chemical reactions on the dust particle surface that form coatings of sulfates and nitrates, or else otherwise internally mix the dust particles with other aerosol components (e.g., Bauer et al., 2008; Bauer and Koch, 2005).

### 5.2.2 Dust Size Distribution

Dust size is generally represented through two approaches in ESMs and CTMs that have implications for the algorithms for dust emission and loss processes and therefore the dust optical properties. The models we surveyed for this paper adopt a "sectional" approach, in which the dust particle size distribution is discretized into a series of size bins that each represent some fractional part of the overall total dust particle size distribution. These size bins, as implemented in the models surveyed here, are non-interacting in the sense that there is no transfer of mass from one size bin to another such as through collision and coagulation. For each bin, the mass input due to emissions is determined as discussed in Section 5.1.1 and for each there are (possibly) size-dependent loss rates determined as in Section 5.1.2. The number of size bins and the range of particle diameters spanned varies from model to model and is chosen to balance the operational needs of the model to achieve a desired accuracy in representing the size distribution on one hand and efficiency in terms of the computational cost of running the model on the other.

An alternative approach to describing the dust particle size distribution is with a modal or moments scheme, in which the evolution of the dust particle size is simulated by parameterizations that track some moment of the particle size distribution, such as for example the modal diameter, usually described by a lognormal mode. Modal and moment approaches typically mix dust internally with other aerosol species (e.g., Bauer et al., 2008; Liu et al., 2012). Internal mixing complicates the separation of the dust optical properties from those of other species. We do not consider these approaches further in this survey, and instead focus on sectional schemes that externally mix dust with other aerosol species. It should be noted that additionally there are sectional approaches that also represent internally mixed particles (e.g., Yu et al., 2015).

### 5.3 Survey of Dust Models

Table 21 summarizes the ten models surveyed in this paper: NASA/GEOS, NOAA GFDL/AM4, NOAA/GEFS, NASA GISS/ModelE2.1, ECMWF/IFS, FMI/SILAM, BSC/MONARCH, JMA-MRI/MASINGAR, UKMO/UM, and NRL/NAAPS. We note that the aerosol formulation in NOAA/GEFS is identical to NASA/GEOS. Eight of these models are core contributors to the ICAP multi-model ensemble discussed in Xian et al. (2019): GEOS, IFS, SILAM, MONARCH, MASINGAR, NAAPS, UM, and GEFS. ModelE and AM4 are frequent contributors to the AeroCom intercomparison and feed into CMIP studies. GEOS is also a frequent contributor to the AeroCom effort. We direct the interested reader to Table 1 in Kim et al. (2014) and Table 1 of Huneeus et al. (2011) for additional models contributing to AeroCom.

| | GEOS/GEFS | AM4 | ModelE | IFS | SILAM | MONARCH | MASINGAR | UM | NAAPS |
|---|---|---|---|---|---|---|---|---|---|
| # size bins[†] | 8 | 8 | 8 | 3 | 4 | 8 | 10 | 2 | 1 |
| Diameter Ranges [μm] | 0.2-0.36,<br>0.36-0.6,<br>0.6-1.2,<br>1.2-2,<br>2-3.6,<br>3.6-6,<br>6-12,<br>12-20 | 0.2-0.36,<br>0.36-0.6,<br>0.6-1.2,<br>1.2-2,<br>2-3.6,<br>3.6-6,<br>6-12,<br>12-20 | 0.2-0.36,<br>0.36-0.6,<br>0.6-1.2,<br>1.2-2,<br>2-4,<br>4-8,<br>8-16,<br>16-32 | 0.06-1.1,<br>1.1-1.8,<br>1.8-40 | 0.01-1,<br>1-2.5,<br>2.5-10,<br>10-30 | 0.2-0.36,<br>0.36-0.6,<br>0.6-1.2,<br>1.2-2,<br>2-3.6,<br>3.6-6,<br>6-12,<br>12-20 | 0.2-0.32,<br>0.32-0.5,<br>0.5-0.8,<br>0.8-1.3,<br>1.3-2,<br>2-3.2,<br>3.2-5,<br>5-8,<br>8-13,<br>13-20 | 0.2-4,<br>4-20 | Total dust |
| Density (ρ) [kg $m^{-3}$] | 2500 (d ≤ 2 μm)<br>2650 (d > 2 μm) | 2500 (d ≤ 2 μm)<br>2650 (d > 2 μm) | 2500 (d ≤ 2 μm)<br>2650 (d > 2 μm) | 2600 | 2600 | 2500 (d ≤ 2 μm)<br>2650 (d > 2 μm) | 2650 | 2650 | 2500 |
| Optical Property Shape Model[§] | Spheroids | Spheres | Spheres | Spheres | Spheres | Spheroids (λ ≤2 μm)<br>Spheres (λ > 2 μm) | Spheres | Spheres | Spheres |
| Refractive Index | Colarco et al. (2014):<br>“Obs” model<br>$n_\lambda = 56$<br>λ = 0.25 – 40 μm | Balkanski et al. (2007):<br>2.7% hematite<br>$n_\lambda = 60$<br>λ = 0.17 – 40 μm | Sinyuk et al. (2003), Colarco et al. (2002), Dubovik et al. (2002), Volz (1973):<br>Calculated in bands | Woodward (2001):<br>$n_\lambda = 50$<br>λ = 0.227 – 10 μm | OPAC:<br>mineral model<br>$n_\lambda = 61$<br>λ = 0.25 – 40 μm | SW: Size-dependent (Klose et al. 2021)[¶]<br>LW: OPAC: mineral model<br>$n_\lambda = 61$<br>λ = 0.25 – 40 μm | OPAC:<br>mineral model<br>$n_\lambda = 61$<br>λ = 0.25 – 40 μm | Balkanski et al. (2007):<br>1.5% hematite<br>$n_\lambda = 61$<br>λ = 0.2 – 40 μm | OPAC:<br>mineral model<br>$n_\lambda = 1$<br>λ = 0.55 μm |

| | | | | | | | | | |
|---|---|---|---|---|---|---|---|---|---|
| Emitted Dust Particle Size Distribution[‡] | Ginoux et al. (2001), Chin et al. (2003) | Mass fraction of emitted dust to each bin: 0.1, 0.225, 0.225, 0.225, 0.225 | Cakmur et al. (2006) | Kok (2011) | 4-modes log-normal* | Kok (2011) | Tanaka and Chiba (2005), which is based on Shao et al. (1996) | D'Almeida (1987), 50/50 blend of "background" and "wind-carrying dust" | OPAC: Desert Model |
| Sub-bin Particle Size Distribution for Calculating Optical Properties | dM/d(log d) = constant<br>edge to edge @ 10 sub-bins<br>d< 2 μm bins integrated as in Tegen and Lacis (1996) | dM/d(log d) = constant<br>calculated at a single effective diameter per size bin<br>d ≤ 2 μm bins integrated as in Tegen and Lacis (1996) | Gamma distribution with mean at the effective radius of the bin and width = 0.2, extends beyond bin edges<br>d ≤ 2 μm bins integrated as in Tegen and Lacis (1996) | truncated lognormal<br>$\widetilde{D}$ = 0.25 μm<br>σ = ln(2.0) | 4-modes log-normal* | Optical properties calculated at a single effective diameter per size bin assuming a lognormal distribution with mass median diameter $\widetilde{\rho D}_v$ = 2.524 μm and σ = ln(2.0) (Zender et al., 2003) | dM/d(log d) = constant<br>edge to edge @ 10 size-bins | D'Almeida (1987), 50/50 blend of "background" and "wind-carrying dust" split at bin edges | N/A |
| RH Dependence | No | No | No | No | diameter grows linearly in the 0.95-1 RH range from $d_{dry}$ to $2.5d_{dry}$ | No | No | No | No |
| Online Radiative Transfer Number of Channels | SW = 9 (Chou-Suarez)<br>LW = 16 (RRTMG) | SW = 10[β]<br>LW = 8[β] | SW = 6[°]<br>LW = 33[°]<br>Longwave scattering approximated as in | SW = 14<br>LW = 16 | No | SW = 14 (RRTMG)<br>LW = 16 (RRTMG) | SW = 22<br>LW = 9 | SW = 6<br>LW = 9 | N/A |
| Longwave Scattering | No | No | Yes+ | No | N/A | No | No | Yes | N/A |
| $MEE_{550 \text{ nm}}$ [$m^2 g^{-1}$] per size bin | 3.02, 4.26, 3.01, 1.23, 0.62, 0.32, 0.17, 0.08 | 1.1, 2.6, 2.7, 0.9, 0.54, 0.28, 0.15, 0.08 | 4.41, 4.50, 2.91, 1.38, 0.64, 0.31, 0.17, 0.10 | 2.5, 0.95, 0.4 | 2.50, 0.83, 0.24, 0.07 | 1.90, 3.24, 2.93, 1.55, 0.73, 0.41, 0.22, 0.11 | 2.07, 3.82, 3.46, 1.41, 0.88, 0.52, 0.31, 0.19, 0.12, 0.07 | 0.70, 0.14 | 0.59 |
| $SSA_{550 \text{ nm}}$ per size bin | 0.98, 0.99, 0.98, 0.95, 0.92, 0.88, 0.82, 0.76 | 0.96, 0.98, 0.98, 0.93, 0.91, 0.86, 0.79, 0.7 | 0.97, 0.97, 0.96, 0.92, 0.88, 0.82, 0.76, 0.70 | 0.96, 0.90, 0.83 | 0.97, 0.893, 0.78, 0.70 | 0.98, 0.99, 0.99, 0.97, 0.95, 0.93, 0.90, 0.85 | 0.97, 0.98, 0.97, 0.93, 0.90, 0.86, 0.80, 0.74, 0.67, 0.60 | 0.96, 0.87 | 0.88 |
| References | Randles et al. (2017)<br>Colarco et al. (2014) | Zhao et al., (2018a, b) | Perlwitz et al. (2015)<br>Miller et al. (2006) | Rémy et al. (2019)<br>Bozzo et al. (2020) | (Sofiev et al., 2015) | Pérez et al. (2011)<br>Klose et al. (2021) | Tanaka and Chiba (2005)<br>Yukimoto (2011) tech memo | Johnson and Osborne (2011) | Lynch et al. (2016) |

[†] GEOS/GEFS, AM4, and ModelE/OMA all assume five dust size bins for transport, where the particles of diameter < 2 μm diameter are collapsed into a single transport bin, with its sub-bin properties apportioned as in Tegen and Lacis (1996).

[§] For spherical shape assumptions a homogeneous solid sphere is assumed with indicated refractive indices, and calculations are carried with a typical Mie scattering code (e.g., Toon and Ackerman (1981) or similar). Where spheroidal shape distributions are indicated, the shape distribution of Dubovik et al. (2006) is used for GEOS/GEFS and the probability distributions of particle shape obtained in Kok et al. (2017) based on laboratory measurements (e.g., Okada et al.,2001; Kandler et al., 2007) are used in MONARCH, with the optical properties in both cases drawn from the database of Meng et al. (2010).

[¶] The multi-component Maxwell Garnett theory is used to calculate refractive indices of internal mixtures of eight minerals, whose size-resolved proportions are estimated based on the mineralogical atlas from Claquin et al. (1999) combined with the brittle fragmentation theory of Kok (2011). The size- and wavelength-dependent real and imaginary indices are obtained for each of the 28 soil types in the atlas and finally the median values are used. The single-mineral refractive indices are taken from Scanza et al. (2015). At 550 nm the values in each bin (in increasing size order) of the imaginary component of the refractive index are: 0.0017, 0.0017, 0.0017, 0.0017, 0.0015, 0.0014, 0.0013, 0.0013.

[‡] This refers to the distribution of emitted dust mass fluxes across the model size bins.

*Weinzierl (2007): Radiatively-driven processes in forest fire and desert dust plumes, dissertation published at the University of Munich. The four-mode lognormal distribution is derived from airborne measurements of dust and fit with the following lognormal parameters: $r_{num}$ = (0.0375, 0.18, 0.49, 2.33) μm, σ = (1.9, 1.6, 2.0, 1.7), $f_{mod}$ = (0.90455, 0.06552, 0.02842, 0.00151).

[β] Freidenreich, S. M., and Ramaswamy, V. (1999), A new multiple-band solar radiative parameterization for general circulation models, *J. Geophys. Res.*, 104( D24), 31389– 31409, doi:10.1029/1999JD900456. Schwarzkopf, M. D., and Ramaswamy, V. (1999), Radiative effects of $CH_4$, $N_2O$, halocarbons and the foreign-broadened $H_2O$ continuum: A GCM experiment, *J. Geophys. Res.*, 104( D8), 9467–9488,doi:10.1029/1999JD900003.

[°] For the SW assumes a combination of refractive indices based on Sinyuk et al. (2003), Colarco et al. (2002), Dubovik et al. (2002) and uses the SW radiative transfer code of Lacis and Hansen (1974). In the LW refractive indices are based on Volz (1973).

+ There is no explicit scattering in the thermal longwave, but dust extinction efficiency is increased by 30% as in Schmidt et al. (2006) following Dufresne et al. (2002).

Table 21. Summary of dust model survey.

### 5.3.1 Dust Microphysical Properties

Table 21 shows the size bin number and ranges, dust particle density, shape model, sub-bin size distribution, complex refractive index, and size distribution at emission assumed by the models surveyed. Most of the models assume spheres for their dust particle shapes. However, GEOS, GEFS, and MONARCH assume non-spherical particles for computing dust optical properties. For GEOS and GEFS the spheroidal distribution is taken from Dubovik et al. (2006) (i.e. Dubovik_25 in Figure 6)(Colarco et al., 2014), which is also the basis of the dust shape assumptions of several retrieval algorithms described in the previous section. The MONARCH model assumes the tri-axial ellipsoid distribution described in Kok et al. (2017).

Table 21 shows other similarities among the models. All the models make similar assumptions for the dust density, 2500-2650 kg/m$^3$. Also, all models assume a fixed size distribution at emission. Two models, IFS and MONARCH, use the Kok (2011) size distribution at emission that is based on brittle fragmentation theory. The other models assume size distributions either from empirical formulations that were developed from various observations (GEOS/GEFS, ModelE, UM, SILAM), physically based models of dust entrainment (MASINGER), or distribute the emitted dust mass essentially equally across size bins (AM4). Except for SILAM, all models assume dust is hydrophobic; particle size does not increate with relative humidity through deliquescence.

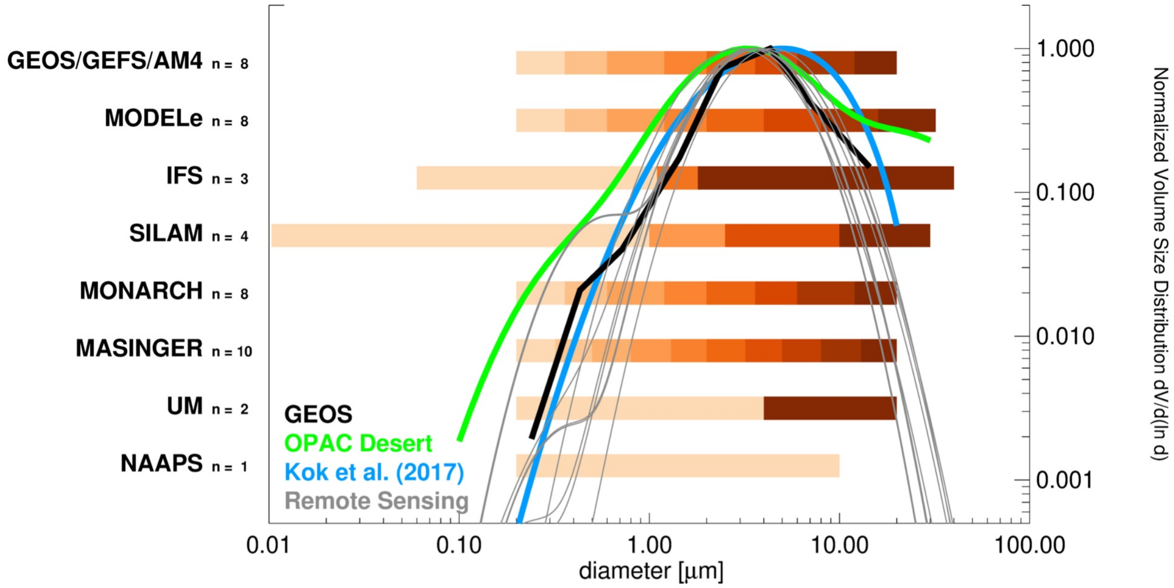

Figure 20. Range of dust particle size simulated in the various models shown in Table 21. Overlaid (right axis) is the dust volume distribution from two observationally-derived particle size distributions meant to represent global mean distributions (the so-called OPAC "desert" model and the Kok et al. (2017) distribution), the size distributions assumed in various remote sensing algorithms as summarized in Section 4, and the global mean dust particle size distribution from simulations with the GEOS model.

The number of size bins used to represent the dust PSD ranges from 1-10, shown graphically in Figure 20. The NAAPS model is the only model that assumes only one size bin. Thus, the dust size distribution in NAAPS does not evolve from emission through transport and loss, and remains fixed at the assumed observationally based, global mean representative OPAC "desert" model (Hess et al., 1998).

In general, all the models attempt to represent the dust particle size distribution in the range of about 0.2 – 20 µm geometric diameter. This range of particle sizes encompasses more than 99%

of the dust mass emitted according to the emitted size distribution derived by Kok (2011). This size range also encompasses 99% of the atmospheric dust mass distribution described by the OPAC "desert" model and the estimated global mean dust size distribution from Kok et al. (2017). This range of particle sizes is also compatible with the size distributions assumed in the remote sensing observations summarized in Section 4 (gray lines in Figure 20) and covers the most radiatively important part of the dust particle size distribution at visible wavelengths, where optical mass efficiency peaks for particles around 3-6 μm diameter and drops off rapidly for particles smaller than about 0.5 μm and larger than about 10 μm diameter. Note that larger particle sizes will impact longwave radiation, and only three models consider dust particles larger than 20 μm diameter, which, when included in forward RT simulations, better match observed thermal infrared brightness temperatures (Zheng et al., 2022). Finally, it is worth noting that none of the models surveyed here tries to represent the giant particles observed in recent airborne measurements (Does et al., 2018; Ryder et al., 2019, 2013a) that are present in small number concentrations and present a challenge in terms of calculating scattering properties for non-spherical particles.

The surveyed models represent dust composition by specification of a globally uniform size-independent spectral complex refractive index, which derives from common compilations that are based on fundamental datasets (see Table 21 for specific references)(Figure 21). Not all the models calculate optical properties at all the wavelengths shown in Figure 21; models that do not include aerosol-radiation interactions may only need to compute optical properties at a small subset of (usually visible) wavelengths for purposes of computing spectral AOD, SSA, and aerosol attenuated backscatter to compare with remote sensing observations. For wavelengths shorter than 1 μm, Figure 21 shows that all the assumed refractive indices converge to approximately the same spectrally constant value for the real part of the refractive index, ~1.53. This is in contrast with the wider range of real refractive indices assumed by the remote sensing retrievals (Figure 16). However, there is considerably more variability among the model assumptions in the longwave. For the assumed imaginary part of the refractive index, there is large variability across the full spectral range, but that is well within the range of measurements reported for bulk dust (Di Biagio et al., 2019, 2017) (see Figure 5). Notably, many of the models in Table 21 use the OPAC or Volz (1973) dataset of LW refractive indices that have been shown to be inconsistent with the Kramers-Kronig constraint (Di Biagio et al., 2014). Within the atmospheric window (between 8 and 12 μm), the imaginary part of these two indices is at the upper end of the range retrieved by Di Biagio et al. (2017) from a worldwide collection of 19 soil samples (Figure 5, gray shading). This suggests that with regard to the model LW DRE, excessive absorption may spuriously compensate for an underestimate of larger particles

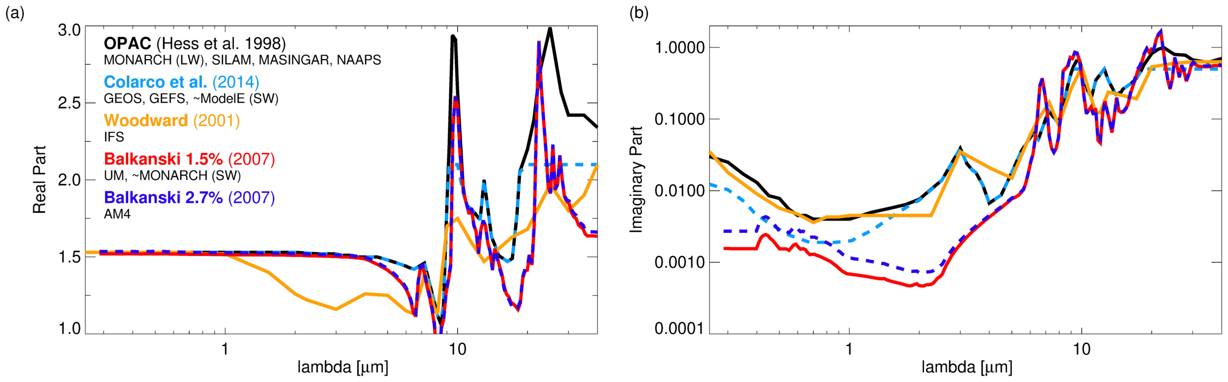

Figure 21. Spectral dust refractive indices ((a): real part; (b): imaginary part) used in the indicated models from Table 21.

### 5.3.2 Dust Optical Properties

The particle size distribution, dust composition (represented by refractive index), and particle shape are fundamental to calculating dust optical properties needed to compute diagnostic aerosol optical quantities (e.g., AOD, SSA, and AE) that are used for comparing the model predictions of aerosol mass loading with remote sensing retrievals, aerosol-radiation interactions internal to the model, and data assimilation of retrieved aerosol geophysical parameters or satellite radiances.

In addition to the specific dust property assumptions, there is also the practical matter of the numerical methods for computing the optical properties. For spherical dust particles (assumed in most of the models surveyed here), this is accomplished using Mie theory. For GEOS, GEFS, and MONARCH, the non-spherical dust optical properties are based on the precomputed kernels from the Meng et al. (2010) database of single scattering properties for triaxial ellipsoids that is sub-selected to the axis ratio distribution either of Dubovik et al. (2006) or Kok et al. (2017). Regardless of the approach, we note that the optical properties need to be computed at a much higher size resolution than the 1 - 10 size bins used in the models here, especially for smaller diameters that are comparable to visible wavelengths. The "Sub-bin particle size distribution" row in Table 21 summarizes this technical point, including the number of sub-bins over which the optical property calculation is made and the assumptions on the functional representation of the sub-bin size distribution. Quantities calculated at these higher size resolutions are then integrated to the transported size bins to specify, e.g., the mass extinction efficiency (MEE) for each size bin used to compute the AOD. These precomputed spectral optical properties are compiled in look-up tables (LUTs) that are used in the various modeling frameworks.

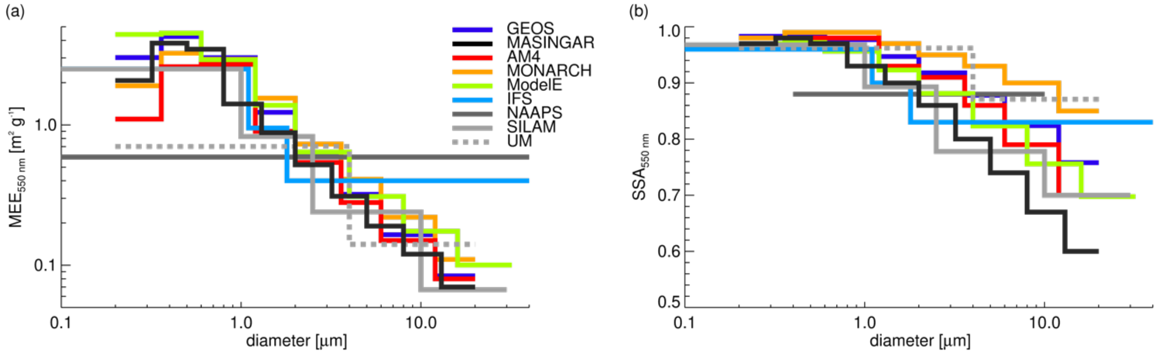

Figure 22. (a) MEE and (b) SSA at 550 nm provided by the surveyed models.

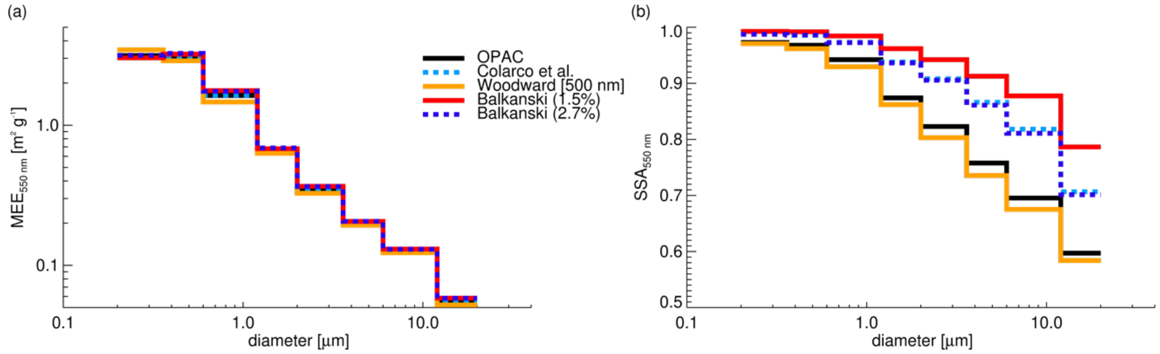

Figure 23. (a) MEE and (b) SSA at 550 nm calculated using the refractive indices shown in Figure 21 but with the sub-binning information from the GEOS/GOCART model (assuming spherical optics, see Figure S2 for an equivalent figure assuming spheroidal optics). Note that the Woodward database provides refractive index information at 500 nm, which is used here.

Figure 22 shows the self-reported, size-resolved MEE and SSA at 550 nm wavelength provided by the surveyed models. These values are also tabulated in Table 21 in the rows labeled ‘MEE per size bin’ and ‘SSA per size bin’. Figure 23 shows the same quantities computed using the GEOS-model eight size bins and sub-bin distribution, but for the complex refractive index assumptions of the different models (Figure 21). The assumed GEOS binning scheme is used to emphasize the effect of the different refractive indices used by the models without the confounding effect of their differing bin and sub-bin assumptions. For the MEE in Figure 23 that is derived using a common size distribution, there is very little sensitivity to the choice of refractive index, which is expected since all the refractive index assumptions have nearly the same value for the real component at 550 nm, as noted earlier. By contrast, for the self-reported values of MEE (Figure 22) there are significant differences especially for smaller particle size bins (although the models have the same trend in MEE). The differences in the self-reported MEE thus arise from the number and width of size bins used to resolve the particle size distribution, the sub-bin particle size distribution assumed for the integration of optical properties, and other specific details of how the optical property calculations are carried out by the individual models. A similar result is found when the calculations are performed assuming non-spherical optics, using the shape distribution assumed by GEOS, as in Figure 23. As expected, the non-spherical optics result in a slightly higher MEE.

Focusing first on the number and width of the size bins, GEOS, GEFS, AM4, and MONARCH are all using the same layout of eight size bins. ModelE is similar, using the same bins in the sub-2 μm diameter range, but making the bins slightly wider at larger particle sizes. MASINGAR carries ten size bins spanning the same range as GEOS, GEFS, AM4, and MONARCH. The shared heritage of GEOS, GEFS, AM4, and ModelE results in the commonality that the four sub-2 μm diameter particle bins are used for radiative calculations, but aggregated into a single bin that is transported. Transported mass is distributed into the four sub-2 μm bins according to globally invariant fractions calculated by Tegen and Lacis (1996). By contrast, MONARCH and MASINGAR transport all their size bins explicitly as separate tracers. SILAM, IFS, UM, and NAAPS have respectively four, three, two, and a single size bin apiece.

In particular, the single UM size bin covering the entire 0.2 - 4 μm diameter range has lower MEE than the bins of the other models covering the same size range, except for the largest bins in that range for GEOS, ModelE, and MONARCH. Accordingly, we expect very little sensitivity in UM to the calculated size distribution of small dust particles but expect greater sensitivity in the more finely resolved models like GEOS, ModelE, and MONARCH.

In contrast to the MEE, for SSA the model assumptions result in mostly similar values of SSA for the smallest diameters less than about 0.6 μm diameter, with values between about 0.96 - 0.99

(Figure 22). The range widens at larger particle sizes, with MONARCH generally being the least absorbing. Increased absorption at larger particle sizes is more apparent in models with the highest number of size bins, with MASINGAR reporting the lowest single scattering albedo at the coarsest sizes. In Figure 23, when a single set of size bins are utilized (based on GEOS), the differences in size resolved SSA are consistent with the differences in the assumed imaginary component of the refractive index between the models.

### 5.4 Implications of Dust Optical Property Assumptions for Size-Integrated AOD, Absorption, and Forcing

In this section, we explore the implications of the choice of number of size bins and sub-bin distribution on the models' respective abilities to represent size-integrated optical properties, given a prescribed dust particle size distribution. That is, we assume the dust size distribution is known and we ask how well the models would agree on the AOD, co-albedo (i.e., 1 - SSA), and shortwave forcing if that size distribution were apportioned according to the models' size bin structures and the resulting optical properties are integrated over size. We assume here for convenience that the size distribution is described by a single lognormal mode with a specified width (σ, log-size standard deviation) and volume median diameter $\widetilde{D_v}$, exploring the range of $\widetilde{D_v}$ = 1.5 - 5.0 μm and σ = ln(1.5) to ln(2.5), following the analysis of dust particle size distributions in Reid et al. (2008). An additional case is considered where the dust particle size distribution is the OPAC desert model (see Figure 20), which is the NAAPS assumption. For all cases, to normalize our results we assign a total mass burden such that the NAAPS model, which represents dust with a single bin, has an effective AOD=1. This works out to a mass loading of 1.695 g $m^{-2}$. As such, regardless of the underlying particle size distribution, for the given mass, the NAAPS model always predicts the same optical properties.

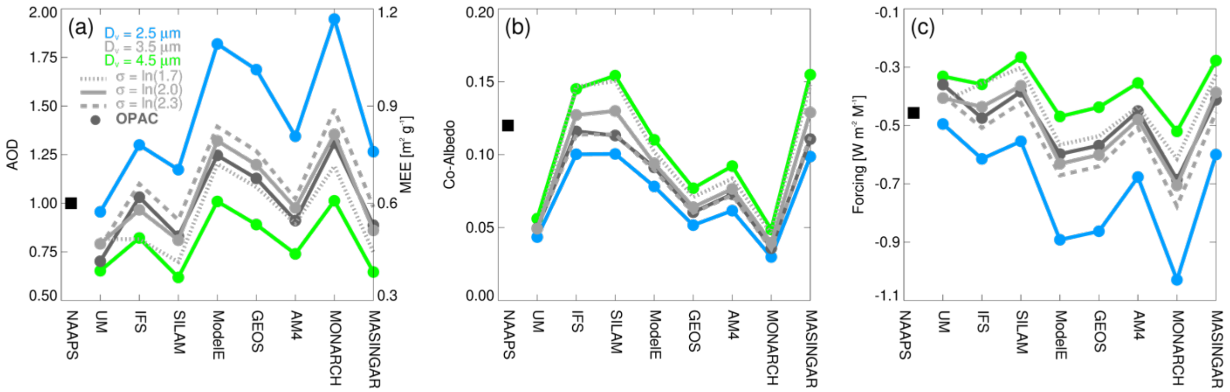

Figure 24. The results of an experiment where a prescribed mass loading of dust M = 1.695 g m$^{-2}$ is distributed across the size bins of the various models assuming the indicated lognormal modes. The figures show (a) the integrated AOD, (b) the aerosol co-albedo (1-SSA), and (c) an estimate of the shortwave radiative forcing of dust per unit M that results over a cloud-free, dark ocean surface calculated using the parameterization of Chýlek and Wong (1995). The single-size NAAPS model produces the same results for each size distribution tested and is shown as the solid black square. The per-size bin optical properties used here are those reported in Table 21 and Figure 19 (i.e., the models' self-reported size-resolved optical properties). Co-albedo is computed by weighting the per-size bin SSA with the per-size bin AOD prior to integration. For simplicity, results are shown centered on the volume median diameter and width of the distributions in Reid et al. (2008) ($\widetilde{D_v}$ = 3.5 µm, σ = ln(2.0); $\widetilde{D_v}$ = 2.5 µm, σ = ln(2.0), $\widetilde{D_v}$ = 4.5 µm, σ = ln(2.0); $\widetilde{D_v}$ = 3.5 µm, σ = ln(1.7); $\widetilde{D_v}$ = 3.5 µm, σ = ln(2.3)).The dark grey line is the same calculation performed using the OPAC desert dust model particle size distribution.

Figure 24 shows the AOD, co-albedo, and direct shortwave radiative forcing using the models' self-reported, per-size bin MEE and SSA as shown in Figure 22, with the models ordered from from the lowest to highest number of size bins used to represent the particle size distribution. AOD and co-albedo are straightforward integrals of the per-bin optical properties given the apportioned mass distributions. An estimate of the cleary-sky globally averaged direct radiative forcing is made using the simple parameterization of Chýlek and Wong (1995), which reduces to:

$$\Delta F_R \sim -2 \cdot (1-a)^2 \cdot \beta \cdot \tau_{sca} - 4 \cdot a \cdot \tau_{abs} \qquad \text{Eq 10.}$$

where a is the surface albedo (equal to 0.06, assuming a dark ocean), β is the up-scattered radiation fraction (equal to 0.31, computed from the GEOS optics and relatively insensitive to the dust particle size distribution used), and $\tau_{sca}$ and $\tau_{abs}$ are respectively the scattering and absorbing optical depths ($\tau_{abs}$ = AOD*co-albedo and $\tau_{sca}$ = AOD - $\tau_{abs}$). A negative relative forcing (i.e., cooling) reflects the overall scattering nature of the aerosols in the mid-visible wavelengths when the aerosol layer is over a dark surface.

Although we explored a range of parameter space, Figure 24 shows the results only for six size distributions, five of which bound the expected dust size range following Reid et al. (2008), who reports a survey of observations that suggest a "common mode" for transported dust particles of $\widetilde{D_v}$, = 3.5 ± 1.0 μm and $\sigma = \ln(2.0 \pm 0.3)$. A sixth distribution based on the OPAC desert dust model particle size distribution is also indicated. The disagreement among the models for a prescribed PSD is striking, with a ~50% diversity in the AOD among the models, and a commensurate range of values in the computed forcing. This likewise implies a wide range of effective MEE, from ~1.2-0.35, which is comparable to the range in MEE values for the remote sensing retrievals; ~0.6 for most retrievals, and ~0.9-1.2 for MISR. This implies that for a given AOD estimate, the implied underlying aerosol mass loadings by the models and remote sensing retrievals can vary by ~50-100%, and these aerosol model assumptions introduce substantial uncertainty in the interpretation and comparison of the model simulations and the retrievals.

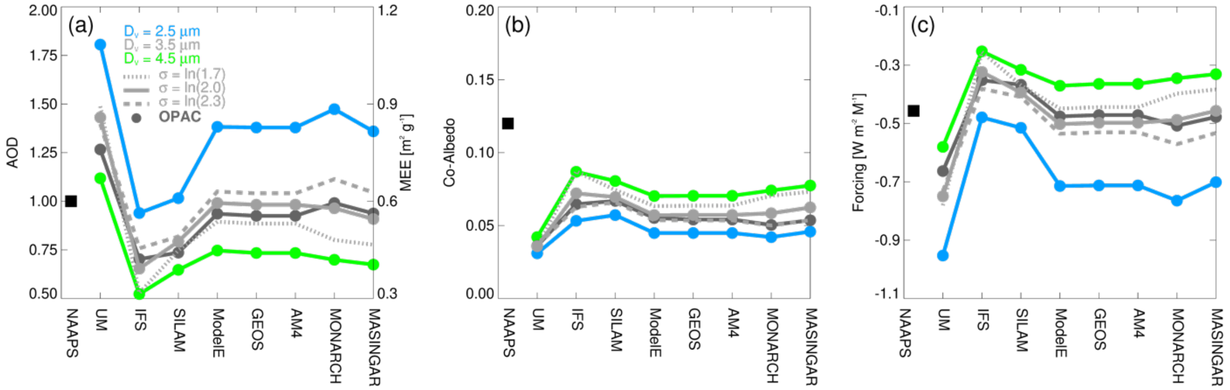

Figure 25. Like Figure 24, except here the optical properties are computed with the GEOS sub-bin distribution (dM/d(log d) = constant ) and refractive index at 550 nm (Colarco et al. 2014), but assuming the various models' bin spacing. All calculations are for spherical particles.

We repeat this analysis in Figure 25, but here we recompute the optical properties for each model using the GEOS sub-bin distribution (dM/d(log d) = constant) and refractive index assumptions, but maintain the overall size bin number and spacing of the various models. Note that the Tegen and Lacis (1996) integration scheme for sub-2 μm diameter particles is applied to the models that implement it – GEOS, GEFS, AM4, and ModelE – but that this has only a small impact on the overall results. Furthermore, all calculations here assume spherical particles. This analysis is thus exploring only the differences among models due to size bin resolution.

Notably, in Figure 25, GEOS and AM4, which have the same size bins and sub-bin distributions, have identical results to one another now, while in Figure 24, where refractive index and shape assumptions differend, the AODs were different. MONARCH, which has the same bin layout as GEOS and AM4, has a slightly different AOD because it does not use the Tegen and Lacis (1996) distribution to aggregate the sub-2 μm part of the size distribution, indicating that this assumption is not terribly significant. MASINGAR now has a very similar AOD as GEOS, AM4, ModelE, and MONARCH, whereas the models with fewer size bins differ significantly. Interestingly, UM now has the highest AOD, whereas IFS has the lowest.

The variability in dust single-scattering co-albedo has now essentially disappeared, indicating that the calculated absorption is mainly sensitive to the underlying refractive index assumption, although the UM size bin scheme does lead to significantly lower co-albedo than the other models, and likewise radiative forcing. This, and the high AOD, indicate that the large 0.2 - 4 µm diameter size range of the first UM size bin and a dM/d(log d) = constant sub-bin distribution assumption may bias the weighting towards smaller, more scattering particles. Conversely, the large 1.8 – 40 µm diameter size range of the largest IFS size bin may bias the weighting towards larger, more absorbing particles.

The calculations shown here assume spherical optics. See Figure S3 for has the same calculation but assuming the GEOS spheroidal distribution; aside from slightly higher resulting AOD for spheroids and some small impacts on co-albedo and forcing there is no major difference from the results in Figure 25.

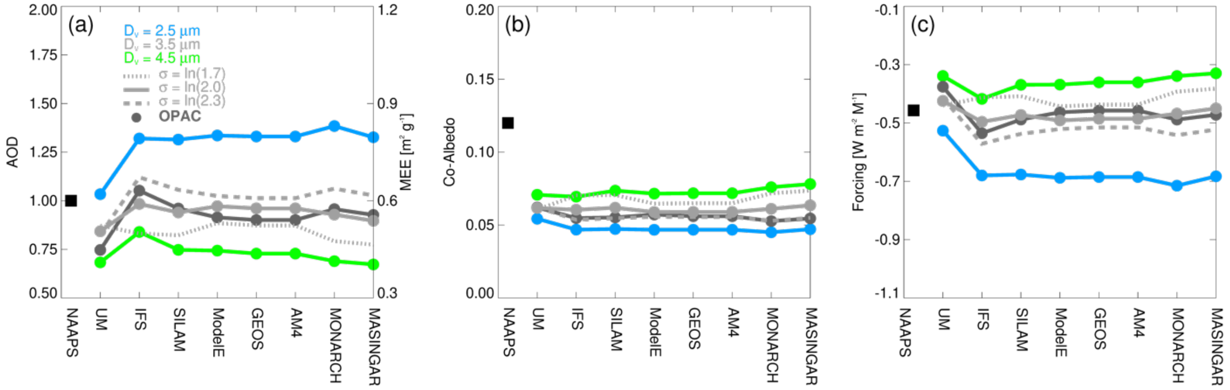

Figure 26. As in Figure 25, but now assuming a sub-bin distribution described by $\widetilde{D_v}$ = 2.524 µm and σ = ln(2.0).

By default, GEOS, AM4, and MASINGER assume a sub-bin distribution dM/d(log d) = constant (Table 21), which is what is shown in Figure 25. In Figure 26, we redo the calculations replacing the GEOS sub-bin distribution with the log-normal sub-bin distribution used in MONARCH: assuming $\widetilde{D_v}$ = 2.524 µm and σ = ln(2.0). Here, we see that all but one of the models (UM) have essentially converged to the same AOD, co-albedo, and forcing for the same mass loading. There are some differences among the models at the coarser $\widetilde{D_v}$ (i.e., $\widetilde{D_v}$ = 3.5 and 4.5 µm), but the variability between the models is much reduced compared to the previous sensitivity test, when using the GEOS sub-bin distribution (Figure 25). Here again, UM has changed its nature, now having the lowest AOD, reflecting the strong variability in particle scattering properties over the large 0.2 - 4 µm diameter size range of the first UM size bin. A similar figure (Figure S4) shows the same calculation but assuming a $\widetilde{D_v}$ = 3.5 µm for the sub-bin distribution, with similar results but a better convergence of the models for the $\widetilde{D_v}$ = 3.5 µm particle size distribution assumption.

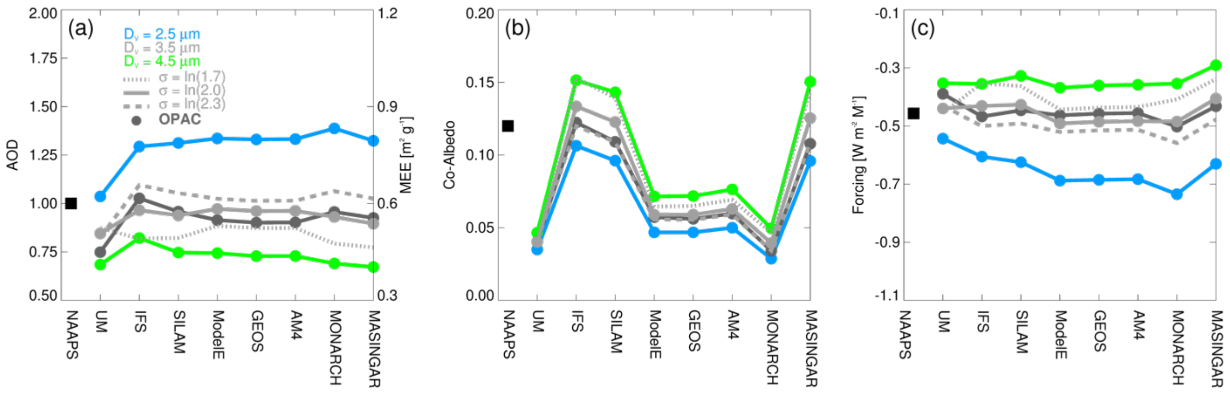

Figure 27. As in Figure 26, but now back to the models' own refractive index choices.

Finally, in Figure 27 we bring the pieces back together by recomputing the optical properties using the models' stated size bins and refractive index choices but retaining here the MONARCH lognormal sub-bin particle size distribution assumption as in Figure 26. Again, this calculation is done for spherical particles. The result is that the models are converged in terms of AOD, with all the models except UM having essentially the same MEE as NAAPS (right axis on the AOD figure) and an AOD ~ 1 for the $\widetilde{D_v} = 3.5$ μm and OPAC desert model PSDs. Note that this means that for a given mass, when the size distribution differs significantly from the NAAPS OPAC desert model assumption, all the other models differ from NAAPS. By bringing the models' own refractive index choices back into play, the models resume their original representations of absorption, as in Figure 24 (i.e., IFS, MASINGAR, and SILAM all have the strongest absorption). The radiative forcing is also similar among the models. Thus our analysis shows that the majority of this inter-model diversity is shown to be the result of the different sub-bin particle size distribution assumptions (e.g., dM/d(log d) = constant in GEOS/GEFS, AM4, and MASINGAR, a gamma distribution used in ModelE, and a smoother, lognormally shaped distribution as in MONARCH).

Current observations are insufficient to guide an optimal single sub-bin distribution assumption. Furthermore, a single sub-bin distribution assumption may be inadequate if the actual dust particle size distribution varies significantly during transport. Until we have better observational characterization, we suggest that inter-model comparisons of models employing a sectional scheme coalesce on a common sub-bin distribution assumption based on our current limited observations, such as the OPAC desert dust model, or the Kok et al. (2017) estimate for a global ambient dust size distribution. This recommendation does not hinder models from exploring real diversity of refractive index and particle shape assumptions, but rather is a suggested structural improvement that would reduce some uncertainty in intercomparisons among existing models. As models typically use common satellite remote sensing observations of AOD to constrain the dust lifecycle (i.e., tuning dust source strengths and removal efficiencies to match climatologies), adopting a similar sub-bin distribution assumption in model intercomparisons would aid in understanding how different physical parameterizations of dust processes implemented in models impact dust mass fluxes.

The last two sections have highlighted the difficulty in constraining dust distributions and physical processes via dust optical impacts in the atmosphere, as the Earth is a complex system, containing myriad dust sources, mixtures of many aerosol components, and their interactions, as well as complex radiative effects over ocean and different land surfaces. Comparatively, a planet such as Mars provides an opportunity to study dust in a relatively simpler environment that is dominated by dust. In the next section, we summarize the current understanding of Martian dust optical properties for remote sensing and planetary modeling applications.

# 6 Measurements of Mars Dust Microphysical Properties and Global Circulation Models

Dust is omnipresent in the Martian atmosphere, with spatial and temporal variability that defines a global dust cycle of exchange between the surface and atmosphere. Martian dust is both a regulator and a tracer of climatic processes on Mars, which was understood from the beginning of Space Age exploration of Mars with Mariner 9 (Gierasch and Goody, 1972; Leovy et al., 1972).

Two prime methods are believed to control dust lifting on Mars: 1) similar to Earth, wind stress on the surface initiates saltation of larger grains (and possibly direct suspension of smaller dust particles) that subsequently bounce and eject smaller dust particles into the atmosphere, and 2) unique to Mars are the seemingly ubiquitous dust devils (Jackson, 2022; Thomas and Gierasch, 1985). Dust is later removed from the atmosphere primarily through sedimentation and settling (dry deposition) with perhaps additional removal as the nuclei of precipitating water ice or $CO_2$

ice cloud particles (wet deposition) (Kahre et al., 2017). Kahn et al. (1992) and Kahre et al. (2017) provide more complete overviews of the state of knowledge of the Martian dust cycle at their respective times of publication.

## 6.1 Mars Dust Microphysical Properties

As of yet, no Martian dust samples have been returned to Earth, and thus our primary understanding of dust properties comes from analysis of remote sensing observations from orbit and multiple landers across the planet. Atmospheric observations dating back to Mariner 9 have suggested how Martian dust interacts with radiation. Foundational work was conducted with the Viking Orbiter (primarily in the infrared) and Landers (through near-Sun visible band imaging) to understand dust particle properties and their scattering and absorption (Pollack et al., 1995, 1979, 1977). More recently, nearly uninterrupted observations have been conducted with a variety of spectrometers, cameras, and radiometers from orbit with additional studies from shorter-lived landers (e.g., Tomasko et al., 1999) and rovers. The Thermal Emission Spectrometer, Planetary Fourier Spectrometer, Thermal Imaging System, and Mars Climate Sounder have provided over a Mars decade of dust abundances and distributions, creating a robust climatology (Montabone et al., 2015; Smith, 2009, 2004; Wolkenberg et al., 2018). Wolff et al. (2017) gives an overview of the current state of knowledge of the optical properties of Martian dust derived from these measurements that we summarize briefly here. However, typically, each Mars-observing instrument team has developed their own tailored dust model for the retrieval of dust abundances or particle properties (e.g., Kleinböhl et al., 2009).

Observations indicate that the atmospherically exchangeable reservoir of Martian dust is globally homogenous in its composition (e.g., Berger et al., 2016). Martian dust is largely feldspar, with trace amounts of other minerals such as pyroxene and olivine, and an important component of nanophase iron oxide, which gives the dust its characteristically Martian ocher color (e.g., Hamilton et al., 2005). The sulfur to chlorine ratio of Martian dust, distinct from other soils, suggests a possible single parent geologic source region (Ojha et al., 2018). Wavelength-dependent real and imaginary components of the dust refractive index from the visible through the thermal infrared (up to ~30 μm) developed by Wolff et al. (2009, 2006) are widely used by the community to represent the Mars dust composition. This refractive index database was created by combining upward-looking Mars Exploration Rover observations with downward-looking Mars Thermal Emission Spectrometer (TES) and Reconnaissance Orbiter Combined Reconnaissance Imaging Spectrometer for Mars (CRISM) observations.

The true structural form of Martian airborne dust particles is unknown due to the lack of direct sampling or observation. When imaged on the surface (at maximum resolutions insufficient to resolve the expected size of an individual grain), it appears to take the form of clumps and conglomerates tens to hundreds of μm in diameter (e.g., Yingst et al., 2020). Mie theory has often been applied (Wolff et al., 2017) in forward modeling of dust optical properties, although more recently applying a T-matrix method (e.g., Mishchenko et al., 2002) to other shapes such as cylinders has been more effective at reproducing observed phase functions of Martian dust. Wolff et al. (2009) applied a T-matrix method with randomly oriented cylindrical dust particles with aspect ratios of 1 to provide a database of dust optical properties that is widely used by the community.

Additional information on dust particle shape and size has been retrieved through analysis of dust's scattering properties. Modified gamma or log-normal size distributions are typical assumptions in these analyses. Thus, retrievals are made of the effective diameter ($D_e$), and less often the effective variance ($v_e$), which is more often assumed. Canonical vertical column-integrated dust particle effective diameters are typically 2.8-3.4 μm under typical atmospheric dust loading (Smith, 2008), with larger sizes ($D_e$ > 8 μm) during dust storm conditions (Clancy et al., 2010; Lemmon et al., 2019). Less information is available about the vertical distribution of dust particle sizes, but smaller sizes have been noted at higher altitudes (10-50+ km) as would be expected from gravitational sorting by size (Fedorova et al., 2009; Guzewich et al., 2014).

## 6.2 Mars General Circulation Models

Dedicated Mars general circulation models (GCMs) were first developed in the late 1960s and 1970s (e.g., Leovy and Mintz, 1969). Modern Mars GCMs include full treatment of boundary layer physics, Mars' seasonal $CO_2$ and $H_2O$ cycles and their exchange between surface and atmospheric reservoirs, dust lifting and sedimentation, and parameterizations for processes such as gravity wave drag (e.g., Forget et al., 1999; Haberle et al., 2019; Richardson et al., 2007). Additionally, dedicated Mars mesoscale models are used for understanding smaller-scale meteorology at the scale of individual terrain features or spacecraft landing sites (e.g., Rafkin et al., 2002; Tyler and Barnes, 2015).

Proper modeling of the Martian dust cycle and dust radiative properties is critical to credibly reproduce the modern Martian climate in Mars GCMs. Dust reaches up to eight or ten scale heights in the Martian atmosphere during the dusty southern summer season, when the largest dust storms tend to originate. Until the last decade, the atmospheric thermal structure was the most well-known aspect of the Martian climate, and Mars GCMs were tuned to match temperature observations by spacecraft. This tuning was often accomplished through adjustment of dust opacity or dust optical properties (Madeleine et al., 2011). More recently, improved physical parameterizations, radiative transfer subroutines, and more comprehensive observations of the Martian atmosphere have led to self-consistent modeling of the Martian dust cycle, concurrently with reasonable reproduction of the base thermal structure.

Currently, most operational Mars GCMs (Haberle et al., 2019; Madeleine et al., 2011; Natarajan et al., 2015) use dust optical properties (single scattering albedo, asymmetry parameter, and extinction) described by Wolff et al. (2009). There are two main approaches used to describe the dust particle size distribution: 1) direct prescription of effective diameter and variance (typically 3-4 μm effective diameter, and 0.3-05 effective variance) of a log-normal distribution, and 2) a multiple size bin approach that self-consistently evolves in the atmosphere through lifting and deposition processes (Haberle et al., 2019; Madeleine et al., 2011), much like the sectional approaches implemented in Earth system models and CTMs described in the previous section.

The variety of Mars GCMs have provided new insights into the physical processes at work that reproduce observed aspects of the dust cycle. Of particular note is the link between locations of net dust lifting or net dust deposition (Ruff and Christensen, 2002) and the seasonality of Martian dust storms. Mars GCMs that treat the surface dust reservoir available for lifting as “infinite” (i.e., global, excluding ice-covered surfaces, and unable to be depleted) can generally reproduce the annual cycle of atmospheric dust loading (e.g., a less dusty northern hemisphere spring and summer around aphelion and a dustier southern hemisphere spring and summer around perihelion) and correctly simulate dust storms in climatologically-favored locations, but suffer from a lack of realistic interannual variability. This is particularly true when trying to reproduce the stochastic nature of Martian “global dust storms,” which generally occur irregularly every 3-6 Mars Years (Basu et al., 2006, 2004; Kahre et al., 2006; Newman et al., 2002). Attempts to model a “finite” surface dust reservoir (where individual grid cells can become depleted of dust and must be refilled by deposition) have all resulted in a quiescent dust cycle after multiple years of simulation, whereupon all dust is removed to model grid cells where it is not lifted (Kahre et al., 2005; Mulholland et al., 2013; Newman and Richardson, 2015).

The enigmatic nature of global dust storms remains a driving question in Mars atmospheric science. Their formation and growth mechanisms remain largely unknown. Similarly, free-running Mars GCMs do not precisely replicate the observed seasonality in atmospheric dust opacity and dust storm occurrence, particularly in the dustier second half of the Martian year (Mars southern summer). Both deficiencies may be sourced, at least in part, from poor understanding of surface sources and sinks of dust and how they may change seasonally. Improving our understanding of global dust storms or surface dust sources and sinks will be challenging with orbital remote sensing alone (both existing and planned spacecraft), although continued observations by the fleet of spacecraft currently operating at Mars, as well as the recently deployed James Webb Space Telescope, remains valuable to document future events and extend the existing dust climatology. The planned return of geologic samples to Earth by the NASA/ESA Mars Sample Return program in the early 2030s will provide terrestrial laboratories with Martian dust for the first time (Farley et al., 2020). This will allow comprehensive measurements of dust composition, particle shape and structure, and optical properties at all wavelengths, for at least a few samples, and provide a unique opportunity for reinterpretation of existing spacecraft data while also upgrading microphysical and radiative transfer models in Mars GCMs.

## 7 Summary

This paper is our consolidated attempt at a comprehensive survey of our current understanding of dust properties from field and laboratory measurements, the numerical methods to estimate optical properties from microphysical information, as well as the representation of dust optical properties in various remote sensing algorithms, and Earth and Mars global circulation models. Dust scientists are presented with a large and expanding set of observational products, but the underlying measurements are often incomplete descriptions of dust particles, requiring additional assumptions to create diagnostics that can be compared to other observational products or models. The retrieval algorithm and global modeling assumptions are not always consistent, and our goal is to document these assumptions as a first step toward meaningful comparison. Our review elucidated several similarities and differences among the paradigms for studying dust. A fundamental property of dust that differentiates it from other aerosol species is the complex emission process that yields a myriad of irregularly shaped and inhomogeneous particles with significant consequences to their optical properties. However, global models and most remote sensing algorithms are still limited to representing dust as particles of homogeneous composition that are smooth spheres or spheroids (and less often as ellipsoids with three distinct dimensions). The exceptions are the MISR retrieval dust models, and Mars remote sensing applications that utilize grains and cylinders, respectively. In particular, global Earth system models favor spheres, with only two models surveryed utilizing spheroids, while the remote sensing applications favor spheroids. The latter can be traced to the wide availability of the GRASP and DSL scattering codes and their implementations of the Meng et al. (2010) database of single scattering properties of spheroidal and ellipsoidal dust particles.

For the refractive index, bulk dust *in situ* observations of the real part of the refractive index coalesce around the value ~1.5 in the visible spectral range, and all of the Earth global models and remote sensing algorithms have adopted this value. However, for the imaginary part of the refractive index, *in situ* observations of bulk dust and individual minerals vary widely, by an order of magnitude across the visible spectral range. This gives latitude for models and retrieval algorithms to assume widely varying, but still plausible, values for the imaginary refractive index. For the remote sensing algorithms, the imaginary refractive index assumptions cluster between ~0.001 and ~0.003 at 500 nm. This is at the upper end of the range of ~0.0006 to ~0.005 reported by Di Biagio et al. (2019, 2017) who aerosolized 19 soil samples from five continents. Meanwhile, the global model assumptions for imaginary refractive index vary by nearly an order of magnitude, from ~0.001 to ~0.01 at 500 nm. The higher values are still are based upon the measurements of Patterson et al. (1977).

In terms of assumptions for particle size distribution, most Earth retrieval algorithms tend to assume similar bimodal lognormal distributions spanning the size range 0.02 - 40 μm, with a fine mode centered at ~0.3 μm and a coarse mode centered at ~4 μm. These assumptions have a common heritage in the AERONET climatology of retrieved size distribution at dust-dominated sites. However, the MISR algorithm is distinguished as it assumes three lognormal modes. Mars retrieval algorithms also tend to assume bimodal lognormal distirubtions, although some utilize gamma distributions. The variability in assumed PSDs results in a range of effective diameters from 0.5 μm to 2.5 μm for the Earth retrieval algorithms. The Mars algorithms assume coarser particles with effective diameters in the 2.8 – 3.4 μm range. Despite the variability in assumed PSDs, the comparison of the resulting phase functions for the Earth dust retrievals agree well at side scattering angles. However, substantial variability is found in the DoLP and the phase function at backscattering angles, resulting in large variability in lidar ratios spanning the range 15-60 sr at 532 nm. A notable difference between passive and lidar remote sensing retrievals is the use of observation based constraints for lidar ratios and lidar linear depolarization ratio in lidar retrievals, rather than the use by passive retrievals of a forward calculation of scattering properties based on a physical dust model. This paradigm requires that the lidar retrieval algorithms make gross assumptions for observing scenes with mixtures of aerosol species. The range of lidar retrieval assumptions for lidar ratio do however span the same range as the passive retrievals forward dust models. Likewise, nearly all the passive dust models derive a 532 nm lidar depolarization ratio greater than 0.2, which is the threshold for identifying dust in CALIOP observations.

Unlike retrieval algorithms that prescribe functional forms to the assumed PSD, global models simulate the size distribution from the balance of size resolved sources and sinks of dust. The models surveyed here represent dust PSD through a number of relatively coarse size bins. The choice of number, placement of the size bins, and sub-bin particle size distribution assumptions (e.g., dM/d(log d) = constant versus a smoother, lognormally shaped distribution) determines the ability of the models to represent PSDs and their impacts on optical properties. The surveyed global Earth system models assumed between 1 and 10 size bins spanning various diameter ranges, but none exceeding 32 µm. Sensitivity tests revealed that even for a common underlying size distribution, the varying number of size bins results in large variability in optical properties, such that there is a ~50% diversity in the AOD among the models, and a commensurate range of values in the computed forcing. The same limitations would apply to Mars global modeling, as they employ the same multiple size bin approach.

The model and remote sensing optical properties can best be compared through the MEE, which is the parameter used by global models to convert remote sensing estimates of AOD to column aerosol mass concentration, which is the parameter transported and transformed by global models. Deriving the MEE requires assumption of a dust particle density. Among the models surveyed, the dust density assumptions range modestly from 2500-2650 kg $m^{-3}$. Taking a nominal dust density of 2500 kg $m^{-3}$, we were able to convert the remote sensing retrieval aerosol extinction at 550 nm to MEE. Nearly all of the remote sensing retrieval dust models have very similar MEEs of ~0.6, with the exception of the MISR models, which yield an MEE of ~1.0. It is notable that the value of 0.6 is approximately equal to the 0.59 value used by the NAAPS model that assumes one size bin with the canonical OPAC dust size distribution. Given the sensitivity of the global transport models' MEE to the size range of particles considered, assumption of the sub-bin size distribution, and the bin size and spacing, the models can represent a larger spread in MEE, from 0.35 to 1.2. Thus it is possible and very likely that comparisons of satellite based dust AOD retrievals and simulations of dust AOD from global models are underpinned by dust models with very different optical properties. These physical inconsistencies, which also exist to a lesser extent among different satellite retrieval products, are largely unacknowledged by the scientific community. This paper has documented this mismatch as a step toward creating a more consistent and rigorous comparison.

# 8 Discussion

The irregular shapes of dust particles defy simple mathematical representation (Buseck et al., 2000; Scheuvens and Kandler, 2014)(Figure 3); the lack of comprehensive and realistic shape models is an outstanding issue for dust optical modeling, and distinguishes it from other aerosol types. The advent of fractal modeling for black carbon (Forrest and Jr, 2001; Sorensen, 2001), which was once widely represented as grape-like structures (Medalia and Rivin, 1982) was a significant breakthrough for representing carbonaceous particles. An analogous innovation has yet to occur for dust (Moosmüller, 2023).

Initial representation of dust in remote sensing and global modeling applications idealized dust particles as spheres whose scattering and absorption properties were calculated using Mie theory (Tegen and Lacis, 1996). (Meng et al., 2010)Implementation of spheroid models for dust has improved space-based remote sensing retrieval products and comparisons between satellite retrievals and global simulations of AOD in the UV-Vis spectral range. However, this substitution hardly changes the hemispheric fluxes calculated by Earth system models (Mishchenko et al., 1997). Significant changes in optical properties and fluxes result when particles are represented as ellipsoids with three distinct dimensions (Kok et al., 2017), but the question of which shape model provides a better representation for dust has not been resolved. Some studies of single particle scattering also indicate the need to account for particle roughness and angularity (Conny et al., 2020; Kalashnikova and Sokolik, 2004), especially for combined multi-angle, multi-spectral remote-sensing retrievals (Kalashnikova and Kahn, 2006). Whether a consideration of these would have a significant effect upon the DRE, and whether the variety in these properties can be expressed parsimoniously remains unresolved.

The lack of realistic dust shape models means that currently there is difficulty in getting closure between forward modeling from particle refractive index, shape, and size and what is observed as optical properties. In Dubovik et al. (2006) the spheroidal shape model was unable to reproduce the spectral dependence of the Amsterdam-Granada measurement of the feldspar scattering matrix. The measured spectral dependence can only be reproduced if, unphysically, different size distributions are assumed at different wavelengths. The current reliance on smooth ellipsoidal shapes by most remote sensing retrieval algorithms and global models is due to the historic lack of exact light-scattering theory for irregular particles, which makes accurate optical modeling for dust extremely challenging. There are limitations in the exact computational methods currently applied to dust optical modeling. However, substantial progress has been made at converging exact and approximate computational methods to accurately calculate single scattering properties of arbitrary non-spherical particles over a wide range of particle size parameters (Yang et al., 2019). This has enabled the development of a recent new database of dust single scattering properties represented by irregular hexahedra (Saito et al., 2021) that are better suited for representing dust backscattering signals. Other possible improvements to dust morphology models have also been proposed by Zubko et al. (2013) by representing dust as agglomerate debris particles.

Although the minimal description of non-spherical features needed to accurately calculate dust optical properties remains unknown, and the sensitivity of global integrated properties like DRE to these features is uncertain, the needed level of complexity should depend on the application. For comparison, the radiative effects of ice clouds are not estimated with the infinite variety of snowflake shapes, but instead a limited number of crystal shapes are prescribed to calculate their collective radiative effect. Closure studies where measured particle properties are used to infer radiative effects that are then compared to independently measured radiative forcing could help elucidate these uncertainties.

The limitations of currently available measurements and retrievals of dust physical properties leave outstanding questions for their representation in global models and remote sensing retrieval algorithms. When particles are transferred from soil to the atmosphere, it is expected that fine particles will preferentially be lifted and stay in the atmosphere for longer periods. However, observations indicate the persistence of coarse and giant particles at higher altitudes and farther downwind of their source than previously expected from global models.(Huang et al., 2020) Given their potential radiative effect in the thermal wavelength range, consequential for global radiative forcing, and the contribution to global distributions of the transport of dust mass, which redistributes essential minerals, it is important that future work focuses on characterizing the life cycle of larger particles and understanding the physical processes that extend their airborne lifetime (Adebiyi et al., 2023). This will require addressing the measurement challenges of large-particle sampling. Cloud probes and open-path aircraft instruments, as well as *in situ* measurements with isokinetic inlets that align with the direction of the flow or the apparent wind, will be essential for measuring a broader size range of dust emission and ambient concentration that can characterize the full life cycle of larger particles.

In models, several issues need to be addressed to understand what vertical transport processes offset the expected settling of larger particles, and contribute to the lack of coarse mode particles sufficiently downwind. Convective mixing driven by heating of the dust layer is one proposed mechanism for maintaining the larger particles within aerosol layers like the SAL (Gasteiger et al., 2017). Another proposed mechanism is increased aerodynamic resistance of non-spherical particles, especially platelike minerals such as phyllosilicates, which would slow particle descent and increase particle lifetime by roughly twenty percent (Huang et al., 2020). Particle settling schemes in models may also be excessively diffusive (Ginoux, 2003). Atmospheric electric fields could also aid particle emission and reduce fall speeds (Toth III et al., 2020; Kok and Renno, 2006) when the particles become charged either through induction at the surface or through particle collisions. However, field measurements also suggest that ambient electric fields orient the longest axis of freshly emitted dust particles along the vertical (Ulanowski et al., 2007), which would minimize the aerodynamic drag of falling particles compared to a collection of random orientations. This mechanism could explain why elongated particles are depleted in deposition measurements of long-range transported dust (Li and Osada, 2007). It has also been posited that a vertical electrical force could potentially compensate for a vertically aligned particle's weight (van der Does et al., 2018). Measurement campaigns are characterizing the relation between dust events and anomalies to the atmospheric field to understand the importance of electromagnetic forces upon dust particle trajectories (Daskalopoulou et al., 2020).

Large particles are most optically thick in the thermal infrared spectral range. However, it has not been demonstrated that Earth system models are grossly underestimating the longwave forcing compared to the shortwave forcing. Although this may be because a commonly used refractive index (Volz 1973) shows larger absorption compared to that measured in an aerosol chamber from a global collection of soil samples (Di Biagio et al., 2017). Sensitivity studies that analyze the impact of large particles on long-wave radiative forcing in models are needed to understand this inconsistency. One aspect that may be overlooked is the model internal parameterization when it comes to radiative forcing. For example, the radiative transfer models embedded within GCMs are not typically designed with aerosol effects in mind. Especially in the longwave, most of the models are neglecting scattering effects by aerosols in their RT calculations.

Due to the indeterminate nature of the remote sensing aerosol retrieval problem, it is not possible to uniquely determine aerosol microphysical properties from current remote sensing observations in sufficient detail, and algorithms employ *a priori* dust models to constrain their solution space. Most remote sensing algorithms base their dust models on AERONET climatology of retrieved size distribution at dust-dominated sites. The AERONET retrieval forces the size distribution to end at 30 μm diameter, assumes simplified dust shapes, and the same indices of refraction for all particle sizes. Thus, relying on AERONET retrieved size distributions may be skewing our understanding of the loading of large particles and the compositions of dust on a routine basis.

More careful analysis of AERONET data and strategic placement of new sites close to dust source regions is needed to account for large particles. Also, synergistic retrievals combining UV-Vis and TIR space-borne remote sensing measurements should be explored as they may provide a way to globally constrain large dust particle loadings (Zheng et al., 2022). However, there is no substitute for direct measurements of *in situ* samples for obtaining detailed particle microphysical and chemical properties.

The heterogeneity in mineral deposits in arid regions leads to significant variability in dust composition, as can be seen in the range of complex refractive index values (particularly in the imaginary component) measured for global samples of bulk dust. The relationship between dust source region and size-resolved composition near-source and after transport requires future investigations (Scheuvens et al., 2013). More accurate datasets on the size-resolved composition will help us to understand the variation of the imaginary refractive index with particle size. For instance, optical measurements have shown that fine dust particles tend to be more absorbing than coarse particles, possibly due to the variation in their composition (Kandler et al., 2007; Rocha-Lima et al., 2018).

Observations and simulations with prognostic dust mineral composition suggest that regional variations are substantial, whereas all the Earth system models surveyed for this paper use globally uniform size invariant refractive index assumptions, whereas some of the remote sensing retrieval algorithms allow for limited refractive index variability through mixing with other modes or optimizing the SSA. These assumptions may lead to regional biases in radiative forcing and retrieved optical properties. Future modeling and retrieval algorithm developments will require different kinds of dust associated with difference source regions and aging processes to capture this variability. However, prognostic dust models will be only as good as their inputs of dust source mineral composition and its regional variations combined with accurate complex refractive index spectra for important minerals. Current measurements of aerosol composition are insufficient to constrain or provide validation of regional variations (e.g. Perlwitz et al., 2015a, Scanza et al., 2015). This limits the attempts to derive local composition and the associated radiative effects from first principles. NASA’s EMIT (Earth Surface Mineral Dust Source Investigation) mission will partly fill this gap in knowledge by providing quantitative measurements of soil composition of iron oxides as well as other minerals that have absorption features in the solar spectral range. However, suborbital measurements that bridge soil properties to what gets lofted will be needed as well, which requires consistent and simultaneous ground based *in situ* soil and aerosol sampling at the source along with column integrated observations (e.g. Panta et al., 2023).

Even with these new constraints on soil minerology, there is nevertheless a lack of understanding of fundamental dust minerology physical properties, even the spectral refractive indices of key minerals like hematite and goethite. Current measurements of hematite refractive index vary widely, which inhibits attempts to calculate dust optical property and forcing variations (Zhang et al., 2015). This is a roadblock for modeling efforts that want to take, for example, the hematite content of a particle and apply a mixing rule and assumptions about morphology to derive radiative forcing (Lafon et al., 2006; e.g., Lee et al., 2020). Continued systematic observations will be needed to resolve these issues and allow more confidence in models and interpretation of remote sensing observations.

Although our ability to represent dust in global circulation models and space-based remote sensing retrieval algorithms has advanced, there is still more work to be done, particularly to consolidate the various approaches. Often in global modeling, radiative forcing, which is integrated over the phase function, or the AOD implied by a mass loading, is the aerosol radiative parameter considered, whereas a satellite retrieval considers the total column aerosol effect on top of the atmosphere radiance from a specific sensor-solar geometry. Our survey of dust optical properties assumed or retrieved by remote sensing retrievals and global circulation models indicates that their representation of dust is often not consistent both within models and retrievals, and between models and retrievals. These large uncertainties should be considered in inter-model comparisons and analysis of simulated dust distributions that are constrained by AOD retrievals, such as long-term trends in mass transport. Moreover, rather than naive comparisons of models to satellite retrievals that may introduce spurious model bias due to mismatch of assumptions between models and retrievals, implementation of observation simulators such as COSP (The CMFIP Observation Simulator Package) (Bodas-Salcedo et al., 2011) will be required in models. Forward modeling in the context of observing system simulation experiments (OSSEs) (Castellanos et al., 2018) can help elucidate these biases and quantify the sensitivities to model and retrieval assumptions.

Next generation missions such as PACE and AOS will provide various active and passive observations with multi-angle, polarization, and broader spectral capabilities opening the opportunity to use observations from various sensors in a synergistic way. This will provide constraints on aerosols beyond single wavelength AOD, such as spectral refractive index and effective radius. Synergistic retrievals will require consistent representation of dust properties across the various instruments.

Both global modeling efforts and remote sensing retrievals require some level of *a priori* constraints for the optical properties of complex natural mixtures of aerosols. However, whereas remote sensing observations characterize the optical properties of the total aerosol amount in the atmosphere from total radiance measurements, global circulation models represent the total aerosol mass burden in the atmosphere by building it up from the balance of individual aerosol sources and sinks. Thus, there is a need for a chain of measurements ranging from characterizing individual dust mineralogy components (e.g., pure hematite and goethite) to *in situ* bulk samples of complex atmospheric aerosol mixtures that can be generalized in a way that both global circulation models and retrieval algorithms can apply them.

This chain of measurements will require developing a comprehensive set of global ground samples (soil taken from source regions) that can be taken back to the laboratory, resuspended, and analyzed (e.g., Engelbrecht et al., 2016). The dust emission process is complex, and the composition of the suspended dust does not necessarily reflect the composition of the parent material. Thus, deposited dust samples in areas downwind and samples that can be analyzed *in situ* from aircraft (e.g., optical properties that are measured with open-path instruments deployed on the wing of an instrument) and at the same time collected to be taken back to the laboratory for additional characterization (e.g., filter samples that undergo chemical and mineralogical analysis) will also be required. An integrated community effort is needed to realize this.

Systematic sampling - the number of samples, range of samples, and how samples are collected - will be crucial in this endeavor. One strategy that has been proposed for “systematic sampling” is to consider the probability distribution of the sampled properties (Kahn et al., 2017). If new observations continue to reproduce the distribution already established, then one can be confident that the variability of that dust property has been captured. This contrasts with the ambient dust property data available now, which originate from a lot of individual samples taken during various field campaigns, and provide no indication as to whether the distributions of properties of interest have been sampled.

This "various single sample" situation is also true for the collections of soil samples that have been analyzed in the laboratory. They have simply been taken from various deserts that are major dust source regions at opportune locations and times. The process of analyzing these samples in the laboratory is to resuspend the soil and sort the suspended particles by size, for example with a $PM_{2.5}$ or $PM_{10}$ sampler, to create a suspended sample that is more representative of long-range transport (e.g., Engelbrecht et al., 2016). One way to determine if these soil samples and their processing is representative enough is to determine if the optics that are measured from such a sample are comparable to what is retrieved at AERONET stations downwind of dust source regions. In general, studies that investigate the consistency between laboratory measurements and observed ambient optical properties are lacking.

It is notable that Mars return samples are forthcoming, and advances in light scattering computational methods, shape modeling, and quantification of mineral optical properties on Earth will all greatly benefit the Mars science community. Dust is a unique problem where terrestrial and planetary scientists can collaborate and share knowledge. Insights gained about the mechanisms for large-particle long range transport on Earth could potentially be applicable to representing Mars planetary scale dust storms in Mars circulation models. In addition, Mars' atmosphere represents a grand laboratory where atmospheric optics is much more dominated by dust aerosols due to lack of other aerosols and clouds, very limited precipitation, low gravity, and reduced gaseous scattering in a much thinner atmosphere. Therefore, this "laboratory" may allow for proof-of-concept dust retrievals without many of the complexities existing in the Earth atmosphere. At the same time, lessons learned in establishing satellite remote sensing capabilities for Earth, beginning with Explorer VII in 1959 (Lewis et al., 2018, 2010) will be invaluable for establishing related capabilities for Mars.

In conclusion, entrained mineral dust particles in the atmosphere are a significant feature of the Earth system, but their representation in remote sensing and global circulation models has significant uncertainties and inconsistencies. The biggest limitation is the lack of detailed, regionally specific, and statistically representative information about the distributions of underlying dust particle microphysical properties – size distribution, morphology, complex index of refraction spectra, internal structure heterogeneity, and the resulting optical properties. Furthermore, there are also limitations in the computational methods that must be applied to dust optical modeling to account for their irregular shape.

## Acknowledgements:

This work was funded by the Science and Exploration Directorate, NASA Goddard Space Flight Center. We thank four reviewers for their insightful comments.

## Author Contributions:

P. Castellanos was responsible for the overall manuscript, contributing to the initial and all subsequent drafts of the manuscript.

P. Colarco was the lead author of Section 5, developed the initial draft of that section, is responsible for all figures and analysis therein, and contributed to the overall editing of the manuscript.

W. R. Espinosa was the lead author of Section 3, developed the initial draft of that section, and contributed to the overall editing of the manuscript.

S. Guzewich was the lead author of Section 6, developed the initial draft of that section, and contributed to the overall editing of the manuscript.

R. Levy was the lead author of Section 4, developed the initial draft of that section, is responsible for all figures an analysis therein, and contributed to the overall editing of the manuscript.

R. Miller was the lead author of Section 2, developed the initial draft of that section, is responsible for figures and analysis therein, and contributed to the overall content and editing of the manuscript.

E. Nowottnick and J. Yorks developed the initial draft of the review of lidar technology and provided the tables of lidar ratio assumptions.

R. Kahn was a co-author of Sections 3 and 4 and contributed to the overall content and editing of the manuscript.

A. Rocha-Lima contributed to the overall content and editing of the manuscript as well as providing the dust imagery in Section 2.

M. Chin, Hans Moosmüller, O. Kemppinen, M. Smith, and H. Yu contributed to the overall content, analysis, and editing of the manuscript.

# 9 References

Abouchami, W., Näthe, K., Kumar, A., Galer, S.J.G., Jochum, K.P., Williams, E., Horbe, A.M.C., Rosa, J.W.C., Balsam, W., Adams, D., Mezger, K., Andreae, M.O., 2013. Geochemical and isotopic characterization of the Bodélé Depression dust source and implications for transatlantic dust transport to the Amazon Basin. Earth Planet Sc Lett 380, 112–123. https://doi.org/10.1016/j.epsl.2013.08.028

Adebiyi, A., Kok, J.F., Murray, B.J., Ryder, C.L., Stuut, J.-B.W., Kahn, R.A., Knippertz, P., Formenti, P., Mahowald, N.M., García-Pando, C.P., Klose, M., Ansmann, A., Samset, B.H., Ito, A., Balkanski, Y., Di Biagio, C., Romanias, M.N., Huang, Y., Meng, J., 2023. A review of coarse mineral dust in the Earth system. Aeolian Res 60, 100849. https://doi.org/10.1016/j.aeolia.2022.100849

Adebiyi, A.A., Kok, J.F., 2020. Climate models miss most of the coarse dust in the atmosphere. Sci Adv 6, eaaz9507. https://doi.org/10.1126/sciadv.aaz9507

Alfaro, S., Gaudichet, A., GOMES, L., Maille, M., 1998. Mineral aerosol production by wind erosion: aerosol particle sizes and binding energies. Geophysical Research Letters 25, 991 994.

Alfaro, S.C., Gomes, L., 2001. Modeling mineral aerosol production by wind erosion: Emission intensities and aerosol size distributions in source areas. J Geophys Res Atmospheres 106, 18075–18084. https://doi.org/10.1029/2000jd900339

Atkinson, J.D., Murray, B.J., Woodhouse, M.T., Whale, T.F., Baustian, K.J., Carslaw, K.S., Dobbie, S., O'Sullivan, D., Malkin, T.L., 2013. The importance of feldspar for ice nucleation by mineral dust in mixed-phase clouds. Nature 498, 355–358. https://doi.org/10.1038/nature12278

Balkanski, Y., Schulz, M., Claquin, T., Guibert, S., 2007. Reevaluation of Mineral aerosol radiative forcings suggests a better agreement with satellite and AERONET data. Atmos Chem Phys 7, 81–95. https://doi.org/10.5194/acp-7-81-2007

Barahona, D., Molod, A., Bacmeister, J., Nenes, A., Gettelman, A., Morrison, H., Phillips, V., Eichmann, A., 2014. Development of two-moment cloud microphysics for liquid and ice within the NASA Goddard Earth Observing System Model (GEOS-5). Geosci Model Dev 7, 1733 1766. https://doi.org/10.5194/gmd-7-1733-2014

Barkey, B., Liou, K.N., 2001. Polar nephelometer for light-scattering measurements of ice crystals. Opt Lett 26, 232. https://doi.org/10.1364/ol.26.000232

Basu, S., Richardson, M.I., Wilson, R.J., 2004. Simulation of the Martian dust cycle with the GFDL Mars GCM. J Geophys Res Planets 1991 2012 109. https://doi.org/10.1029/2004je002243

Basu, S., Wilson, J., Richardson, M., Ingersoll, A., 2006. Simulation of spontaneous and variable global dust storms with the GFDL Mars GCM. J Geophys Res Planets 1991 2012 111. https://doi.org/10.1029/2005je002660

Bauer, S.E., Koch, D., 2005. Impact of heterogeneous sulfate formation at mineral dust surfaces on aerosol loads and radiative forcing in the Goddard Institute for Space Studies general circulation model. J Geophys Res Atmospheres 1984 2012 110. https://doi.org/10.1029/2005jd005870

Bauer, S.E., Wright, D.L., Koch, D., Lewis, E.R., McGraw, R., Chang, L.-S., Schwartz, S.E., Ruedy, R., 2008. MATRIX (Multiconfiguration Aerosol TRacker of mIXing state): an aerosol microphysical module for global atmospheric models. Atmos Chem Phys 8, 6003–6035. https://doi.org/10.5194/acp-8-6003-2008

Bedidi, A., Cervelle, B., 1993. Light scattering by spherical particles with hematite and goethitelike optical properties: Effect of water impregnation. J Geophys Res Solid Earth 98, 11941–11952. https://doi.org/10.1029/93jb00188

Benedetti, A., Reid, J.S., KNIPPERTZ, P., Marsham, J.H., Giuseppe, F.D., Remy, S., Basart, S., Boucher, O., Brooks, I.M., Menut, L., Mona, L., Laj, P., Pappalardo, G., Wiedensohler, A., Baklanov, A., Brooks, M., Colarco, P.R., Cuevas, E., Silva, A.D., Escribano, J., Flemming, J., Huneeus, N., Jorba, O., Kazadzis, S., Kinne, S., Popp, T., Quinn, P.K., Sekiyama, T.T., Tanaka, T., Terradellas, E., 2018. Status and future of numerical atmospheric aerosol prediction with a focus on data requirements. Atmos Chem Phys 18, 10615 10643. https://doi.org/10.5194/acp-18-10615-2018

Berger, J.A., Schmidt, M.E., Gellert, R., Campbell, J.L., King, P.L., Flemming, R.L., Ming, D.W., Clark, B.C., Pradler, I., VanBommel, S.J.V., Minitti, M.E., Fairén, A.G., Boyd, N.I., Thompson, L.M., Perrett, G.M., Elliott, B.E., Desouza, E., 2016. A global Mars dust composition refined by the Alpha-Particle X-ray Spectrometer in Gale Crater. Geophys Res Lett 43, 67–75. https://doi.org/10.1002/2015gl066675

Bi, L., Lin, W., Liu, D., Zhang, K., 2018. Assessing the depolarization capabilities of nonspherical particles in a super-ellipsoidal shape space. Opt. express 26, 1726–1742. https://doi.org/10.1364/oe.26.001726

Bi, L., Wang, Z., Han, W., Li, W., Zhang, X., 2022. Computation of Optical Properties of Core-Shell Super-Spheroids Using a GPU Implementation of the Invariant Imbedding T-Matrix Method. Front. Remote Sens. 3, 903312. https://doi.org/10.3389/frsen.2022.903312

Bi, L., Yang, P., 2014. Accurate simulation of the optical properties of atmospheric ice crystals with the invariant imbedding T-matrix method. J. Quant. Spectrosc. Radiat. Transf. 138, 17–35. https://doi.org/10.1016/j.jqsrt.2014.01.013

Bi, L., Yang, P., Kattawar, G.W., Hu, Y., Baum, B.A., 2011. Scattering and absorption of light by ice particles: Solution by a new physical-geometric optics hybrid method. J Quantitative Spectrosc Radiat Transf 112, 1492–1508. https://doi.org/10.1016/j.jqsrt.2011.02.015

Bi, L., Yang, P., Kattawar, G.W., Kahn, R., 2010. Modeling optical properties of mineral aerosol particles by using nonsymmetric hexahedra. Appl Optics 49, 334. https://doi.org/10.1364/ao.49.000334

Bi, L., Yang, P., Kattawar, G.W., Kahn, R., 2009. Single-scattering properties of triaxial ellipsoidal particles for a size parameter range from the Rayleigh to geometric-optics regimes. Appl Optics 48, 114. https://doi.org/10.1364/ao.48.000114

Bi, L., Yang, P., Kattawar, G.W., Mishchenko, M.I., 2013. Efficient implementation of the invariant imbedding T-matrix method and the separation of variables method applied to large nonspherical inhomogeneous particles. J Quantitative Spectrosc Radiat Transf 116, 169–183. https://doi.org/10.1016/j.jqsrt.2012.11.014

Bian, Y., Xu, W., Hu, Y., Tao, J., Kuang, Y., Zhao, C., 2020. Method to retrieve aerosol extinction profiles and aerosol scattering phase functions with a modified CCD laser atmospheric detection system. Opt Express 28, 6631. https://doi.org/10.1364/oe.386214

Bian, Y., Zhao, C., Xu, W., Zhao, G., Tao, J., Kuang, Y., 2017. Development and validation of a CCD-laser aerosol detective system for measuring the ambient aerosol phase function. Atmos Meas Tech 10, 2313–2322. https://doi.org/10.5194/amt-10-2313-2017

Bodas-Salcedo, A., Webb, M.J., Bony, S., Chepfer, H., Dufresne, J.-L., Klein, S.A., Zhang, Y., Marchand, R., Haynes, J.M., Pincus, R., John, V.O., 2011. COSP: Satellite simulation software for model assessment. B Am Meteorol Soc 92, 1023–1043. https://doi.org/10.1175/2011bams2856.1

Bohren, C.F., Huffman, D.R., 1998. Absorption and Scattering of Light by Small Particles. John Wiley & Sons. https://doi.org/10.1002/9783527618156

Braun, S.A., Yorks, J., Thorsen, T., Cecil, D., Kirschbaum, D., 2022. NASA’S Earth System Observatory-Atmosphere Observing System. Igarss 2022 - 2022 Ieee Int Geoscience Remote Sens Symposium 00, 7391–7393. https://doi.org/10.1109/igarss46834.2022.9884029

Bruggeman, D.A.G., 1935. Berechnung verschiedener physikalischer Konstanten von heterogenen Substanzen. I. Dielektrizitätskonstanten und Leitfähigkeiten der Mischkörper aus isotropen Substanzen. Annalen Der Physik 416, 636–664. https://doi.org/10.1002/andp.19354160705

Bullard, R.L., Kuang, C., Uin, J., Smith, S., Springston, S.R., 2017. Aerosol Inlet Characterization Experiment Report.

Burton, S.P., Ferrare, R.A., Hostetler, C.A., Hair, J.W., Rogers, R.R., Obland, M.D., Butler, C.F., Cook, A.L., Harper, D.B., Froyd, K.D., 2012. Aerosol classification using airborne High Spectral Resolution Lidar measurements – methodology and examples. Atmos Meas Tech 5, 73–98. https://doi.org/10.5194/amt-5-73-2012

Buseck, P.R., Jacob, D.J., Pósfai, M., Li, J., Anderson, J.R., 2000. Minerals in the Air: An Environmental Perspective. Int Geol Rev 42, 577–593. https://doi.org/10.1080/00206810009465101

Butt, M.J., Mashat, A.S., 2018. MODIS satellite data evaluation for sand and dust storm monitoring in Saudi Arabia. Int J Remote Sens 39, 1–19. https://doi.org/10.1080/01431161.2018.1488293

Cakmur, R.V., Miller, R.L., Perlwitz, J., Geogdzhayev, I.V., Ginoux, P., Koch, D., Kohfeld, K.E., Tegen, I., Zender, C.S., 2006. Constraining the magnitude of the global dust cycle by minimizing the difference between a model and observations. J Geophys Res Atmospheres 1984 2012 111. https://doi.org/10.1029/2005jd005791

Caquineau, S., Gaudichet, A., Gomes, L., Legrand, M., 2002. Mineralogy of Saharan dust transported over northwestern tropical Atlantic Ocean in relation to source regions. J Geophys Res Atmospheres 1984 2012 107, AAC 4-1-AAC 4-12. https://doi.org/10.1029/2000jd000247

Carlson, T.N., 1979. Atmospheric Turbidity in Saharan Dust Outbreaks as Determined by Analyses of Satellite Brightness Data. Mon Weather Rev 107, 322–335. https://doi.org/10.1175/1520-0493(1979)107<;0322:atisdo>2.0.co;2

Carlson, T.N., Prospero, J.M., 1972. The Large-Scale Movement of Saharan Air Outbreaks over the Northern Equatorial Atlantic. J Appl Meteorol 11, 283–297. https://doi.org/10.1175/1520-0450(1972)011<;0283:tlsmos>2.0.co;2

Castagner, J.-L., Bigio, I.J., 2006. Polar nephelometer based on a rotational confocal imaging setup. Appl Optics 45, 2232. https://doi.org/10.1364/ao.45.002232

Castellanos, P., Silva, A.M. da, Darmenov, A.S., Buchard, V., Govindaraju, R.C., Ciren, P., Kondragunta, S., 2018. A Geostationary Instrument Simulator for Aerosol Observing System Simulation Experiments. Atmosphere-basel 10, 2. https://doi.org/10.3390/atmos10010002

Checa-Garcia, R., Balkanski, Y., Albani, S., Bergman, T., Carslaw, K., Cozic, A., Dearden, C., Marticorena, B., Michou, M., Noije, T. van, Nabat, P., O'Connor, F.M., Olivié, D., Prospero, J.M., Sager, P.L., Schulz, M., Scott, C., 2021. Evaluation of natural aerosols in CRESCENDO Earth system models (ESMs): mineral dust. Atmos Chem Phys 21, 10295–10335. https://doi.org/10.5194/acp-21-10295-2021

Chen, G., Yang, P., Kattawar, G.W., 2008. Application of the pseudospectral time-domain method to the scattering of light by nonspherical particles. J Opt Soc Am 25, 785. https://doi.org/10.1364/josaa.25.000785

Chowdhary, J., Zhai, P.-W., Boss, E., Dierssen, H., Frouin, R., Ibrahim, A., Lee, Z., Remer, L.A., Twardowski, M., Xu, F., Zhang, X., Ottaviani, M., Espinosa, W.R., Ramon, D., 2019. Modeling Atmosphere-Ocean Radiative Transfer: A PACE Mission Perspective. Frontiers Earth Sci 7, 100. https://doi.org/10.3389/feart.2019.00100

Chylek, P., Wong, J., 1995. Effect of absorbing aerosols on global radiation budget. Geophys Res Lett 22, 929–931. https://doi.org/10.1029/95gl00800

Clancy, R.T., Wolff, M.J., Whitney, B.A., Cantor, B.A., Smith, M.D., McConnochie, T.H., 2010. Extension of atmospheric dust loading to high altitudes during the 2001 Mars dust storm: MGS TES limb observations. Icarus 207, 98–109. https://doi.org/10.1016/j.icarus.2009.10.011

Claquin, T., Schulz, M., Balkanski, Y.J., 1999. Modeling the mineralogy of atmospheric dust sources. J Geophys Res Atmospheres 1984 2012 104, 22243–22256. https://doi.org/10.1029/1999jd900416

Colarco, P., Toon, O., Holben, B., 2003. Saharan dust transport to the Caribbean during PRIDE: 1. Influence of dust sources and removal mechanisms on the timing and magnitude of downwind aerosol optical depth events from simulations of in situ and remote sensing observations. J Geophys Res Atmospheres 1984 2012 108. https://doi.org/10.1029/2002jd002658

Colarco, P.R., Nowottnick, E.P., Randles, C.A., Yi, B., Yang, P., Kim, K., Smith, J.A., Bardeen, C.G., 2014. Impact of radiatively interactive dust aerosols in the NASA GEOS-5 climate model: Sensitivity to dust particle shape and refractive index. J Geophys Res Atmospheres 119, 753–786. https://doi.org/10.1002/2013jd020046

Colarco, P.R., Toon, O.B., Torres, O., Rasch, P.J., 2002. Determining the UV imaginary index of refraction of Saharan dust particles from Total Ozone Mapping Spectrometer data using a three-dimensional model of dust transport. J Geophys Res Atmospheres 1984 2012 107, AAC 4-1-AAC 4-18. https://doi.org/10.1029/2001jd000903

Conny, J.M., Willis, R.D., Ortiz-Montalvo, D.L., 2020. Optical Modeling of Single Asian Dust and Marine Air Particles: A Comparison with Geometric Particle Shapes for Remote Sensing. J Quantitative Spectrosc Radiat Transf 254, 107197. https://doi.org/10.1016/j.jqsrt.2020.107197

Croft, B., Lohmann, U., Martin, R.V., Stier, P., Wurzler, S., Feichter, J., Hoose, C., Heikkilä, U., Donkelaar, A. van, Ferrachat, S., 2010. Influences of in-cloud aerosol scavenging parameterizations on aerosol concentrations and wet deposition in ECHAM5-HAM. Atmos Chem Phys 10, 1511–1543. https://doi.org/10.5194/acp-10-1511-2010

Curtis, D.B., Aycibin, M., Young, M.A., Grassian, V.H., Kleiber, P.D., 2007. Simultaneous measurement of light-scattering properties and particle size distribution for aerosols: Application to ammonium sulfate and quartz aerosol particles. Atmos Environ 41, 4748–4758. https://doi.org/10.1016/j.atmosenv.2007.03.020

d'Almeida, G.A., Schütz, L., 1983. Number, Mass and Volume Distributions of Mineral Aerosol and Soils of the Sahara. J Clim Appl Meteorol 22, 233–243. https://doi.org/10.1175/1520-0450(1983)022<;0233:nmavdo>2.0.co;2

Daskalopoulou, V., Mallios, S.A., Ulanowski, Z., Hloupis, G., Gialitaki, A., Tsikoudi, I., Tassis, K., Amiridis, V., 2020. The electrical activity of Saharan dust as perceived from surface electric field observations. Atmos Chem Phys 21, 927–949. https://doi.org/10.5194/acp-21-927-2021

Dave, J.V., 1978. Effect of Aerosols on the Estimation of Total Ozone in an Atmospheric Column from the Measurements of Its Ultraviolet Radiance. J Atmos Sci 35, 899–911. https://doi.org/10.1175/1520-0469(1978)035<;0899:eoaote>2.0.co;2

DeMott, P.J., Sassen, K., Poellot, M.R., Baumgardner, D., Rogers, D.C., Brooks, S.D., Prenni, A.J., Kreidenweis, S.M., 2003. African dust aerosols as atmospheric ice nuclei. Geophys Res Lett 30. https://doi.org/10.1029/2003gl017410

Dentener, F.J., Carmichael, G.R., Zhang, Y., Lelieveld, J., Crutzen, P.J., 1996. Role of mineral aerosol as a reactive surface in the global troposphere. J Geophys Res Atmospheres 101, 22869–22889. https://doi.org/10.1029/96jd01818

Di Biagio, C., Balkanski, Y., Albani, S., Boucher, O., Formenti, P., 2020. Direct Radiative Effect by Mineral Dust Aerosols Constrained by New Microphysical and Spectral Optical Data. Geophys Res Lett 47. https://doi.org/10.1029/2019gl086186

Di Biagio, C., Boucher, H., Caquineau, S., Chevaillier, S., Cuesta, J., Formenti, P., 2014. Variability of the infrared complex refractive index of African mineral dust: experimental estimation and implications for radiative transfer and satellite remote sensing. https://doi.org/10.5194/acpd-14-10597-2014

Di Biagio, C., Formenti, P., Balkanski, Y., Caponi, L., Cazaunau, M., Pangui, E., Journet, E., Nowak, S., Andreae, M.O., Kandler, K., Saeed, T., Piketh, S., Seibert, D., Williams, E., Doussin, J.-F., 2019. Complex refractive indices and single-scattering albedo of global dust aerosols in the shortwave spectrum and relationship to size and iron content. Atmos Chem Phys 19, 15503–15531. https://doi.org/10.5194/acp-19-15503-2019

Di Biagio, C., Formenti, P., Balkanski, Y., Caponi, L., Cazaunau, M., Pangui, E., Journet, E., Nowak, S., Caquineau, S., Andreae, M.O., Kandler, K., Saeed, T., Piketh, S., Seibert, D., Williams, E., Doussin, J.-F., 2017. Global scale variability of the mineral dust long-wave refractive index: a new dataset of in situ measurements for climate modeling and remote sensing. Atmos Chem Phys 17, 1901–1929. https://doi.org/10.5194/acp-17-1901-2017

Diner, D.J., Beckert, J.C., Reilly, T.H., Bruegge, C.J., Conel, J.E., Kahn, R.A., Martonchik, J.V., Ackerman, T.P., Davies, R., Gerstl, S.A.W., Gordon, H.R., Muller, J.-P., Myneni, R.B., Sellers, P.J., Pinty, B., Verstraete, M.M., 1998. Multi-angle Imaging SpectroRadiometer (MISR) instrument description and experiment overview. Ieee T Geosci Remote 36, 1072–1087. https://doi.org/10.1109/36.700992

Does, M. van der, Brummer, G.A., Crimpen, F.C.J., Korte, L.F., Mahowald, N.M., Merkel, U., Yu, H., Zuidema, P., Stuut, J.W., 2020. Tropical Rains Controlling Deposition of Saharan Dust Across the North Atlantic Ocean. Geophys Res Lett 47. https://doi.org/10.1029/2019gl086867

Does, M. van der, Knippertz, P., Zschenderlein, P., Harrison, R.G., Stuut, J.-B.W., 2018. The mysterious long-range transport of giant mineral dust particles. Sci Adv 4, eaau2768. https://doi.org/10.1126/sciadv.aau2768

Does, M. van der, Korte, L.F., Munday, C.I., Brummer, G.-J.A., Stuut, J.-B.W., 2016. Particle size traces modern Saharan dust transport and deposition across the equatorial North Atlantic. Atmos Chem Phys 16, 13697–13710. https://doi.org/10.5194/acp-16-13697-2016

Dolgos, G., Martins, J.V., 2014. Polarized Imaging Nephelometer for in situ airborne measurements of aerosol light scattering. Opt Express 22, 21972. https://doi.org/10.1364/oe.22.021972

Draine, B.T., Flatau, P.J., 1994. Discrete-Dipole Approximation For Scattering Calculations. J Opt Soc Am 11, 1491. https://doi.org/10.1364/josaa.11.001491

Dubovik, O., Herman, M., Holdak, A., Lapyonok, T., Tanré, D., Deuzé, J.L., Ducos, F., Sinyuk, A., Lopatin, A., 2011. Statistically optimized inversion algorithm for enhanced retrieval of aerosol properties from spectral multi-angle polarimetric satellite observations. Atmos Meas Tech 4, 975–1018. https://doi.org/10.5194/amt-4-975-2011

Dubovik, O., Holben, B., Eck, T.F., Smirnov, A., Kaufman, Y.J., King, M.D., Tanré, D., Slutsker, I., 2002. Variability of Absorption and Optical Properties of Key Aerosol Types Observed in Worldwide Locations. J Atmos Sci 59, 590–608. https://doi.org/10.1175/1520-0469(2002)059<;0590:voaaop>2.0.co;2

Dubovik, O., King, M.D., 2000. A flexible inversion algorithm for retrieval of aerosol optical properties from Sun and sky radiance measurements. J Geophys Res Atmospheres 105, 20673–20696. https://doi.org/10.1029/2000jd900282

Dubovik, O., Sinyuk, A., Lapyonok, T., Holben, B.N., Mishchenko, M., Yang, P., Eck, T.F., Volten, H., Muñoz, O., Veihelmann, B., Zande, W.J. van der, Leon, J., Sorokin, M., Slutsker, I., 2006. Application of spheroid models to account for aerosol particle nonsphericity in remote sensing of desert dust. J Geophys Res Atmospheres 1984 2012 111. https://doi.org/10.1029/2005jd006619

Dupont, S., Rajot, J. -L., Labiadh, M., Bergametti, G., Lamaud, E., Irvine, M.R., Alfaro, S.C., Bouet, C., Fernandes, R., Khalfallah, B., Marticorena, B., Bonnefond, J.M., Chevaillier, S., Garrigou, D., Henry-des-Tureaux, T., Sekrafi, S., Zapf, P., 2019. Dissimilarity Between Dust, Heat, and Momentum Turbulent Transports During Aeolian Soil Erosion. J Geophys Res Atmospheres 124, 1064–1089. https://doi.org/10.1029/2018jd029048

Engelbrecht, J.P., Moosmüller, H., Pincock, S., Jayanty, R.K.M., Lersch, T., Casuccio, G., 2016. Technical note: Mineralogical, chemical, morphological, and optical interrelationships of mineral dust re-suspensions. Atmos Chem Phys 16, 10809–10830. https://doi.org/10.5194/acp-16-10809-2016

Espinosa, W.R., Martins, J.V., Remer, L.A., Puthukkudy, A., Orozco, D., Dolgos, G., 2018. In situ measurements of angular-dependent light scattering by aerosols over the contiguous United States. Atmos Chem Phys 18, 3737–3754. https://doi.org/10.5194/acp-18-3737-2018

Farley, K.A., Williford, K.H., Stack, K.M., Bhartia, R., Chen, A., Torre, M. de la, Hand, K., Goreva, Y., Herd, C.D.K., Hueso, R., Liu, Y., Maki, J.N., Martinez, G., Moeller, R.C., Nelessen, A., Newman, C.E., Nunes, D., Ponce, A., Spanovich, N., Willis, P.A., Beegle, L.W., Bell, J.F., Brown, A.J., Hamran, S.-E., Hurowitz, J.A., Maurice, S., Paige, D.A., Rodriguez-Manfredi, J.A., Schulte, M., Wiens, R.C., 2020. Mars 2020 Mission Overview. Space Sci Rev 216, 142. https://doi.org/10.1007/s11214-020-00762-y

Fedorova, A.A., Korablev, O.I., Bertaux, J.-L., Rodin, A.V., Montmessin, F., Belyaev, D.A., Reberac, A., 2009. Solar infrared occultation observations by SPICAM experiment on Mars-Express: Simultaneous measurements of the vertical distributions of H2O, CO2 and aerosol. Icarus 200, 96–117. https://doi.org/10.1016/j.icarus.2008.11.006

Forget, F., Hourdin, F., Fournier, R., Hourdin, C., Talagrand, O., Collins, M., Lewis, S.R., Read, P.L., Huot, J., 1999. Improved general circulation models of the Martian atmosphere from the surface to above 80 km. J Geophys Res Planets 104, 24155–24175. https://doi.org/10.1029/1999je001025

Formenti, P., Schütz, L., Balkanski, Y., Desboeufs, K., Ebert, M., Kandler, K., Petzold, A., Scheuvens, D., Weinbruch, S., Zhang, D., 2011. Recent progress in understanding physical and chemical properties of African and Asian mineral dust. Atmos. Chem. Phys. 11, 8231–8256. https://doi.org/10.5194/acp-11-8231-2011

Forrest, S.R., Jr, T.A.W., 2001. Long-range correlations in smoke-particle aggregates. J Phys Math Gen 12, L109. https://doi.org/10.1088/0305-4470/12/5/008

Fouquart, Y., Bonnel, B., Brogniez, G., Buriez, J.C., Smith, L., Morcrette, J.J., Cerf, A., 1987. Observations of Saharan Aerosols: Results of ECLATS Field Experiment. Part II: Broadband Radiative Characteristics of the Aerosols and Vertical Radiative Flux Divergence. J Clim Appl Meteorol 26, 38–52. https://doi.org/10.1175/1520-0450(1987)026<;0038:oosaro>2.0.co;2

Fratini, G., Ciccioli, P., Febo, A., Forgione, A., Valentini, R., 2007. Size-segregated fluxes of mineral dust from a desert area of northern China by eddy covariance. Atmos Chem Phys 7, 2839–2854. https://doi.org/10.5194/acp-7-2839-2007

Garnett, J.C.M., 1904. XII. Colours in metal glasses and in metallic films. Philosophical Transactions Royal Soc Lond Ser Contain Pap Math Or Phys Character 203, 385–420. https://doi.org/10.1098/rsta.1904.0024

Gassó, S., Grassian, V.H., Miller, R.L., 2010. Interactions between Mineral Dust, Climate, and Ocean Ecosystems. Elements 6, 247–252. https://doi.org/10.2113/gselements.6.4.247

Gasteiger, J., Groß, S., Sauer, D., Haarig, M., Ansmann, A., Weinzierl, B., 2017. Particle settling and vertical mixing in the Saharan Air Layer as seen from an integrated model, lidar, and in situ perspective. Atmos Chem Phys 17, 297–311. https://doi.org/10.5194/acp-17-297-2017

Gasteiger, J., Wiegner, M., Groß, S., Freudenthaler, V., Toledano, C., Tesche, M., Kandler, K., 2011. Modelling lidar-relevant optical properties of complex mineral dust aerosols. Tellus B 63, 725–741. https://doi.org/10.1111/j.1600-0889.2011.00559.x

Genthon, C., 1992. Simulations of desert dust and sea-salt aerosols in Antarctica with a general circulation model of the atmosphere. Tellus B 44, 371–389. https://doi.org/10.1034/j.1600-0889.1992.00014.x

Gillette, D.A., 1974. On the production of soil wind erosion aerosols having the potential for long range transport. Journal de Recherches Atmospheriques 8, 735–744.

Gillette, D.A., Blifford, I.H., Fryrear, D.W., 1974. The influence of wind velocity on the size distributions of aerosols generated by the wind erosion of soils. J Geophys Res 79, 4068–4075. https://doi.org/10.1029/jc079i027p04068

Gillette, D.A., Jr., I.H.B., Fenster, C.R., 1972. Measurements of Aerosol Size Distributions and Vertical Fluxes of Aerosols on Land Subject to Wind Erosion. J Appl Meteorol 11, 977–987. https://doi.org/10.1175/1520-0450(1972)011<;0977:moasda>2.0.co;2

Gillette, D.A., Passi, R., 1988. Modeling dust emission caused by wind erosion. J Geophys Res Atmospheres 93, 14233–14242. https://doi.org/10.1029/jd093id11p14233

Gillies, J.A., 2013. Treatise on Geomorphology. Aeolian Process 43–63. https://doi.org/10.1016/b978-0-12-374739-6.00297-9

Ginoux, P., 2003. Effects of nonsphericity on mineral dust modeling. J Geophys Res Atmospheres 1984 2012 108, 4052. https://doi.org/10.1029/2002jd002516

Ginoux, P., Chin, M., Tegen, I., Prospero, J., Holben, B., Dubovik, O., Lin, S., 2001. Sources and distributions of dust aerosols simulated with the GOCART model. Journal Of Geophysical Research-Atmospheres 106, 20255 20273.

Ginoux, P., Prospero, J.M., Gill, T.E., Hsu, N.C., Zhao, M., 2012. Global-scale attribution of anthropogenic and natural dust sources and their emission rates based on MODIS Deep Blue aerosol products. Rev Geophys 50. https://doi.org/10.1029/2012rg000388

Ginoux, P., Torres, O., 2003. Empirical TOMS index for dust aerosol: Applications to model validation and source characterization. J Geophys Res Atmospheres 1984 2012 108. https://doi.org/10.1029/2003jd003470

González-Flórez, C., Klose, M., Alastuey, A., Dupont, S., Escribano, J., Etyemezian, V., Gonzalez-Romero, A., Huang, Y., Kandler, K., Nikolich, G., Panta, A., Querol, X., Reche, C., Yus-Díez, J., García-Pando, C.P., 2022. Insights into the size-resolved dust emission from field measurements in the Moroccan Sahara. Atmospheric Chem Phys Discuss 2022, 1–65. https://doi.org/10.5194/acp-2022-758

Green, R.O., Thompson, D.R., 2020. An Earth Science Imaging Spectroscopy Mission: The Earth Surface Mineral Dust Source Investigation (EMIT). Igarss 2020 - 2020 Ieee Int Geoscience Remote Sens Symposium 00, 6262–6265. https://doi.org/10.1109/igarss39084.2020.9323741

Grini, A., Zender, C.S., Colarco, P.R., 2002. Saltation Sandblasting behavior during mineral dust aerosol production. Geophys Res Lett 29, 15-1-15–4. https://doi.org/10.1029/2002gl015248

Gustafson, B.Å.S., 1996. Microwave analog to light scattering measurements: A modern implementation of a proven method to achieve precise control. J Quantitative Spectrosc Radiat Transf 55, 663–672. https://doi.org/10.1016/0022-4073(96)00009-x

Guzewich, S.D., Smith, M.D., Wolff, M.J., 2014. The vertical distribution of Martian aerosol particle size. J Geophys Res Planets 119, 2694–2708. https://doi.org/10.1002/2014je004704

Haberle, R.M., Kahre, M.A., Hollingsworth, J.L., Montmessin, F., Wilson, R.J., Urata, R.A., Brecht, A.S., Wolff, M.J., Kling, A.M., Schaeffer, J.R., 2019. Documentation of the NASA/Ames Legacy Mars Global Climate Model: Simulations of the present seasonal water cycle. Icarus 333, 130–164. https://doi.org/10.1016/j.icarus.2019.03.026

Hair, J.W., Hostetler, C.A., Cook, A.L., Harper, D.B., Ferrare, R.A., Mack, T.L., Welch, W., Izquierdo, L.R., Hovis, F.E., 2008. Airborne High Spectral Resolution Lidar for profiling aerosol optical properties. Appl Optics 47, 6734. https://doi.org/10.1364/ao.47.006734

Hamilton, V.E., McSween, H.Y., Hapke, B., 2005. Mineralogy of Martian atmospheric dust inferred from thermal infrared spectra of aerosols. J Geophys Res Planets 1991 2012 110. https://doi.org/10.1029/2005je002501

Hand, J.L., Mahowald, N.M., Chen, Y., Siefert, R.L., Luo, C., Subramaniam, A., Fung, I., 2004. Estimates of atmospheric-processed soluble iron from observations and a global mineral aerosol model: Biogeochemical implications. J Geophys Res Atmospheres 1984 2012 109. https://doi.org/10.1029/2004jd004574

Herman, J.R., Bhartia, P.K., Torres, O., Hsu, C., Seftor, C., Celarier, E., 1997. Global distribution of UV-absorbing aerosols from Nimbus 7/TOMS data. J Geophys Res Atmospheres 102, 16911–16922. https://doi.org/10.1029/96jd03680

Hess, M., Koepke, P., Schult, I., 1998. Optical Properties of Aerosols and Clouds: The Software Package OPAC. B Am Meteorol Soc 79, 831–844. https://doi.org/10.1175/1520-0477(1998)079<;0831:opoaac>2.0.co;2

Hillger, D., Kopp, T., Lee, T., Lindsey, D., Seaman, C., Miller, S., Solbrig, J., Kidder, S., Bachmeier, S., Jasmin, T., Rink, T., 2013. First-Light Imagery from Suomi NPP VIIRS. B Am Meteorol Soc 94, 1019–1029. https://doi.org/10.1175/bams-d-12-00097.1

Holben, B.N., Eck, T.F., Slutsker, I., Tanré, D., Buis, J.P., Setzer, A., Vermote, E., Reagan, J.A., Kaufman, Y.J., Nakajima, T., Lavenu, F., Jankowiak, I., Smirnov, A., 1998. AERONET—A Federated Instrument Network and Data Archive for Aerosol Characterization. Remote Sens Environ 66, 1–16. https://doi.org/10.1016/s0034-4257(98)00031-5

Horvath, H., Arboledas, L.A., Reyes, F.J.O., 2018. Angular scattering of the Sahara dust aerosol. Atmos Chem Phys 18, 17735–17744. https://doi.org/10.5194/acp-18-17735-2018

Hsu, N.C., Jeong, M.-J., Bettenhausen, C., Sayer, A.M., Hansell, R., Seftor, C.S., Huang, J., Tsay, S.-C., 2013. Enhanced Deep Blue aerosol retrieval algorithm: The second generation. J Geophys Res Atmospheres 118, 9296–9315. https://doi.org/10.1002/jgrd.50712

Hsu, N.C., Lee, J., Sayer, A.M., Kim, W., Bettenhausen, C., Tsay, S. -C., 2019. VIIRS Deep Blue Aerosol Products Over Land: Extending the EOS Long-Term Aerosol Data Records. J Geophys Res Atmospheres 124, 4026–4053. https://doi.org/10.1029/2018jd029688

Hsu, N.C., Tsay, S.-C., King, M.D., Herman, J.R., 2004. Aerosol Properties Over Bright-Reflecting Source Regions. Ieee T Geosci Remote 42, 557–569. https://doi.org/10.1109/tgrs.2004.824067

Hu, S., Gao, T., Li, H., Liu, L., Chen, M., Yang, B., 2018. Light-scattering model for aerosol particles with irregular shapes and inhomogeneous compositions using a parallelized pseudo-spectral time-domain technique. Chinese Phys B 27, 054215. https://doi.org/10.1088/1674-1056/27/5/054215

Hu, S., Liu, L., Gao, T., Zeng, Q., Liu, X., 2020. An efficient implementation of the light scattering simulation for random-oriented non-rotationally symmetric particles using invariant imbedding T-matrix method. J Quantitative Spectrosc Radiat Transf 241, 106734. https://doi.org/10.1016/j.jqsrt.2019.106734

Hu, Y., 2007. Depolarization ratio–effective lidar ratio relation: Theoretical basis for space lidar cloud phase discrimination. Geophys Res Lett 34. https://doi.org/10.1029/2007gl029584

Huang, Y., Adebiyi, A.A., Formenti, P., Kok, J.F., 2021. Linking the Different Diameter Types of Aspherical Desert Dust Indicates That Models Underestimate Coarse Dust Emission. Geophys Res Lett 48. https://doi.org/10.1029/2020gl092054

Huang, Y., Kok, J.F., Kandler, K., Lindqvist, H., Nousiainen, T., Sakai, T., Adebiyi, A., Jokinen, O., 2020. Climate Models and Remote Sensing Retrievals Neglect Substantial Desert Dust Asphericity. Geophys Res Lett 47. https://doi.org/10.1029/2019gl086592

Huneeus, N., Schulz, M., Balkanski, Y., Griesfeller, J., Prospero, J., Kinne, S., Bauer, S., Boucher, O., Chin, M., Dentener, F., Diehl, T., Easter, R., Fillmore, D., Ghan, S., Ginoux, P., Grini, A., Horowitz, L., Koch, D., Krol, M.C., Landing, W., Liu, X., Mahowald, N., Miller, R., Morcrette, J.-J., Myhre, G., Penner, J., Perlwitz, J., Stier, P., Takemura, T., Zender, C.S., 2011. Global dust model intercomparison in AeroCom phase I. Atmos Chem Phys 11, 7781–7816. https://doi.org/10.5194/acp-11-7781-2011

Ibrahim, A., Franz, B.A., Ahmad, Z., Bailey, S.W., 2019. Multiband Atmospheric Correction Algorithm for Ocean Color Retrievals. Frontiers Earth Sci 7, 116. https://doi.org/10.3389/feart.2019.00116

III, J.R.T., Rajupet, S., Squire, H., Volbers, B., Zhou, J., Xie, L., Sankaran, R.M., Lacks, D.J., 2020. Electrostatic forces alter particle size distributions in atmospheric dust. Atmos Chem Phys 20, 3181–3190. https://doi.org/10.5194/acp-20-3181-2020

Ishizuka, M., Mikami, M., Leys, J.F., Shao, Y., Yamada, Y., Heidenreich, S., 2014. Power law relation between size-resolved vertical dust flux and friction velocity measured in a fallow wheat field. Aeolian Res 12, 87–99. https://doi.org/10.1016/j.aeolia.2013.11.002

Iversen, J.D., White, B.R., 1982. Saltation threshold on Earth, Mars and Venus. Sedimentology 29, 111–119. https://doi.org/10.1111/j.1365-3091.1982.tb01713.x

Jackson, B., 2022. Vortices and Dust Devils as Observed by the Mars Environmental Dynamics Analyzer Instruments on Board the Mars 2020 Perseverance Rover. Planet Sci J 3, 20. https://doi.org/10.3847/psj/ac4586

Järvinen, E., Kemppinen, O., Nousiainen, T., Kociok, T., Möhler, O., Leisner, T., Schnaiter, M., 2016. Laboratory investigations of mineral dust near-backscattering depolarization ratios. J Quantitative Spectrosc Radiat Transf 178, 192–208. https://doi.org/10.1016/j.jqsrt.2016.02.003

Jennings, B.R., Parslow, K., 1988. Particle size measurement: the equivalent spherical diameter. Proc Royal Soc Lond Math Phys Sci 419, 137–149. https://doi.org/10.1098/rspa.1988.0100

Jeong, G.Y., Park, M.Y., Kandler, K., Nousiainen, T., Kemppinen, O., 2016. Mineralogical properties and internal structures of individual fine particles of Saharan dust. Atmos Chem Phys 16, 12397–12410. https://doi.org/10.5194/acp-16-12397-2016

Jethva, H., Torres, O., Ahn, C., 2014. Global assessment of OMI aerosol single-scattering albedo using ground-based AERONET inversion: OMI Single-scattering Albedo Assessment. J Geophys Res Atmospheres 119, 9020–9040. https://doi.org/10.1002/2014jd021672

Jickells, T.D., An, Z.S., Andersen, K.K., Baker, A.R., Bergametti, G., Brooks, N., Cao, J.J., Boyd, P.W., Duce, R.A., Hunter, K.A., Kawahata, H., Kubilay, N., laRoche, J., Liss, P.S., Mahowald, N., Prospero, J.M., Ridgwell, A.J., Tegen, I., Torres, R., 2005. Global Iron Connections Between Desert Dust, Ocean Biogeochemistry, and Climate. Science 308, 67–71. https://doi.org/10.1126/science.1105959

Johnson, B.R., 1988. Invariant imbedding T matrix approach to electromagnetic scattering. Appl Optics 27, 4861. https://doi.org/10.1364/ao.27.004861

Josset, D., Pelon, J., Protat, A., Flamant, C., 2008. New approach to determine aerosol optical depth from combined CALIPSO and CloudSat ocean surface echoes. Geophys Res Lett 35. https://doi.org/10.1029/2008gl033442

Josset, D., Rogers, R., Pelon, J., Hu, Y., Liu, Z., Omar, A., Zhai, P.-W., 2011. CALIPSO lidar ratio retrieval over the ocean. Opt Express 19, 18696–706. https://doi.org/10.1364/oe.19.018696

Journet, E., Balkanski, Y., Harrison, S.P., 2014. A new data set of soil mineralogy for dust-cycle modeling. Atmos Chem Phys 14, 3801–3816. https://doi.org/10.5194/acp-14-3801-2014

Joussaume, S., 1990. 3-Dimensional Simulations of the Atmospheric Cycle of Desert Dust Particles Using a General-Circulation Model. Journal Of Geophysical Research-Atmospheres 95, 1909 1941.

Kahn, R., 1989. Comparative Planetology and the Atmosphere of Earth, Report to the Solar System Exploration Division. National Aeronautics and Space Administration, Pasadena.

Kahn, R., Petzold, A., Wendisch, M., Bierwirth, E., Dinter, T., Esselborn, M., Fiebig, M., Heese, B., Knippertz, P., Müller, D., Schladitz, A., Hoyningen-Huene, W.V., 2009. Desert dust aerosol air mass mapping in the western Sahara, using particle properties derived from space-based multi-angle imaging. Tellus B 61. https://doi.org/10.3402/tellusb.v61i1.16827

Kahn, R.A., Berkoff, T.A., Brock, C., Chen, G., Ferrare, R.A., Ghan, S., Hansico, T.F., Hegg, D.A., Martins, J.V., McNaughton, C.S., Murphy, D.M., Ogren, J.A., Penner, J.E., Pilewskie, P., Seinfeld, J.H., Worsnop, D.R., 2017. SAM-CAAM: A Concept for Acquiring Systematic Aircraft Measurements to Characterize Aerosol Air Masses. B Am Meteorol Soc 98, 2215–2228. https://doi.org/10.1175/bams-d-16-0003.1

Kahn, R.A., Gaitley, B.J., 2015. An analysis of global aerosol type as retrieved by MISR. J Geophys Res Atmospheres 120, 4248–4281. https://doi.org/10.1002/2015jd023322

Kahn, R.A., Lee, S.W., Martin, T.Z., Zurek, R.W., 1992. The Martian Dust Cycle, in: Kieffer, H.H., Jakosky, B.M., Snyder, C.W., Matthews, M. (Eds.), Mars. University of Arizona Press.

Kahn, R.A., Liu, Y., Diner, D.J., 2022. Handbook of Air Quality and Climate Change 1–14. https://doi.org/10.1007/978-981-15-2527-8_62-1

Kahnert, M., Nousiainen, T., Räisänen, P., 2007. Mie simulations as an error source in mineral aerosol radiative forcing calculations. Q J Roy Meteor Soc 133, 299–307. https://doi.org/10.1002/qj.40

Kahnert, M., Nousiainen, T., Veihelmann, B., 2005. Spherical and spheroidal model particles as an error source in aerosol climate forcing and radiance computations: A case study for feldspar aerosols. J Geophys Res Atmospheres 1984 2012 110. https://doi.org/10.1029/2004jd005558

Kahre, M., Murphy, J., Newman, C., Wilson, R., Cantor, B., Lemmon, M., Wolff, M., 2017. The Mars Dust Cycle, in: Haberle, R., Clancy, R., Forget, F., Smith, M., Zurek, R. (Eds.), The Atmosphere and Climate of Mars. Cambridge University Press, Cambridge, pp. 295–337. https://doi.org/10.1017/9781139060172.010

Kahre, M.A., Murphy, J.R., Haberle, R.M., 2006. Modeling the Martian dust cycle and surface dust reservoirs with the NASA Ames general circulation model. J Geophys Res Planets 1991 2012 111. https://doi.org/10.1029/2005je002588

Kahre, M.A., Murphy, J.R., Haberle, R.M., Montmessin, F., Schaeffer, J., 2005. Simulating the Martian dust cycle with a finite surface dust reservoir. Geophys Res Lett 32. https://doi.org/10.1029/2005gl023495

Kaiser, J.C., Hendricks, J., Righi, M., Jöckel, P., Tost, H., Kandler, K., Weinzierl, B., Sauer, D., Heimerl, K., Schwarz, J.P., Perring, A.E., Popp, T., 2019. Global aerosol modeling with MADE3 (v3.0) in EMAC (based on v2.53): model description and evaluation. Geosci Model Dev 12, 541–579. https://doi.org/10.5194/gmd-12-541-2019

Kalashnikova, O.V., Kahn, R., 2006. Ability of multiangle remote sensing observations to identify and distinguish mineral dust types: 2. Sensitivity over dark water. J Geophys Res Atmospheres 1984 2012 111. https://doi.org/10.1029/2005jd006756

Kalashnikova, O.V., Kahn, R., Sokolik, I.N., Li, W., 2005. Ability of multiangle remote sensing observations to identify and distinguish mineral dust types: Optical models and retrievals of optically thick plumes. J Geophys Res Atmospheres 1984 2012 110. https://doi.org/10.1029/2004jd004550

Kalashnikova, O.V., Sokolik, I.N., 2004. Modeling the radiative properties of nonspherical soil-derived mineral aerosols. J Quantitative Spectrosc Radiat Transf 87, 137–166. https://doi.org/10.1016/j.jqsrt.2003.12.026

Kandler, K., Benker, N., Bundke, U., Cuevas, E., Ebert, M., Knippertz, P., Rodríguez, S., Schütz, L., Weinbruch, S., 2007. Chemical composition and complex refractive index of Saharan Mineral Dust at Izaña, Tenerife (Spain) derived by electron microscopy. Atmos Environ 41, 8058–8074. https://doi.org/10.1016/j.atmosenv.2007.06.047

Kandler, K., Lieke, K., Benker, N., Emmel, C., Küpper, M., Müller-Ebert, D., Ebert, M., Scheuvens, D., Schladitz, A., Schütz, L., Weinbruch, S., 2011. Electron microscopy of particles collected at Praia, Cape Verde, during the Saharan Mineral Dust Experiment: particle chemistry, shape, mixing state and complex refractive index. Tellus B 63, 475–496. https://doi.org/10.1111/j.1600-0889.2011.00550.x

Kandler, K., Schütz, L., Deutscher, C., Ebert, M., Hofmann, H., Jäckel, S., Jaenicke, R., Knippertz, P., Lieke, K., Massling, A., Petzold, A., Schladitz, A., Weinzierl, B., Wiedensohler, A., Zorn, S., Weinbruch, S., 2009. Size distribution, mass concentration, chemical and mineralogical composition and derived optical parameters of the boundary layer aerosol at Tinfou, Morocco, during SAMUM 2006. Tellus B 61, 32–50. https://doi.org/10.1111/j.1600-0889.2008.00385.x

Kaufman, Y.J., Koren, I., Remer, L.A., Tanré, D., Ginoux, P., Fan, S., 2005. Dust transport and deposition observed from the Terra-Moderate Resolution Imaging Spectroradiometer (MODIS) spacecraft over the Atlantic Ocean. J Geophys Res Atmospheres 1984 2012 110. https://doi.org/10.1029/2003jd004436

Kaufman, Y.J., Wald, A.E., Remer, L.A., Gao, B.-C., Li, R.-R., Flynn, L., 1997. The MODIS 2.1- µm channel-correlation with visible reflectance for use in remote sensing of aerosol. Ieee T Geosci Remote 35, 1286–1298. https://doi.org/10.1109/36.628795

Kemppinen, O., Nousiainen, T., Lindqvist, H., 2015a. The impact of surface roughness on scattering by realistically shaped wavelength-scale dust particles. J Quantitative Spectrosc Radiat Transf 150, 55–67. https://doi.org/10.1016/j.jqsrt.2014.05.024

Kemppinen, O., Nousiainen, T., Merikallio, S., Räisänen, P., 2015b. Retrieving microphysical properties of dust-like particles using ellipsoids: the case of refractive index. Atmos Chem Phys 15, 11117–11132. https://doi.org/10.5194/acp-15-11117-2015

Kim, D., Chin, M., Cruz, C.A., Tong, D., Yu, H., 2021. Spring Dust in Western North America and Its Interannual Variability—Understanding the Role of Local and Transported Dust. J Geophys Res Atmospheres 126. https://doi.org/10.1029/2021jd035383

Kim, D., Chin, M., Kemp, E.M., Tao, Z., Peters-Lidard, C.D., Ginoux, P., 2017. Development of high-resolution dynamic dust source function - A case study with a strong dust storm in a regional model. Atmos Environ 159, 11–25. https://doi.org/10.1016/j.atmosenv.2017.03.045

Kim, D., Chin, M., Yu, H., Diehl, T., Tan, Q., Kahn, R.A., Tsigaridis, K., Bauer, S.E., Takemura, T., Pozzoli, L., Bellouin, N., Schulz, M., Peyridieu, S., Chedin, A., Koffi, B., 2014. Sources, sinks, and transatlantic transport of North African dust aerosol: A multimodel analysis and comparison with remote sensing data. J Geophys Res Atmospheres 119, 6259 6277. https://doi.org/10.1002/2013jd021099

Kim, D., Chin, M., Yu, H., Pan, X., Bian, H., Tan, Q., Kahn, R.A., Tsigaridis, K., Bauer, S.E., Takemura, T., Pozzoli, L., Bellouin, N., Schulz, M., 2019. Asian and Trans-Pacific Dust: A Multimodel and Multiremote Sensing Observation Analysis. J Geophys Res Atmospheres 124, 13534–13559. https://doi.org/10.1029/2019jd030822

Kim, M.-H., Omar, A.H., Tackett, J.L., Vaughan, M.A., Winker, D.M., Trepte, C.R., Hu, Y., Liu, Z., Poole, L.R., Pitts, M.C., Kar, J., Magill, B.E., 2018. The CALIPSO version 4 automated aerosol classification and lidar ratio selection algorithm. Atmos Meas Tech 11, 6107–6135. https://doi.org/10.5194/amt-11-6107-2018

Kinne, S., Schulz, M., Textor, C., Guibert, S., Balkanski, Y., Bauer, S.E., Berntsen, T., Berglen, T.F., Boucher, O., Chin, M., Collins, W., Dentener, F., Diehl, T., Easter, R., Feichter, J., Fillmore, D., Ghan, S., Ginoux, P., Gong, S., Grini, A., Hendricks, J., Herzog, M., Horowitz, L., Isaksen, I., Iversen, T., Kirkevåg, A., Kloster, S., Koch, D., Kristjansson, J.E., Krol, M., Lauer, A., Lamarque, J.F., Lesins, G., Liu, X., Lohmann, U., Montanaro, V., Myhre, G., Penner, J., Pitari, G., Reddy, S., Seland, O., Stier, P., Takemura, T., Tie, X., 2006. An AeroCom initial assessment – optical properties in aerosol component modules of global models. Atmos Chem Phys 6, 1815–1834. https://doi.org/10.5194/acp-6-1815-2006

Kleinböhl, A., Schofield, J.T., Kass, D.M., Abdou, W.A., Backus, C.R., Sen, B., Shirley, J.H., Lawson, W.G., Richardson, M.I., Taylor, F.W., Teanby, N.A., McCleese, D.J., 2009. Mars Climate Sounder limb profile retrieval of atmospheric temperature, pressure, and dust and water ice opacity. J Geophys Res Planets 1991 2012 114, n/a-n/a. https://doi.org/10.1029/2009je003358

Klose, M., Jorba, O., Ageitos, M.G., Escribano, J., Dawson, M.L., Obiso, V., Tomaso, E.D., Basart, S., Pinto, G.M., Macchia, F., Ginoux, P., Guerschman, J., Prigent, C., Huang, Y., Kok, J.F., Miller, R.L., García-Pando, C.P., 2021. Mineral dust cycle in the Multiscale Online Nonhydrostatic AtmospheRe CHemistry model (MONARCH) Version 2.0. Geoscientific Model Dev Discuss 2021, 1–59. https://doi.org/10.5194/gmd-2021-32

Klüser, L., Martynenko, D., Holzer-Popp, T., 2011. Thermal infrared remote sensing of mineral dust over land and ocean: a spectral SVD based retrieval approach for IASI. Atmos. Meas. Tech. 4, 757–773. https://doi.org/10.5194/amt-4-757-2011

Knippertz, P., Stutz, J.-B.W., 2014. Mineral Dust A Key Player in the Earth System. https://doi.org/10.1007/978-94-017-8978-3

Kok, J.F., 2011. A scaling theory for the size distribution of emitted dust aerosols suggests climate models underestimate the size of the global dust cycle. Proc National Acad Sci 108, 1016–1021. https://doi.org/10.1073/pnas.1014798108

Kok, J.F., Adebiyi, A.A., Albani, S., Balkanski, Y., Checa-Garcia, R., Chin, M., Colarco, P.R., Hamilton, D.S., Huang, Y., Ito, A., Klose, M., Leung, D.M., Li, L., Mahowald, N.M., Miller, R.L., Obiso, V., García-Pando, C.P., Rocha-Lima, A., Wan, J.S., Whicker, C.A., 2021. Improved representation of the global dust cycle using observational constraints on dust properties and abundance. Atmos. Chem. Phys. 21, 8127–8167. https://doi.org/10.5194/acp-21-8127-2021

Kok, J.F., Mahowald, N.M., Fratini, G., Gillies, J.A., Ishizuka, M., Leys, J.F., Mikami, M., Park, M.S., Park, S.U., Pelt, R.S.V., Zobeck, T.M., 2014. An improved dust emission model – Part 1: Model description and comparison against measurements. Atmospheric Chemistry And Physics 14, 13023 13041. https://doi.org/10.5194/acp-14-13023-2014-supplement

Kok, J.F., Renno, N.O., 2006. Enhancement of the emission of mineral dust aerosols by electric forces. Geophys Res Lett 33. https://doi.org/10.1029/2006gl026284

Kok, J.F., Ridley, D.A., Zhou, Q., Miller, R.L., Zhao, C., Heald, C.L., Ward, D.S., Albani, S., Haustein, K., 2017. Smaller desert dust cooling effect estimated from analysis of dust size and abundance. Nat Geosci 10, 274–278. https://doi.org/10.1038/ngeo2912

Kok, J.F., Storelvmo, T., Karydis, V.A., Adebiyi, A.A., Mahowald, N.M., Evan, A.T., He, C., Leung, D.M., 2023. Mineral dust aerosol impacts on global climate and climate change. Nat Rev Earth Environ 4, 71–86. https://doi.org/10.1038/s43017-022-00379-5

Kong, S., Sato, K., Bi, L., 2022. Lidar Ratio–Depolarization Ratio Relations of Atmospheric Dust Aerosols: The Super-Spheroid Model and High Spectral Resolution Lidar Observations. J. Geophys. Res.: Atmos. 127, e2021JD035629. https://doi.org/10.1029/2021jd035629

Koren, I., Remer, L.A., Kaufman, Y.J., Rudich, Y., Martins, J.V., 2007. On the twilight zone between clouds and aerosols: CLOUDS TWILIGHT ZONE. Geophys Res Lett 34. https://doi.org/10.1029/2007gl029253

Kwon, H.-J., Cho, S.-H., Chun, Y., Lagarde, F., Pershagen, G., 2002. Effects of the Asian Dust Events on Daily Mortality in Seoul, Korea. Environ Res 90, 1–5. https://doi.org/10.1006/enrs.2002.4377

Lafon, S., Sokolik, I.N., Rajot, J.L., Caquineau, S., Gaudichet, A., 2006. Characterization of iron oxides in mineral dust aerosols: Implications for light absorption. J Geophys Res Atmospheres 1984 2012 111. https://doi.org/10.1029/2005jd007016

Lee, H., Honda, Y., Lim, Y.-H., Guo, Y.L., Hashizume, M., Kim, H., 2014. Effect of Asian dust storms on mortality in three Asian cities. Atmos Environ 89, 309–317. https://doi.org/10.1016/j.atmosenv.2014.02.048

Lee, J., Hsu, N.C., Sayer, A.M., Bettenhausen, C., Yang, P., 2017. AERONET-Based Nonspherical Dust Optical Models and Effects on the VIIRS Deep Blue/SOAR Over Water

Aerosol Product. J Geophys Res Atmospheres 122, 10,384-10,401. https://doi.org/10.1002/2017jd027258

Lee, K., Choi, H., Kim, J., 2020. Refractive Index for Asian Dust in the Ultraviolet-Visible Region Determined From Compositional Analysis and Validated With OMI Observations. J Geophys Res Atmospheres 125. https://doi.org/10.1029/2019jd030629

Lemmon, M.T., Guzewich, S.D., McConnochie, T., Vicente-Retortillo, A., Martínez, G., Smith, M.D., Bell, J.F., Wellington, D., Jacob, S., 2019. Large Dust Aerosol Sizes Seen During the 2018 Martian Global Dust Event by the Curiosity Rover. Geophys Res Lett 46, 9448–9456. https://doi.org/10.1029/2019gl084407

Leovy, C., Mintz, Y., 1969. Numerical Simulation of the Atmospheric Circulation and Climate of Mars. J Atmos Sci 26, 1167–1190. https://doi.org/10.1175/1520-0469(1969)026<;1167:nsotac>2.0.co;2

Levy, R., Remer, L., Tanré, D., Mattoo, S., Kaufman, Y., 2009. Algorithm for remote sensing of tropospheric aerosol over dark targets from MODIS: Collections 005 and 051: Revision 2, February 2009, MODIS Algorithm Theoretical Basis Document.

Levy, R.C., Mattoo, S., Munchak, L.A., Remer, L.A., Sayer, A.M., Patadia, F., Hsu, N.C., 2013. The Collection 6 MODIS aerosol products over land and ocean. Atmos Meas Tech 6, 2989–3034. https://doi.org/10.5194/amt-6-2989-2013

Levy, R.C., Remer, L.A., Dubovik, O., 2007. Global aerosol optical properties and application to Moderate Resolution Imaging Spectroradiometer aerosol retrieval over land. J Geophys Res Atmospheres 112. https://doi.org/10.1029/2006jd007815

Lewis, J.M., Martin, D.W., Rabin, R.M., Moosmüller, H., 2010. Suomi: Pragmatic Visionary. B Am Meteorol Soc 91, 559–578. https://doi.org/10.1175/2009bams2897.1

Lewis, J.M., Phillips, J.M., Menzel, W.P., Haar, T.H.V., Moosmüller, H., House, F.B., Fearon, M.G., 2018. Verner Suomi: The Life and Work of the Founder of Satellite Meteorology, 1st ed. American Meteorological Society.

Li, F., Vogelmann, A.M., Ramanathan, V., 2004. Saharan Dust Aerosol Radiative Forcing Measured from Space. J Climate 17, 2558–2571. https://doi.org/10.1175/1520-0442(2004)017<;2558:sdarfm>2.0.co;2

Li, J., Osada, K., 2007. Water-Insoluble Particles in Spring Snow at Mt. Tateyama, Japan: Characteristics of the Shape Factors and Size Distribution in Relation with Their Origin and Transportation. J Meteorological Soc Jpn Ser Ii 85, 137–149. https://doi.org/10.2151/jmsj.85.137

Li, L., Mahowald, N.M., Miller, R.L., García-Pando, C.P., Klose, M., Hamilton, D.S., Ageitos, M.G., Ginoux, P., Balkanski, Y., Green, R.O., Kalashnikova, O., Kok, J.F., Obiso, V., Paynter, D., Thompson, D.R., 2021. Quantifying the range of the dust direct radiative effect due to source mineralogy uncertainty. Atmos Chem Phys 21, 3973–4005. https://doi.org/10.5194/acp-21-3973-2021

Limbacher, J.A., Kahn, R.A., Lee, J., 2022. The new MISR research aerosol retrieval algorithm: a multi-angle, multi-spectral, bounded-variable least squares retrieval of aerosol particle properties over both land and water. Atmos Meas Tech 15, 6865–6887. https://doi.org/10.5194/amt-15-6865-2022

Lin, W., Bi, L., Dubovik, O., 2018. Assessing Superspheroids in Modeling the Scattering Matrices of Dust Aerosols. J. Geophys. Res.: Atmos. 123, 13,917-13,943. https://doi.org/10.1029/2018jd029464

Lin, W., Bi, L., Weng, F., Li, Z., Dubovik, O., 2021. Capability of Superspheroids for Modeling PARASOL Observations Under Dusty-Sky Conditions. J. Geophys. Res.: Atmos. 126. https://doi.org/10.1029/2020jd033310

Lindqvist, H., Jokinen, O., Kandler, K., Scheuvens, D., Nousiainen, T., 2014. Single scattering by realistic, inhomogeneous mineral dust particles with stereogrammetric shapes. Atmos Chem Phys 14, 143–157. https://doi.org/10.5194/acp-14-143-2014

Liu, C., Panetta, R.L., Yang, P., Macke, A., Baran, A.J., 2013. Modeling the scattering properties of mineral aerosols using concave fractal polyhedra. Appl Optics 52, 640. https://doi.org/10.1364/ao.52.000640

Liu, C.-M., Young, C.-Y., Lee, Y.-C., 2006. Influence of Asian dust storms on air quality in Taiwan. Sci Total Environ 368, 884–897. https://doi.org/10.1016/j.scitotenv.2006.03.039

Liu, H., Jacob, D., Bey, I., Yantosca, R., 2001. Constraints from Pb-210 and Be-7 on wet deposition and transport in a global three-dimensional chemical tracer model driven by assimilated meteorological fields. Journal Of Geophysical Research-Atmospheres 106, 12109 12128.

Liu, J., Yang, P., Muinonen, K., 2015. Dust-aerosol optical modeling with Gaussian spheres: Combined invariant-imbedding T-matrix and geometric-optics approach. J Quantitative Spectrosc Radiat Transf 161, 136–144. https://doi.org/10.1016/j.jqsrt.2015.04.003

Liu, Q.H., 1997. The PSTD algorithm: A time-domain method requiring only two cells per wavelength. Microw Opt Techn Let 15, 158–165. https://doi.org/10.1002/(sici)1098-2760(19970620)15:3<;158::aid-mop11>3.0.co;2-3

Liu, X., Easter, R.C., Ghan, S.J., Zaveri, R., Rasch, P., Shi, X., Lamarque, J.-F., Gettelman, A., Morrison, H., Vitt, F., Conley, A., Park, S., Neale, R., Hannay, C., Ekman, A.M.L., Hess, P., Mahowald, N., Collins, W., Iacono, M.J., Bretherton, C.S., Flanner, M.G., Mitchell, D., 2012. Toward a minimal representation of aerosols in climate models: description and evaluation in the Community Atmosphere Model CAM5. Geosci Model Dev 5, 709–739. https://doi.org/10.5194/gmd-5-709-2012

Liu, Z., Winker, D., Omar, A., Vaughan, M., Trepte, C., Hu, Y., Powell, K., Sun, W., Lin, B., 2011. Effective lidar ratios of dense dust layers over North Africa derived from the CALIOP measurements. J Quantitative Spectrosc Radiat Transf 112, 204–213. https://doi.org/10.1016/j.jqsrt.2010.05.006

Lorenz, L.V., 1890. Upon the light reflected and refracted by a transparent sphere. Det Konelige Danske Videnskabernes Selskabs Skrifter 6, 1–62.

Lyapustin, A., Wang, Y., Korkin, S., Huang, D., 2018. MODIS Collection 6 MAIAC algorithm. Atmos Meas Tech 11, 5741–5765. https://doi.org/10.5194/amt-11-5741-2018

Lyapustin, A.I., Wang, Y., Laszlo, I., Hilker, T., G.Hall, F., Sellers, P.J., Tucker, C.J., Korkin, S.V., 2012. Multi-angle implementation of atmospheric correction for MODIS (MAIAC): 3. Atmospheric correction. Remote Sens Environ 127, 385–393. https://doi.org/10.1016/j.rse.2012.09.002

Lynch, D.K., Livingston, W., 2001. Color and Light in Nature. Cambridge University Press, New York.

Mackowski, D.W., Mishchenko, M.I., 1996. Calculation of the T matrix and the scattering matrix for ensembles of spheres. J Opt Soc Am 13, 2266. https://doi.org/10.1364/josaa.13.002266

Madeleine, J. -B., Forget, F., Millour, E., Montabone, L., Wolff, M.J., 2011. Revisiting the radiative impact of dust on Mars using the LMD Global Climate Model. J Geophys Res Planets 1991 2012 116. https://doi.org/10.1029/2011je003855

Mahowald, N., Albani, S., Kok, J.F., Engelstaeder, S., Scanza, R., Ward, D.S., Flanner, M.G., 2014. The size distribution of desert dust aerosols and its impact on the Earth system. Aeolian Res 15, 53–71. https://doi.org/10.1016/j.aeolia.2013.09.002

Mahowald, N., Kohfeld, K., Hansson, M., Balkanski, Y., Harrison, S., Prentice, I., Schulz, M., Rodhe, H., 1999. Dust sources and deposition during the last glacial maximum and current climate: A comparison of model results with paleodata from ice cores and marine sediments. Journal Of Geophysical Research-Atmospheres 104, 15895 15916.

Malm, W.C., Sisler, J.F., Huffman, D., Eldred, R.A., Cahill, T.A., 1994. Spatial and seasonal trends in particle concentration and optical extinction in the United States. J Geophys Res Atmospheres 99, 1347–1370. https://doi.org/10.1029/93jd02916

Maring, H., Savoie, D.L., Izaguirre, M.A., Custals, L., Reid, J.S., 2003. Mineral dust aerosol size distribution change during atmospheric transport. J Geophys Res Atmospheres 1984 2012 108. https://doi.org/10.1029/2002jd002536

Marshak, A., Ackerman, A., Silva, A.M. da, Eck, T., Holben, B., Kahn, R., Kleidman, R., Knobelspiesse, K., Levy, R., Lyapustin, A., Oreopoulos, L., Remer, L., Torres, O., Várnai, T., Wen, G., Yorks, J., 2021. Aerosol Properties in Cloudy Environments from Remote Sensing Observations: A Review of the Current State of Knowledge. B Am Meteorol Soc 102, E2177–E2197. https://doi.org/10.1175/bams-d-20-0225.1

Marshak, A., Lyapustin, A., Schuster, G.L., Szabo, A., Eckman, R., 2022. Editorial: DSCOVR EPIC/NISTAR: 5 Years of Observing Earth From the First Lagrangian Point. Frontiers Remote Sens 3, 963660. https://doi.org/10.3389/frsen.2022.963660

Marticorena, B., Bergametti, G., 1995. Modeling the Atmospheric Dust Cycle: 1. Design of a soil-derived dust emission scheme. Journal Of Geophysical Research-Atmospheres 100, 16415 16430.

Martín, J.C.G., Guirado, D., Frattin, E., Bermudez-Edo, M., Gonzalez, P.C., Reyes, F.J.O., Nousiainen, T., Gutiérrez, P.J., Moreno, F., Muñoz, O., 2021. On the application of scattering matrix measurements to detection and identification of major types of airborne aerosol particles: Volcanic ash, desert dust and pollen. J Quantitative Spectrosc Radiat Transf 271, 107761. https://doi.org/10.1016/j.jqsrt.2021.107761

Martins, J., 2016. Airborne Open Polar/Imaging Nephelometer for Ice Particles in Cirrus Clouds and Aerosols Field Campaign Report (No. DOE/SC-ARM-15-063). U.S. Department of Energy Office of Science.

Martonchik, J.V., Kahn, R.A., Diner, D.J., 2009. Satellite Aerosol Remote Sensing over Land 267–293. https://doi.org/10.1007/978-3-540-69397-0_9

Matthias, V., Freudenthaler, V., Amodeo, A., Balin, I., Balis, D., Bösenberg, J., Chaikovsky, A., Chourdakis, G., Comeron, A., Delaval, A., Tomasi, F.D., Eixmann, R., Hågård, A., Komguem, L., Kreipl, S., Matthey, R., Rizi, V., Rodrigues, J.A., Wandinger, U., Wang, X., 2004. Aerosol lidar intercomparison in the framework of the EARLINET project 1 Instruments: erratum. Appl Optics 43, 2578. https://doi.org/10.1364/ao.43.002578

McMurry, P.H., 2000. A review of atmospheric aerosol measurements. Atmos Environ 34, 1959–1999. https://doi.org/10.1016/s1352-2310(99)00455-0

Medalia, A.I., Rivin, D., 1982. Particulate carbon and other components of soot and carbon black. Carbon 20, 481–492. https://doi.org/10.1016/0008-6223(82)90084-7

Meng, Z., Yang, P., Kattawar, G.W., Bi, L., Liou, K.N., Laszlo, I., 2010. Single-scattering properties of tri-axial ellipsoidal mineral dust aerosols: A database for application to radiative transfer calculations. J Aerosol Sci 41, 501–512. https://doi.org/10.1016/j.jaerosci.2010.02.008

Mie, G., 1908. Beiträge zur Optik trüber Medien, speziell kolloidaler Metallösungen. Ann Phys-berlin 330, 377–445. https://doi.org/10.1002/andp.19083300302

Miffre, A., Mehri, T., Francis, M., Rairoux, P., 2016. UV–VIS depolarization from Arizona Test Dust particles at exact backscattering angle. J. Quant. Spectrosc. Radiat. Transf. 169, 79–90. https://doi.org/10.1016/j.jqsrt.2015.09.016

Mills, M.M., Ridame, C., Davey, M., Roche, J.L., Geider, R.J., 2004. Iron and phosphorus co-limit nitrogen fixation in the eastern tropical North Atlantic. Nature 429, 292–294. https://doi.org/10.1038/nature02550

Mishchenko, M.I., 2006. Scale invariance rule in electromagnetic scattering. J Quantitative Spectrosc Radiat Transf 101, 411–415. https://doi.org/10.1016/j.jqsrt.2006.02.047

Mishchenko, M.I., 2000. Calculation of the amplitude matrix for a nonspherical particle in a fixed orientation. Appl Optics 39, 1026. https://doi.org/10.1364/ao.39.001026

Mishchenko, M.I., Lacis, A.A., Carlson, B.E., Travis, L.D., 1995. Nonsphericity of dust-like tropospheric aerosols: Implications for aerosol remote sensing and climate modeling. Geophys Res Lett 22, 1077–1080. https://doi.org/10.1029/95gl00798

Mishchenko, M.I., Travis, L.D., 1998. Capabilities and limitations of a current FORTRAN implementation of the T-matrix method for randomly oriented, rotationally symmetric scatterers. J Quantitative Spectrosc Radiat Transf 60, 309–324. https://doi.org/10.1016/s0022-4073(98)00008-9

Mishchenko, M.I., Travis, L.D., Kahn, R.A., West, R.A., 1997. Modeling phase functions for dustlike tropospheric aerosols using a shape mixture of randomly oriented polydisperse spheroids. J Geophys Res Atmospheres 102, 16831–16847. https://doi.org/10.1029/96jd02110

Mishchenko, M.I., Travis, L.D., Lacis, A.A., 2006. Multiple Scattering of Light by Particles, Cambridge University Press. Cambridge University Press, Cambridge.

Mishchenko, M.I., Travis, L.D., Lacis, A.A., 2002. Scattering, Absorption, and Emission of Light by Small Particles. Cambridge University Press, Cambridge.

Mishra, S.K., Dey, S., Tripathi, S.N., 2008. Implications of particle composition and shape to dust radiative effect: A case study from the Great Indian Desert. Geophys Res Lett 35. https://doi.org/10.1029/2008gl036058

Mishra, S.K., Tripathi, S.N., 2008. Modeling optical properties of mineral dust over the Indian Desert. J Geophys Res Atmospheres 1984 2012 113. https://doi.org/10.1029/2008jd010048

Montabone, L., Forget, F., Millour, E., Wilson, R.J., Lewis, S.R., Cantor, B., Kass, D., Kleinböhl, A., Lemmon, M.T., Smith, M.D., Wolff, M.J., 2015. Eight-year climatology of dust optical depth on Mars. Icarus 251, 65–95. https://doi.org/10.1016/j.icarus.2014.12.034

Moosmüller, H., 2023. Optical Properties of Nonspherical, Light-Absorbing Particles: Black Carbon and Mineral Dust Aerosols, in: Mengüç, M.P., Francoeur, M. (Eds.), Elsevier Science and Technology Books, Nanophotonics Series. pp. 349–370. https://doi.org/10.1016/b978-0-323-99901-4.00005-6.

Moosmüller, H., Chakrabarty, R.K., 2011. Technical Note: Simple analytical relationships between Ångström coefficients of aerosol extinction, scattering, absorption, and single scattering albedo. Atmos Chem Phys 11, 10677–10680. https://doi.org/10.5194/acp-11-10677-2011

Moosmüller, H., Engelbrecht, J.P., Skiba, M., Frey, G., Chakrabarty, R.K., Arnott, W.P., 2012. Single scattering albedo of fine mineral dust aerosols controlled by iron concentration. J Geophys Res Atmospheres 1984 2012 117, n/a-n/a. https://doi.org/10.1029/2011jd016909

Moosmüller, H., Sorensen, C.M., 2018a. Single scattering albedo of homogeneous, spherical particles in the transition regime. J Quantitative Spectrosc Radiat Transf 219, 333–338. https://doi.org/10.1016/j.jqsrt.2018.08.015

Moosmüller, H., Sorensen, C.M., 2018b. Small and large particle limits of single scattering albedo for homogeneous, spherical particles. J Quantitative Spectrosc Radiat Transf 204, 250–255. https://doi.org/10.1016/j.jqsrt.2017.09.029

Moxim, W.J., Fan, S., Levy, H., 2011. The meteorological nature of variable soluble iron transport and deposition within the North Atlantic Ocean basin. J Geophys Res Atmospheres 1984 2012 116. https://doi.org/10.1029/2010jd014709

Mugnai, A., Wiscombe, W.J., 1986. Scattering from nonspherical Chebyshev particles I: cross sections, single-scattering albedo, asymmetry factor, and backscattered fraction. Appl Optics 25, 1235. https://doi.org/10.1364/ao.25.001235

Muinonen, K. T., Nousiainen, T., Fast, P., Lumme, K., Peltoniemi, J. I., 1996. Light scattering by Gaussian random particles: Ray optics approximation. J. Quantitative Spectrosc Radiat Transf 55, 577-601. https://doi.org/10.1016/0022-4073(96)00003-9

Muinonen, K., Nousiainen, T., Lindqvist, H., Muñoz, O., Videen, G., 2009. Light scattering by Gaussian particles with internal inclusions and roughened surfaces using ray optics. J Quantitative Spectrosc Radiat Transf 110, 1628–1639. https://doi.org/10.1016/j.jqsrt.2009.03.012

Mulholland, D.P., Read, P.L., Lewis, S.R., 2013. Simulating the interannual variability of major dust storms on Mars using variable lifting thresholds. Icarus 223, 344–358. https://doi.org/10.1016/j.icarus.2012.12.003

Muñoz, O., Moreno, F., Guirado, D., Dabrowska, D.D., Volten, H., Hovenier, J.W., 2012. The Amsterdam–Granada Light Scattering Database. J Quantitative Spectrosc Radiat Transf 113, 565–574. https://doi.org/10.1016/j.jqsrt.2012.01.014

Muñoz, O., Moreno, F., Guirado, D., Ramos, J.L., López, A., Girela, F., Jerónimo, J.M., Costillo, L.P., Bustamante, I., 2010. Experimental determination of scattering matrices of dust particles at visible wavelengths: The IAA light scattering apparatus. J Quantitative Spectrosc Radiat Transf 111, 187–196. https://doi.org/10.1016/j.jqsrt.2009.06.011

Muñoz, O., Moreno, F., Guirado, D., Ramos, J.L., Volten, H., Hovenier, J.W., 2011. The IAA cosmic dust laboratory: Experimental scattering matrices of clay particles. Icarus 211, 894–900. https://doi.org/10.1016/j.icarus.2010.10.027

Muñoz, O., Volten, H., Haan, J.F., Vassen, W., Hovenier, J.W., 2001. Experimental determination of scattering matrices of randomly oriented fly ash and clay particles at 442 and 633 nm. J Geophys Res Atmospheres 106, 22833–22844. https://doi.org/10.1029/2000jd000164

Muñoz, O., Volten, H., Hovenier, J.W., Nousiainen, T., Muinonen, K., Guirado, D., Moreno, F., Waters, L.B.F.M., 2007. Scattering matrix of large Saharan dust particles: Experiments and computations. J Geophys Res Atmospheres 112. https://doi.org/10.1029/2006jd008074

Nakajima, T., Tanaka, M., Hayasaka, T., Miyake, Y., Nakanishi, Y., Sasamoto, K., 1986. Airborne measurements of the optical stratification of aerosols in turbid atmospheres. Appl. Opt. 25, 4374. https://doi.org/10.1364/ao.25.004374

Nakajima, T., Tanaka, M., Yamano, M., Shiobara, M., Arao, K., Nakanishi, Y., 1989. Aerosol Optical Characteristics in the Yellow Sand Events Observed in May, 1982 at Nagasaki-Part II Models. J Meteorological Soc Jpn Ser Ii 67, 279–291. https://doi.org/10.2151/jmsj1965.67.2_279

Nakajima, T., Tanaka, M., Yamauchi, T., 1983. Retrieval of the optical properties of aerosols from aureole and extinction data. Appl. Opt. 22, 2951. https://doi.org/10.1364/ao.22.002951

Nakajima, T., Tonna, G., Rao, R., Boi, P., Kaufman, Y., Holben, B., 1996. Use of sky brightness measurements from ground for remote sensing of particulate polydispersions. Appl. Opt. 35, 2672. https://doi.org/10.1364/ao.35.002672

Natarajan, M., Cianciolo, A.D., Fairlie, T.D., Richardson, M.I., McConnochie, T.H., 2015. Sensitivity of simulated Martian atmospheric temperature to prescribed dust opacity distribution: Comparison of model results with reconstructed data from Mars Exploration Rover missions. J Geophys Res Planets 120, 2002–2019. https://doi.org/10.1002/2015je004813

Newman, C.E., Lewis, S.R., Read, P.L., Forget, F., 2002. Modeling the Martian dust cycle 2. Multiannual radiatively active dust transport simulations. J Geophys Res Planets 1991 2012 107, 7-1-7–15. https://doi.org/10.1029/2002je001920

Newman, C.E., Richardson, M.I., 2015. The impact of surface dust source exhaustion on the martian dust cycle, dust storms and interannual variability, as simulated by the MarsWRF General Circulation Model. Icarus 257, 47–87. https://doi.org/10.1016/j.icarus.2015.03.030

Nickovic, S., Vukovic, A., Vujadinovic, M., Djurdjevic, V., Pejanovic, G., 2012. Technical Note: High-resolution mineralogical database of dust-productive soils for atmospheric dust modeling. Atmos Chem Phys 12, 845–855. https://doi.org/10.5194/acp-12-845-2012

Nisantzi, A., Mamouri, R.E., Ansmann, A., Schuster, G.L., Hadjimitsis, D.G., 2015. Middle East versus Saharan dust extinction-to-backscatter ratios. Atmos Chem Phys 15, 7071–7084. https://doi.org/10.5194/acp-15-7071-2015

Nousiainen, T., 2009. Optical modeling of mineral dust particles: A review. J Quantitative Spectrosc Radiat Transf 110, 1261–1279. https://doi.org/10.1016/j.jqsrt.2009.03.002

Nousiainen, T., Kahnert, M., Veihelmann, B., 2006. Light scattering modeling of small feldspar aerosol particles using polyhedral prisms and spheroids. J Quantitative Spectrosc Radiat Transf 101, 471–487. https://doi.org/10.1016/j.jqsrt.2006.02.038

Nousiainen, T., Kandler, K., 2014. Light Scattering Reviews 9, Light Scattering and Radiative Transfer 3–52. https://doi.org/10.1007/978-3-642-37985-7_1

Nousiainen, T., Muinonen, K., Räisänen, P., 2003. Scattering of light by large Saharan dust particles in a modified ray optics approximation. J Geophys Res Atmospheres 1984 2012 108, AAC 12-1-AAC 12-17. https://doi.org/10.1029/2001jd001277

Nousiainen, T., Muñoz, O., Lindqvist, H., Mauno, P., Videen, G., 2011. Light scattering by large Saharan dust particles: Comparison of modeling and experimental data for two samples. J Quantitative Spectrosc Radiat Transf 112, 420–433. https://doi.org/10.1016/j.jqsrt.2010.09.003

Nousiainen, T., Vermeulen, K., 2003. Comparison of measured single-scattering matrix of feldspar particles with T-matrix simulations using spheroids. J Quantitative Spectrosc Radiat Transf 79, 1031–1042. https://doi.org/10.1016/s0022-4073(02)00337-0

Ojha, L., Lewis, K., Karunatillake, S., Schmidt, M., 2018. The Medusae Fossae Formation as the single largest source of dust on Mars. Nat Commun 9, 2867. https://doi.org/10.1038/s41467-018-05291-5

Omar, A., Liu, Z., Vaughan, M., Thornhill, K., Kittaka, C., Ismail, S., Hu, Y., Chen, G., Powell, K., Winker, D., Trepte, C., Winstead, E., Anderson, B., 2010. Extinction-to-backscatter ratios of Saharan dust layers derived from in situ measurements and CALIPSO overflights during NAMMA. J Geophys Res Atmospheres 115. https://doi.org/10.1029/2010jd014223

Omar, A.H., Winker, D.M., Vaughan, M.A., Hu, Y., Trepte, C.R., Ferrare, R.A., Lee, K.-P., Hostetler, C.A., Kittaka, C., Rogers, R.R., Kuehn, R.E., Liu, Z., 2009. The CALIPSO

Automated Aerosol Classification and Lidar Ratio Selection Algorithm. J Atmos Ocean Tech 26, 1994–2014. https://doi.org/10.1175/2009jtecha1231.1

Painter, T.H., Barrett, A.P., Landry, C.C., Neff, J.C., Cassidy, M.P., Lawrence, C.R., McBride, K.E., Farmer, G.L., 2007. Impact of disturbed desert soils on duration of mountain snow cover. Geophys Res Lett 34. https://doi.org/10.1029/2007gl030284

Panta, A., Kandler, K., Alastuey, A., González-Flórez, C., González-Romero, A., Klose, M., Querol, X., Reche, C., Yus-Díez, J., García-Pando, C.P., 2023. Insights into the single-particle composition, size, mixing state, and aspect ratio of freshly emitted mineral dust from field measurements in the Moroccan Sahara using electron microscopy. Atmos. Chem. Phys. 23, 3861–3885. https://doi.org/10.5194/acp-23-3861-2023

Papagiannopoulos, N., Mona, L., Alados-Arboledas, L., Amiridis, V., Baars, H., Binietoglou, I., Bortoli, D., D'Amico, G., Giunta, A., Guerrero-Rascado, J.L., Schwarz, A., Pereira, S., Spinelli, N., Wandinger, U., Wang, X., Pappalardo, G., 2016. CALIPSO climatological products: evaluation and suggestions from EARLINET. Atmos Chem Phys 16, 2341–2357. https://doi.org/10.5194/acp-16-2341-2016

Patterson, E.M., Gillette, D.A., 1977. Commonalities in measured size distributions for aerosols having a soil-derived component. J Geophys Res 82, 2074–2082. https://doi.org/10.1029/jc082i015p02074

Patterson, E.M., Gillette, D.A., Stockton, B.H., 1977. Complex index of refraction between 300 and 700 nm for Saharan aerosols. J Geophys Res 82, 3153–3160. https://doi.org/10.1029/jc082i021p03153

Pauly, R., 2017. Cloud and Aerosol 1064nm Lidar Ratio Retrievals from the CATS Instrument.

Pérez García-Pando, C., Miller, R.L., Perlwitz, J.P., Rodríguez, S., Prospero, J.M., 2016. Predicting the mineral composition of dust aerosols: Insights from elemental composition measured at the Izaña Observatory. Geophys Res Lett 43, 10,520-10,529. https://doi.org/10.1002/2016gl069873

Perlwitz, J.P., García-Pando, C.P., Miller, R.L., 2015a. Predicting the mineral composition of dust aerosols – Part 2: Model evaluation and identification of key processes with observations. Atmos Chem Phys 15, 11629–11652. https://doi.org/10.5194/acp-15-11629-2015

Perlwitz, J.P., García-Pando, C.P., Miller, R.L., 2015b. Predicting the mineral composition of dust aerosols – Part 1: Representing key processes. Atmos Chem Phys 15, 11593–11627. https://doi.org/10.5194/acp-15-11593-2015

Petzold, A., VEIRA, A., MUND, S., ESSELBORN, M., KIEMLE, C., WEINZIERL, B., HAMBURGER, T., EHRET, G., LIEKE, K., KANDLER, K., 2011. Mixing of mineral dust with urban pollution aerosol over Dakar (Senegal): impact on dust physico-chemical and radiative properties. Tellus B 63, 619–634. https://doi.org/10.1111/j.1600-0889.2011.00547.x

Peyridieu, S., Chédin, A., Tanré, D., Capelle, V., Pierangelo, C., Lamquin, N., Armante, R., 2009. Saharan dust infrared optical depth and altitude retrieved from AIRS: a focus over North Atlantic – comparison to MODIS and CALIPSO. https://doi.org/10.5194/acpd-9-21199-2009

Pilinis, C., Li, X., 1998. Particle shape and internal inhomogeneity effects on the optical properties of tropospheric aerosols of relevance to climate forcing. J Geophys Res Atmospheres 103, 3789–3800. https://doi.org/10.1029/97jd02792

Pollack, J.B., Colburn, D., Kahn, R., Hunter, J., Camp, W.V., Carlston, C.E., Wolf, M.R., 1977. Properties of aerosols in the Martian atmosphere, as inferred from Viking Lander imaging data. J Geophys Res 82, 4479–4496. https://doi.org/10.1029/js082i028p04479

Pollack, J.B., Colburn, D.S., Flasar, F.M., Kahn, R., Carlston, C.E., Pidek, D., 1979. Properties and effects of dust particles suspended in the Martian atmosphere. J Geophys Res Solid Earth 84, 2929–2945. https://doi.org/10.1029/jb084ib06p02929

Pollack, J.B., Ockert-Bell, M.E., Shepard, M.K., 1995. Viking Lander image analysis of Martian atmospheric dust. J Geophys Res Planets 100, 5235–5250. https://doi.org/10.1029/94je02640

Porch, W.M., Gillette, D.A., 1977. A Comparison of Aerosol and Momentum Mixing in Dust Storms Using Fast-Response Instruments. J Appl Meteorol 16, 1273–1281. https://doi.org/10.1175/1520-0450(1977)016<;1273:acoaam>2.0.co;2

Prospero, J.M., Bonatti, E., Schubert, C., Carlson, T.N., 1970. Dust in the Caribbean atmosphere traced to an African dust storm. Earth Planet Sc Lett 9, 287–293. https://doi.org/10.1016/0012-821x(70)90039-7

Prospero, J.M., Ginoux, P., Torres, O., Nicholson, S.E., Gill, T.E., 2002. ENVIRONMENTAL CHARACTERIZATION OF GLOBAL SOURCES OF ATMOSPHERIC SOIL DUST IDENTIFIED WITH THE NIMBUS 7 TOTAL OZONE MAPPING SPECTROMETER (TOMS) ABSORBING AEROSOL PRODUCT. Rev Geophys 40, 2-1-2–31. https://doi.org/10.1029/2000rg000095

Pu, B., Ginoux, P., 2018. How reliable are CMIP5 models in simulating dust optical depth? Atmos Chem Phys 18, 12491–12510. https://doi.org/10.5194/acp-18-12491-2018

Purcell, E.M., Pennypacker, C.R., 1973. Scattering and Absorption of Light by Nonspherical Dielectric Grains. Astrophysical J 186, 705. https://doi.org/10.1086/152538

Rafkin, S.C.R., Maria, M.R.V.S., Michaels, T.I., 2002. Simulation of the atmospheric thermal circulation of a martian volcano using a mesoscale numerical model. Nature 419, 697–699. https://doi.org/10.1038/nature01114

Räisänen, P., Haapanala, P., Chung, C.E., Kahnert, M., Makkonen, R., Tonttila, J., Nousiainen, T., 2013. Impact of dust particle non-sphericity on climate simulations. Q J Roy Meteor Soc 139, 2222–2232. https://doi.org/10.1002/qj.2084

Reid, E.A., Reid, J.S., Meier, M.M., Dunlap, M.R., Cliff, S.S., Broumas, A., Perry, K., Maring, H., 2003. Characterization of African dust transported to Puerto Rico by individual particle and size segregated bulk analysis. J Geophys Res Atmospheres 1984 2012 108. https://doi.org/10.1029/2002jd002935

Reid, J.S., Jonsson, H.H., Maring, H.B., Smirnov, A., Savoie, D.L., Cliff, S.S., Reid, E.A., Livingston, J.M., Meier, M.M., Dubovik, O., Tsay, S., 2003a. Comparison of size and morphological measurements of coarse mode dust particles from Africa. J. Geophys. Res.: Atmos. 108. https://doi.org/10.1029/2002jd002485

Reid, J.S., Kinney, J.E., Westphal, D.L., Holben, B.N., Welton, E.J., Tsay, S., Eleuterio, D.P., Campbell, J.R., Christopher, S.A., Colarco, P.R., Jonsson, H.H., Livingston, J.M., Maring, H.B., Meier, M.L., Pilewskie, P., Prospero, J.M., Reid, E.A., Remer, L.A., Russell, P.B., Savoie, D.L., Smirnov, A., Tanré, D., 2003b. Analysis of measurements of Saharan dust by airborne and ground-based remote sensing methods during the Puerto Rico Dust Experiment (PRIDE). J Geophys Res Atmospheres 1984 2012 108. https://doi.org/10.1029/2002jd002493

Reid, J.S., Reid, E.A., Walker, A., Piketh, S., Cliff, S., Mandoos, A.A., Tsay, S., Eck, T.F., 2008. Dynamics of southwest Asian dust particle size characteristics with implications for global dust research. J Geophys Res Atmospheres 113. https://doi.org/10.1029/2007jd009752

Remer, L.A., Kaufman, Y.J., 1998. Dynamic aerosol model: Urban/industrial aerosol. J Geophys Res Atmospheres 103, 13859–13871. https://doi.org/10.1029/98jd00994

Remer, L.A., Levy, R.C., Mattoo, S., Tanré, D., Gupta, P., Shi, Y., Sawyer, V., Munchak, L.A., Zhou, Y., Kim, M., Ichoku, C., Patadia, F., Li, R.-R., Gassó, S., Kleidman, R.G., Holben, B.N., 2020. The Dark Target Algorithm for Observing the Global Aerosol System: Past, Present, and Future. Remote Sens-basel 12, 2900. https://doi.org/10.3390/rs12182900

Richardson, M.I., Toigo, A.D., Newman, C.E., 2007. PlanetWRF: A general purpose, local to global numerical model for planetary atmospheric and climate dynamics. J Geophys Res Planets 1991 2012 112. https://doi.org/10.1029/2006je002825

Ridgwell, A.J., 2002. Dust in the Earth system: the biogeochemical linking of land, air and sea. Philosophical Transactions Royal Soc Lond Ser Math Phys Eng Sci 360, 2905–2924. https://doi.org/10.1098/rsta.2002.1096

Rocha-Lima, A., Martins, J.V., Remer, L.A., Todd, M., Marsham, J.H., Engelstaedter, S., Ryder, C.L., Cavazos-Guerra, C., Artaxo, P., Colarco, P., Washington, R., 2018. A detailed characterization of the Saharan dust collected during the Fennec campaign in 2011: in situ ground-based and laboratory measurements. Atmos Chem Phys 18, 1023–1043. https://doi.org/10.5194/acp-18-1023-2018

Rosenberg, P.D., Dean, A.R., Williams, P.I., Dorsey, J.R., Minikin, A., Pickering, M.A., Petzold, A., 2012. Particle sizing calibration with refractive index correction for light scattering optical particle counters and impacts upon PCASP and CDP data collected during the Fennec campaign. Atmos Meas Tech 5, 1147–1163. https://doi.org/10.5194/amt-5-1147-2012

Rosenberg, P.D., Parker, D.J., Ryder, C.L., Marsham, J.H., Garcia-Carreras, L., Dorsey, J.R., Brooks, I.M., Dean, A.R., Crosier, J., McQuaid, J.B., Washington, R., 2014. Quantifying particle size and turbulent scale dependence of dust flux in the Sahara using aircraft measurements. J Geophys Res Atmospheres 119, 7577–7598. https://doi.org/10.1002/2013jd021255

Ruff, S.W., Christensen, P.R., 2002. Bright and dark regions on Mars: Particle size and mineralogical characteristics based on Thermal Emission Spectrometer data. J Geophys Res Planets 1991 2012 107, 2-1-2–22. https://doi.org/10.1029/2001je001580

Ryder, C.L., Highwood, E.J., Lai, T.M., Sodemann, H., Marsham, J.H., 2013a. Impact of atmospheric transport on the evolution of microphysical and optical properties of Saharan dust. Geophys Res Lett 40, 2433–2438. https://doi.org/10.1002/grl.50482

Ryder, C.L., Highwood, E.J., Rosenberg, P.D., Trembath, J., Brooke, J.K., Bart, M., Dean, A., Crosier, J., Dorsey, J., Brindley, H., Banks, J., Marsham, J.H., McQuaid, J.B., Sodemann, H., Washington, R., 2013b. Optical properties of Saharan dust aerosol and contribution from the coarse mode as measured during the Fennec 2011 aircraft campaign. Atmos Chem Phys 13, 303–325. https://doi.org/10.5194/acp-13-303-2013

Ryder, C.L., Highwood, E.J., Walser, A., Seibert, P., Philipp, A., Weinzierl, B., 2019. Coarse and giant particles are ubiquitous in Saharan dust export regions and are radiatively significant over the Sahara. Atmos Chem Phys 19, 15353–15376. https://doi.org/10.5194/acp-19-15353-2019

Ryder, C.L., Marenco, F., Brooke, J.K., Estelles, V., Cotton, R., Formenti, P., McQuaid, J.B., Price, H.C., Liu, D., Ausset, P., Rosenberg, P.D., Taylor, J.W., Choularton, T., Bower, K., Coe, H., Gallagher, M., Crosier, J., Lloyd, G., Highwood, E.J., Murray, B.J., 2018. Coarse-mode mineral dust size distributions, composition and optical properties from AER-D aircraft measurements over the tropical eastern Atlantic. Atmos Chem Phys 18, 17225–17257. https://doi.org/10.5194/acp-18-17225-2018

Sadrian, M.R., Calvin, W.M., McCormack, J., 2022. Contrasting mineral dust abundances from X-ray diffraction and reflectance spectroscopy. Atmos Meas Tech 15, 3053–3074. https://doi.org/10.5194/amt-15-3053-2022

Sadrian, M.R., Calvin, W.M., Perrin, A.E., Engelbrecht, J.P., Moosmüller, H., 2023. Variations in Infrared Complex Refractive Index Spectra of Surface Soils from Global Dust Entrainment Regions. Atmosphere-basel 14, 675. https://doi.org/10.3390/atmos14040675

Saito, M., Yang, P., 2022. Generalization of Atmospheric Nonspherical Particle Size: Interconversions of Size Distributions and Optical Equivalence. J. Atmos. Sci. 79, 3333–3349. https://doi.org/10.1175/jas-d-22-0086.1

Saito, M., Yang, P., 2021. Advanced Bulk Optical Models Linking the Backscattering and Microphysical Properties of Mineral Dust Aerosol. Geophys Res Lett 48. https://doi.org/10.1029/2021gl095121

Saito, M., Yang, P., Ding, J., Liu, X., 2021. A comprehensive database of the optical properties of irregular aerosol particles for radiative transfer simulations. J Atmos Sci. https://doi.org/10.1175/jas-d-20-0338.1

Salomonson, V.V., Barnes, W., Xiong, J., Kempler, S., Masuoka, E., 2002. An Overview of the Earth Observing System MODIS Instrument and Associated Data Systems Performance. Ieee Int Geoscience Remote Sens Symposium 2, 1174–1176. https://doi.org/10.1109/igarss.2002.1025812

Samset, B.H., Stjern, C.W., Andrews, E., Kahn, R.A., Myhre, G., Schulz, M., Schuster, G.L., 2018. Aerosol Absorption: Progress Towards Global and Regional Constraints. Curr Clim Change Reports 4, 65–83. https://doi.org/10.1007/s40641-018-0091-4

Sassen, K., 2002. Indirect climate forcing over the western US from Asian dust storms. Geophys Res Lett 29, 103-1-103–4. https://doi.org/10.1029/2001gl014051

Sawyer, V., Levy, R.C., Mattoo, S., Cureton, G., Shi, Y., Remer, L.A., 2020. Continuing the MODIS Dark Target Aerosol Time Series with VIIRS. Remote Sens-basel 12, 308. https://doi.org/10.3390/rs12020308

Sayer, A.M., Hsu, N.C., Bettenhausen, C., Ahmad, Z., Holben, B.N., Smirnov, A., Thomas, G.E., Zhang, J., 2012. SeaWiFS Ocean Aerosol Retrieval (SOAR): Algorithm, validation, and comparison with other data sets. J Geophys Res Atmospheres 1984 2012 117, n/a-n/a. https://doi.org/10.1029/2011jd016599

Sayer, A.M., Hsu, N.C., Lee, J., Bettenhausen, C., Kim, W.V., Smirnov, A., 2017. Satellite Ocean Aerosol Retrieval (SOAR) algorithm extension to S-NPP VIIRS as part of the "Deep Blue" aerosol project. J Geophys Res Atmospheres Jgr 123, 380–400. https://doi.org/10.1002/2017jd027412

Scanza, R.A., Mahowald, N., Ghan, S., Zender, C.S., Kok, J.F., Liu, X., Zhang, Y., Albani, S., 2015. Modeling dust as component minerals in the Community Atmosphere Model: development of framework and impact on radiative forcing. Atmos Chem Phys 15, 537–561. https://doi.org/10.5194/acp-15-537-2015

Schepanski, K., 2018. Transport of Mineral Dust and Its Impact on Climate. Geosciences 8, 151. https://doi.org/10.3390/geosciences8050151

Scheuvens, D., Kandler, K., 2014. Mineral Dust, A Key Player in the Earth System 15–49. https://doi.org/10.1007/978-94-017-8978-3_2

Scheuvens, D., Schütz, L., Kandler, K., Ebert, M., Weinbruch, S., 2013. Bulk composition of northern African dust and its source sediments — A compilation. Earth-sci Rev 116, 170–194. https://doi.org/10.1016/j.earscirev.2012.08.005

Schulz, M., Textor, C., Kinne, S., Balkanski, Y., Bauer, S., Berntsen, T., Berglen, T., Boucher, O., Dentener, F., Guibert, S., Isaksen, I.S.A., Iversen, T., Koch, D., Kirkevåg, A., Liu, X., Montanaro, V., Myhre, G., Penner, J.E., Pitari, G., Reddy, S., Seland, Ø., Stier, P., Takemura, T., 2006. Radiative forcing by aerosols as derived from the AeroCom present-day and pre-industrial simulations. Atmos Chem Phys 6, 5225–5246. https://doi.org/10.5194/acp-6-5225-2006

Schuster, G.L., Dubovik, O., Arola, A., 2016. Remote sensing of soot carbon – Part 1: Distinguishing different absorbing aerosol species. Atmos Chem Phys 16, 1565–1585. https://doi.org/10.5194/acp-16-1565-2016

Schuster, G.L., Espinosa, W.R., Ziemba, L.D., Beyersdorf, A.J., Rocha-Lima, A., Anderson, B.E., Martins, J.V., Dubovik, O., Ducos, F., Fuertes, D., Lapyonok, T., Shook, M., Derimian, Y., Moore, R.H., 2019. A Laboratory Experiment for the Statistical Evaluation of Aerosol Retrieval (STEAR) Algorithms. Remote Sens-basel 11, 498. https://doi.org/10.3390/rs11050498

Schuster, G.L., Vaughan, M., MacDonnell, D., Su, W., Winker, D., Dubovik, O., Lapyonok, T., Trepte, C., 2012. Comparison of CALIPSO aerosol optical depth retrievals to AERONET measurements, and a climatology for the lidar ratio of dust. Atmos Chem Phys 12, 7431–7452. https://doi.org/10.5194/acp-12-7431-2012

Schütz, L., 1980. Long Range Transport of Desert Dust With Special Emphasis on the Sahara. Ann Ny Acad Sci 338, 515–532. https://doi.org/10.1111/j.1749-6632.1980.tb17144.x

Shao, Y., 2001. A model for mineral dust emission. J Geophys Res Atmospheres 106, 20239–20254. https://doi.org/10.1029/2001jd900171

Shao, Y., Ishizuka, M., Mikami, M., Leys, J.F., 2011. Parameterization of size-resolved dust emission and validation with measurements. J Geophys Res Atmospheres 1984 2012 116. https://doi.org/10.1029/2010jd014527

Shao, Y., Raupach, M., 1993. Effect of Saltation Bombardment on the Entrainment of Dust by Wind. Journal Of Geophysical Research-Atmospheres 98, 12719 12726.

Shao, Yaping, Wyrwoll, K.-H., Chappell, A., Huang, J., Lin, Z., McTainsh, G.H., Mikami, M., Tanaka, T.Y., Wang, X., Yoon, S., 2011. Dust cycle: An emerging core theme in Earth system science. Aeolian Res 2, 181–204. https://doi.org/10.1016/j.aeolia.2011.02.001

Sinyuk, A., Holben, B.N., Eck, T.F., Giles, D.M., Slutsker, I., Korkin, S., Schafer, J.S., Smirnov, A., Sorokin, M., Lyapustin, A., 2020. The AERONET Version 3 aerosol retrieval algorithm, associated uncertainties and comparisons to Version 2. Atmos Meas Tech 13, 3375–3411. https://doi.org/10.5194/amt-13-3375-2020

Sinyuk, A., Torres, O., Dubovik, O., 2003. Combined use of satellite and surface observations to infer the imaginary part of refractive index of Saharan dust. Geophys Res Lett 30. https://doi.org/10.1029/2002gl016189

Skiles, S.M., Flanner, M., Cook, J.M., Dumont, M., Painter, T.H., 2018. Radiative forcing by light-absorbing particles in snow. Nat. Clim. Chang. 8, 964–971. https://doi.org/10.1038/s41558-018-0296-5

Smith, I.B., Putzig, N.E., Holt, J.W., Phillips, R.J., 2016. An ice age recorded in the polar deposits of Mars. Science 352, 1075–1078. https://doi.org/10.1126/science.aad6968

Smith, M.D., 2009. THEMIS observations of Mars aerosol optical depth from 2002–2008. Icarus 202, 444–452. https://doi.org/10.1016/j.icarus.2009.03.027

Smith, M.D., 2008. Spacecraft Observations of the Martian Atmosphere*. Annu Rev Earth Pl Sc 36, 191–219. https://doi.org/10.1146/annurev.earth.36.031207.124334

Smith, M.D., 2004. Interannual variability in TES atmospheric observations of Mars during 1999–2003. Icarus 167, 148–165. https://doi.org/10.1016/j.icarus.2003.09.010

Sobanska, S., Hwang, H., Choël, M., Jung, H.-J., Eom, H.-J., Kim, H., Barbillat, J., Ro, C.-U., 2012. Investigation of the Chemical Mixing State of Individual Asian Dust Particles by the Combined Use of Electron Probe X-ray Microanalysis and Raman Microspectrometry. Anal Chem 84, 3145–3154. https://doi.org/10.1021/ac2029584

Sofiev, M., Vira, J., Kouznetsov, R., Prank, M., Soares, J., Genikhovich, E., 2015. Construction of the SILAM Eulerian atmospheric dispersion model based on the advection algorithm of Michael Galperin. Geosci Model Dev 8, 3497–3522. https://doi.org/10.5194/gmd-8-3497-2015

Sokolik, I.N., Toon, O.B., 1999. Incorporation of mineralogical composition into models of the radiative properties of mineral aerosol from UV to IR wavelengths. J Geophys Res Atmospheres 104, 9423–9444. https://doi.org/10.1029/1998jd200048

Song, Q., Zhang, Z., Yu, H., Kok, J.F., Di Biagio, C., Albani, S., Zheng, J., Ding, J., 2022. Size-resolved dust direct radiative effect efficiency derived from satellite observations. Atmos. Chem. Phys. 22, 13115–13135. https://doi.org/10.5194/acp-22-13115-2022

Sorensen, C.M., 2001. Light Scattering by Fractal Aggregates: A Review. Aerosol Sci Tech 35, 648–687. https://doi.org/10.1080/02786820117868

Sorensen, C.M., Maughan, J.B., Moosmüller, H., 2019. Spherical particle absorption over a broad range of imaginary refractive index. J Quantitative Spectrosc Radiat Transf 226, 81–86. https://doi.org/10.1016/j.jqsrt.2019.01.011

Sow, M., Alfaro, S.C., Rajot, J.L., Marticorena, B., 2009. Size resolved dust emission fluxes measured in Niger during 3 dust storms of the AMMA experiment. Atmos Chem Phys 9, 3881–3891. https://doi.org/10.5194/acp-9-3881-2009

Stamnes, K., Thomas, G.E., Stamnes, J.J., 2017. Radiative Transfer in the Atmosphere and Ocean. Cambridge University Press. https://doi.org/10.1017/9781316148549

Sugimoto, N., Huang, Z., 2014. Lidar methods for observing mineral dust. J Meteorol Res-prc 28, 173–184. https://doi.org/10.1007/s13351-014-3068-9

Sumlin, B.J., Heinson, W.R., Chakrabarty, R.K., 2018. Retrieving the aerosol complex refractive index using PyMieScatt: A Mie computational package with visualization capabilities. J Quantitative Spectrosc Radiat Transf 205, 127–134. https://doi.org/10.1016/j.jqsrt.2017.10.012

Taflove, A., Hagness, S., 2005. Computational Electrodynamics: The Finite-Difference Time-Domain Method, Third Edition. Artech House Publishers.

Tegen, I., Fung, I., 1994. Modeling of Mineral Dust in the Atmosphere - Sources, Transport, and Optical-Thickness. Journal Of Geophysical Research-Atmospheres 99, 22897 22914.

Tegen, I., Lacis, AA., 1996. Modeling of particle size distribution and its influence on the radiative properties of mineral dust aerosol. Journal Of Geophysical Research-Atmospheres 101, 19237 19244.

Tegen, I., Miller, R., 1998. A general circulation model study on the interannual variability of soil dust aerosol. J Geophys Res Atmospheres 103, 25975–25995. https://doi.org/10.1029/98jd02345

Textor, C., Schulz, M., Guibert, S., Kinne, S., Balkanski, Y., Bauer, S., Berntsen, T., Berglen, T., Boucher, O., Chin, M., Dentener, F., Diehl, T., Easter, R., Feichter, H., Fillmore, D., Ghan, S., Ginoux, P., Gong, S., Grini, A., Hendricks, J., Horowitz, L., Huang, P., Isaksen, I., Iversen, I., Kloster, S., Koch, D., Kirkevåg, A., Kristjansson, J.E., Krol, M., Lauer, A., Lamarque, J.F., Liu, X., Montanaro, V., Myhre, G., Penner, J., Pitari, G., Reddy, S., Seland, Ø., Stier, P., Takemura, T., Tie, X., 2006. Analysis and quantification of the diversities of aerosol life cycles within AeroCom. Atmos Chem Phys 6, 1777–1813. https://doi.org/10.5194/acp-6-1777-2006

Thomas, P., Gierasch, P.J., 1985. Dust Devils on Mars. Science 230, 175–177. https://doi.org/10.1126/science.230.4722.175

Todd, M.C., Washington, R., Martins, J.V., Dubovik, O., Lizcano, G., M'Bainayel, S., Engelstaedter, S., 2007. Mineral dust emission from the Bodélé Depression, northern Chad, during BoDEx 2005. J Geophys Res Atmospheres 1984 2012 112. https://doi.org/10.1029/2006jd007170

Tomasko, M.G., Doose, L.R., Lemmon, M., Smith, P.H., Wegryn, E., 1999. Properties of dust in the Martian atmosphere from the Imager on Mars Pathfinder. J Geophys Res Planets 104, 8987–9007. https://doi.org/10.1029/1998je900016

Tong, D.Q., Gorris, M.E., Gill, T.E., Ardon-Dryer, K., Wang, J., Ren, L., 2022. Dust Storms, Valley Fever, and Public Awareness. Geohealth 6, e2022GH000642. https://doi.org/10.1029/2022gh000642

Toon, O.B., Ackerman, T.P., 1981. Algorithms for the calculation of scattering by stratified spheres. Appl Optics 20, 3657. https://doi.org/10.1364/ao.20.003657

Torres, O., Ahn, C., Chen, Z., 2013. Improvements to the OMI near-UV aerosol algorithm using A-train CALIOP and AIRS observations. Atmos Meas Tech 6, 3257–3270. https://doi.org/10.5194/amt-6-3257-2013

Torres, O., Bhartia, P.K., Jethva, H., Ahn, C., 2018. Impact of the ozone monitoring instrument row anomaly on the long-term record of aerosol products. Atmos Meas Tech 11, 2701–2715. https://doi.org/10.5194/amt-11-2701-2018

Torres, O., Jethva, H., Ahn, C., Jaross, G., Loyola, D.G., 2020. TROPOMI aerosol products: evaluation and observations of synoptic-scale carbonaceous aerosol plumes during 2018–2020. Atmos Meas Tech 13, 6789–6806. https://doi.org/10.5194/amt-13-6789-2020

Torres, O., Tanskanen, A., Veihelmann, B., Ahn, C., Braak, R., Bhartia, P.K., Veefkind, P., Levelt, P., 2007. Aerosols and surface UV products from Ozone Monitoring Instrument observations: An overview. J Geophys Res Atmospheres 1984 2012 112. https://doi.org/10.1029/2007jd008809

Trochkine, D., Iwasaka, Y., Matsuki, A., Yamada, M., Kim, Y. -S., Nagatani, T., Zhang, D., Shi, G. -Y., Shen, Z., 2003. Mineral aerosol particles collected in Dunhuang, China, and their comparison with chemically modified particles collected over Japan. J Geophys Res Atmospheres 108. https://doi.org/10.1029/2002jd003268

Tyler, D., Barnes, J.R., 2015. Convergent crater circulations on Mars: Influence on the surface pressure cycle and the depth of the convective boundary layer. Geophys Res Lett 42, 7343–7350. https://doi.org/10.1002/2015gl064957

Ulanowski, Z., Bailey, J., Lucas, P.W., Hough, J.H., Hirst, E., 2007. Alignment of atmospheric mineral dust due to electric field. Atmos Chem Phys 7, 6161–6173. https://doi.org/10.5194/acp-7-6161-2007

Vaughan, M., Liu, Z., Hu, Y.-X., Powell, K., Omar, A., Rodier, S., Hunt, W., Kar, J., Tackett, J., Getzewich, B., Lee, K.-P., 2015. Cloud-Aerosol Interactions: Retrieving Aerosol Ångstrom Exponents From CALIPSO Measurements of Opaque Water Clouds.

Veihelmann, B., Nousiainen, T., Kahnert, M., Zande, W.J. van der, 2006. Light scattering by small feldspar particles simulated using the Gaussian random sphere geometry. J Quantitative Spectrosc Radiat Transf 100, 393–405. https://doi.org/10.1016/j.jqsrt.2005.11.053

Vermote, E.F., Kotchenova, S., 2008. Atmospheric correction for the monitoring of land surfaces. J Geophys Res Atmospheres 1984 2012 113. https://doi.org/10.1029/2007jd009662

Vilaplana, R., Moreno, F., Molina, A., 2006. Study of the sensitivity of size-averaged scattering matrix elements of nonspherical particles to changes in shape, porosity and refractive index. J Quantitative Spectrosc Radiat Transf 100, 415–428. https://doi.org/10.1016/j.jqsrt.2005.11.068

Volz, F.E., 1973. Infrared Optical Constants of Ammonium Sulfate, Sahara Dust, Volcanic Pumice, and Flyash. Appl Optics 12, 564. https://doi.org/10.1364/ao.12.000564

Voss, K.K., Evan, A.T., 2019. A new satellite-based global climatology of dust aerosol optical depth A new satellite-based global climatology of dust aerosol optical depth. J Appl Meteorol Clim 59, 83–102. https://doi.org/10.1175/jamc-d-19-0194.1

Warren, S.G., Roesler, C.S., Brandt, R.E., Curran, M., 2019. Green Icebergs Revisited. J Geophys Res Oceans 124, 925–938. https://doi.org/10.1029/2018jc014479

Washington, R., Flamant, C., Parker, D., Marsham, J., Mc-Quaid, J., Brindley, H., Todd, M., Highwood, E., Ryder, C., Chaboureau, J.P., Kocha, C., Bechir, M., Saci, A., 2012. Fennec - The Saharan Climate System. CLIVAR Exchanges 69, 31–32.

Waterman, P.C., 1965. Matrix formulation of electromagnetic scattering. P Ieee 53, 805–812. https://doi.org/10.1109/proc.1965.4058

Watson, J.G., Chow, J.C., Frazier, C.A., 1999. Fluorescence Analysis of Ambient Air Samples, in: Landsberger, S., Creatchman, M. (Eds.), Gordon and Breach Science. pp. 67–96.

Wei, J., Li, Z., Peng, Y., Sun, L., 2019. MODIS Collection 6.1 aerosol optical depth products over land and ocean: validation and comparison. Atmos Environ 201, 428–440. https://doi.org/10.1016/j.atmosenv.2018.12.004

Weiden, S.-L. von der, Drewnick, F., Borrmann, S., 2009. Particle Loss Calculator – a new software tool for the assessment of the performance of aerosol inlet systems. Atmos Meas Tech 2, 479–494. https://doi.org/10.5194/amt-2-479-2009

Weinzierl, B., Ansmann, A., Prospero, J.M., Althausen, D., Benker, N., Chouza, F., Dollner, M., Farrell, D., Fomba, W.K., Freudenthaler, V., Gasteiger, J., Groß, S., Haarig, M., Heinold, B., Kandler, K., Kristensen, T.B., Mayol-Bracero, O.L., Müller, T., Reitebuch, O., Sauer, D., Schäfler, A., Schepanski, K., Spanu, A., Tegen, I., Toledano, C., Walser, A., 2017. The Saharan Aerosol Long-range Transport and Aerosol-Cloud-Interaction Experiment (SALTRACE): overview and selected highlights. B Am Meteorol Soc 98, 1427–1451. https://doi.org/10.1175/bams-d-15-00142.1

Westphal, D., Toon, O., Carlson, T., 1988. A Cast-Study of Mobilization and Transport of Saharan Dust. Journal Of The Atmospheric Sciences 45, 2145 2175.

Westphal, D., Toon, O., Carlson, T., 1987. A Two-Dimensional Numerical Investigation of the Dynamics and Microphysics of Saharan Dust Storms. Journal Of Geophysical Research-Atmospheres 92, 3027 3049.

Wiegner, M., Gasteiger, J., Kandler, K., Weinzierl, B., Rasp, K., Esselborn, M., Freudenthaler, V., Heese, B., Toledano, C., Tesche, M., Althausen, D., 2009. Numerical simulations of optical properties of Saharan dust aerosols with emphasis on lidar applications. Tellus B 61, 180–194. https://doi.org/10.1111/j.1600-0889.2008.00381.x

Winker, D.M., Vaughan, M.A., Omar, A., Hu, Y., Powell, K.A., Liu, Z., Hunt, W.H., Young, S.A., 2009. Overview of the CALIPSO Mission and CALIOP Data Processing Algorithms. J Atmos Ocean Tech 26, 2310–2323. https://doi.org/10.1175/2009jtecha1281.1

Wiscombe, W.J., 1980. Improved Mie scattering algorithms. Appl Optics 19, 1505. https://doi.org/10.1364/ao.19.001505

Wolff, M., Lopéz-Valverde, M., Madeleine, J., Wilson, R., Smith, M., Fouchet, T., Delory, G., 2017. Radiative Process: Techniques and Applications, in: Haberle, R., Clancy, R., Forget, F., Smith, M., Zurek, R. (Eds.), The Atmosphere and Climate of Mars. Cambridge University Press, Cambridge, pp. 106–171. https://doi.org/10.1017/9781139060172.006

Wolff, M.J., Smith, M.D., Clancy, R.T., Arvidson, R., Kahre, M., Seelos, F., Murchie, S., Savijärvi, H., 2009. Wavelength dependence of dust aerosol single scattering albedo as observed by the Compact Reconnaissance Imaging Spectrometer. J Geophys Res Planets 1991 2012 114. https://doi.org/10.1029/2009je003350

Wolff, M.J., Smith, M.D., Clancy, R.T., Spanovich, N., Whitney, B.A., Lemmon, M.T., Bandfield, J.L., Banfield, D., Ghosh, A., Landis, G., Christensen, P.R., Bell, J.F., Squyres, S.W., 2006. Constraints on dust aerosols from the Mars Exploration Rovers using MGS overflights and Mini-TES. J Geophys Res Planets 1991 2012 111, n/a-n/a. https://doi.org/10.1029/2006je002786

Wolkenberg, P., Giuranna, M., Grassi, D., Aronica, A., Aoki, S., Scaccabarozzi, D., Saggin, B., 2018. Characterization of dust activity on Mars from MY27 to MY32 by PFS-MEX observations. Icarus 310, 32–47. https://doi.org/10.1016/j.icarus.2017.10.045

Woodward, S., 2001. Modeling the atmospheric life cycle and radiative impact of mineral dust in the Hadley Centre climate model. Journal Of Geophysical Research-Atmospheres 106, 18155 18166.

Wu, M., Liu, X., Yang, K., Luo, T., Wang, Z., Wu, C., Zhang, K., Yu, H., Darmenov, A., 2019. Modeling Dust in East Asia by CESM and Sources of Biases. J Geophys Res Atmospheres 124, 8043–8064. https://doi.org/10.1029/2019jd030799

Xian, P., Reid, J.S., Hyer, E.J., Sampson, C.R., Rubin, J.I., Ades, M., Asencio, N., Basart, S., Benedetti, A., Bhattacharjee, P.S., Brooks, M.E., Colarco, P.R., Silva, A.M. da, Eck, T.F., Guth, J., Jorba, O., Kouznetsov, R., Kipling, Z., Sofiev, M., Garcia-Pando, C.P., Pradhan, Y., Tanaka, T., Wang, J., Westphal, D.L., Yumimoto, K., Zhang, J., 2019. Current state of the global operational aerosol multi-model ensemble: An update from the International Cooperative for Aerosol Prediction (ICAP). Q J Roy Meteor Soc. https://doi.org/10.1002/qj.3497

Xie, Y., Li, Z., Li, L., Wang, L., Li, D., Chen, C., Li, K., Xu, H., 2014. Study on influence of different mixing rules on the aerosol components retrieval from ground-based remote sensing measurements. Atmos Res 145, 267–278. https://doi.org/10.1016/j.atmosres.2014.04.006

Yang, A., Tan, Q., Rajapakshe, C., Chin, M., Yu, H., 2022. Global premature mortality by dust and pollution PM2.5 estimated from aerosol reanalysis of the modern-era retrospective analysis for research and applications, version 2. Frontiers Environ Sci 10, 975755. https://doi.org/10.3389/fenvs.2022.975755

Yang, P., Ding, J., Panetta, R.L., Liou, K.-N., Kattawar, G.W., Mishchenko, M., 2019. On the Convergence of Numerical Computations for Both Exact and Approximate Solutions for Electromagnetic Scattering by Nonspherical Dielectric Particles. Electromagn Waves Camb Mass 164, 27–61.

Yang, P., Feng, Q., Hong, G., Kattawar, G.W., Wiscombe, W.J., Mishchenko, M.I., Dubovik, O., Laszlo, I., Sokolik, I.N., 2007. Modeling of the scattering and radiative properties of nonspherical dust-like aerosols. J Aerosol Sci 38, 995–1014. https://doi.org/10.1016/j.jaerosci.2007.07.001

Yang, P., Liou, K.N., 1996. Geometric-optics-integral-equation method for light scattering by nonspherical ice crystals. Appl Optics 35, 6568–84. https://doi.org/10.1364/ao.35.006568

Yang, P., Liou, K.N., Mishchenko, M.I., Gao, B.C., 2000. Efficient finite-difference time-domain scheme for light scattering by dielectric particles: application to aerosols. Appl Optics 39, 3727–37. https://doi.org/10.1364/ao.39.003727

Yasunari, T.J., Koster, R.D., Lau, W.K.M., Kim, K., 2015. Impact of snow darkening via dust, black carbon, and organic carbon on boreal spring climate in the Earth system. J Geophys Res Atmospheres 120, 5485–5503. https://doi.org/10.1002/2014jd022977

Yee, K., 1966. Numerical solution of initial boundary value problems involving maxwell's equations in isotropic media. Ieee T Antenn Propag 14, 302–307. https://doi.org/10.1109/tap.1966.1138693

Yi, B., Hsu, C.N., Yang, P., Tsay, S.-C., 2011. Radiative transfer simulation of dust-like aerosols: Uncertainties from particle shape and refractive index. J Aerosol Sci 42, 631–644. https://doi.org/10.1016/j.jaerosci.2011.06.008

Yingst, R.A., Bray, S., Herkenhoff, K., Lemmon, M., Minitti, M.E., Schmidt, M.E., Edgett, K.S., Fey, D.M., Kah, L.C., 2020. Dust cover on Curiosity's Mars Hand Lens Imager (MAHLI) calibration target: Implications for deposition and removal mechanisms. Icarus 351, 113872. https://doi.org/10.1016/j.icarus.2020.113872

Yorks, J.E., McGill, M.J., Palm, S.P., Hlavka, D.L., Selmer, P.A., Nowottnick, E.P., Vaughan, M.A., Rodier, S.D., Hart, W.D., 2016. An overview of the CATS level 1 processing algorithms and data products: CATS Data Products and Algorithms. Geophys Res Lett 43, 4632–4639. https://doi.org/10.1002/2016gl068006

Yoshioka, M., Mahowald, N.M., Conley, A.J., Collins, W.D., Fillmore, D.W., Zender, C.S., Coleman, D.B., 2007. Impact of Desert Dust Radiative Forcing on Sahel Precipitation: Relative Importance of Dust Compared to Sea Surface Temperature Variations, Vegetation Changes, and Greenhouse Gas Warming. J. Clim. 20, 1445–1467. https://doi.org/10.1175/jcli4056.1

Young, S.A., Vaughan, M.A., 2009. The Retrieval of Profiles of Particulate Extinction from Cloud-Aerosol Lidar Infrared Pathfinder Satellite Observations (CALIPSO) Data: Algorithm Description. J Atmos Ocean Tech 26, 1105–1119. https://doi.org/10.1175/2008jtecha1221.1

Yu, H., Chin, M., Bian, H., Yuan, T., Prospero, J.M., Omar, A.H., Remer, L.A., Winker, D.M., Yang, Y., Zhang, Y., Zhang, Z., 2015. Quantification of trans-Atlantic dust transport from seven-year (2007–2013) record of CALIPSO lidar measurements. Remote Sens Environ 159, 232–249. https://doi.org/10.1016/j.rse.2014.12.010

Yu, H., Kaufman, Y.J., Chin, M., Feingold, G., Remer, L.A., Anderson, T.L., Balkanski, Y., Bellouin, N., Boucher, O., Christopher, S., DeCola, P., Kahn, R., Koch, D., Loeb, N., Reddy, M.S., Schulz, M., Takemura, T., Zhou, M., 2006. A review of measurement-based assessments of the aerosol direct radiative effect and forcing. Atmos Chem Phys 6, 613–666. https://doi.org/10.5194/acp-6-613-2006

Yu, H., Tan, Q., Chin, M., Remer, L.A., Kahn, R.A., Bian, H., Kim, D., Zhang, Z., Yuan, T., Omar, A.H., Winker, D.M., Levy, R.C., Kalashnikova, O., Crepeau, L., Capelle, V., Chédin, A., 2019. Estimates of African Dust Deposition Along the Trans-Atlantic Transit Using the Decadelong Record of Aerosol Measurements from CALIOP, MODIS, MISR, and IASI. J Geophys Res Atmospheres 124, 7975–7996. https://doi.org/10.1029/2019jd030574

Yu, H., Tan, Q., Zhou, L., Zhou, Y., Bian, H., Chin, M., Ryder, C.L., Levy, R.C., Pradhan, Y., Shi, Y., Song, Q., Zhang, Z., Colarco, P.R., Kim, D., Remer, L.A., Yuan, T., Mayol-Bracero, O., Holben, B.N., 2021. Observation and modeling of the historic “Godzilla” African dust intrusion into the Caribbean Basin and the southern US in June 2020. Atmos Chem Phys 21, 12359–12383. https://doi.org/10.5194/acp-21-12359-2021

Yu, H., Yang, Y., Wang, H., Tan, Q., Chin, M., Levy, R.C., Remer, L.A., Smith, S.J., Yuan, T., Shi, Y., 2020. Interannual variability and trends of combustion aerosol and dust in major continental outflows revealed by MODIS retrievals and CAM5 simulations during 2003–2017. Atmos Chem Phys 20, 139–161. https://doi.org/10.5194/acp-20-139-2020

Yu, P., Toon, O.B., Bardeen, C.G., Mills, M.J., Fan, T., English, J.M., Neely, R.R., 2015. Evaluations of tropospheric aerosol properties simulated by the community earth system model with a sectional aerosol microphysics scheme. J Adv Model Earth Sy 7, 865–914. https://doi.org/10.1002/2014ms000421

Yurkin, M.A., Hoekstra, A.G., Brock, R.S., Lu, J.Q., 2007. Systematic comparison of the discrete dipole approximation and the finite difference time domain method for large dielectric scatterers. Opt Express 15, 17902. https://doi.org/10.1364/oe.15.017902

Zender, C., Bian, H., Newman, D., 2003. Mineral Dust Entrainment and Deposition (DEAD) model: Description and 1990s dust climatology. J Geophys Res Atmospheres 1984 2012 108, 4416. https://doi.org/10.1029/2002jd002775

Zhang, J., Reid, J.S., Westphal, D.L., Baker, N.L., Hyer, E.J., 2008. A system for operational aerosol optical depth data assimilation over global oceans. J Geophys Res Atmospheres 1984 2012 113. https://doi.org/10.1029/2007jd009065

Zhang, X.L., Wu, G.J., Zhang, C.L., Xu, T.L., Zhou, Q.Q., 2015. What is the real role of iron oxides in the optical properties of dust aerosols? Atmos Chem Phys 15, 12159–12177. https://doi.org/10.5194/acp-15-12159-2015

Zhang, Y., Mahowald, N., Scanza, R.A., Journet, E., Desboeufs, K., Albani, S., Kok, J.F., Zhuang, G., Chen, Y., Cohen, D.D., Paytan, A., Patey, M.D., Achterberg, E.P., Engelbrecht, J.P., Fomba, K.W., 2015. Modeling the global emission, transport and deposition of trace elements associated with mineral dust. Biogeosciences 12, 5771–5792. https://doi.org/10.5194/bg-12-5771-2015

Zhao, A., Ryder, C.L., Wilcox, L.J., 2022. How well do the CMIP6 models simulate dust aerosols? Atmos Chem Phys 22, 2095–2119. https://doi.org/10.5194/acp-22-2095-2022

Zheng, J., Zhang, Z., Garnier, A., Yu, H., Song, Q., Wang, C., Dubuisson, P., Di Biagio, C., 2022. The thermal infrared optical depth of mineral dust retrieved from integrated CALIOP and IIR observations. Remote Sens Environ 270, 112841. https://doi.org/10.1016/j.rse.2021.112841

Zheng, J., Zhang, Z., Yu, H., Garnier, A., Song, Q., Wang, C., Di Biagio, C., Kok, J.F., Derimian, Y., Ryder, C., 2023. Thermal infrared dust optical depth and coarse-mode effective diameter over oceans retrieved from collocated MODIS and CALIOP observations. Atmos. Chem. Phys. 23, 8271–8304. https://doi.org/10.5194/acp-23-8271-2023

Zhou, Y., Levy, R.C., Remer, L.A., Mattoo, S., Espinosa, W.R., 2020. Dust Aerosol Retrieval Over the Oceans With the MODIS/VIIRS Dark Target Algorithm: 2. Nonspherical Dust Model. Earth Space Sci 7. https://doi.org/10.1029/2020ea001222

Zong, R., Weng, F., Bi, L., Lin, X., Rao, C., Li, W., 2021. Impact of hematite on dust absorption at wavelengths ranging from 0.2 to 1.0 µm: an evaluation of literature data using the T-matrix method. Opt. express 29, 17405–17427. https://doi.org/10.1364/oe.427611

Zubko, E., Muinonen, K., Muñoz, O., Nousiainen, T., Shkuratov, Y., Sun, W., Videen, G., 2013. Light scattering by feldspar particles: Comparison of model agglomerate debris particles with laboratory samples. J Quantitative Spectrosc Radiat Transf 131, 175–187. https://doi.org/10.1016/j.jqsrt.2013.01.017

Zubko, E., Muinonen, K., Shkuratov, Y., Videen, G., Nousiainen, T., 2007. Scattering of light by roughened Gaussian random particles. J Quantitative Spectrosc Radiat Transf 106, 604–615. https://doi.org/10.1016/j.jqsrt.2007.01.050

Zubko, E., Shkuratov, Y., Mishchenko, M., Videen, G., 2008. Light scattering in a finite multi-particle system. J Quantitative Spectrosc Radiat Transf 109, 2195–2206. https://doi.org/10.1016/j.jqsrt.2008.03.007

Zubko, E., Videen, G., Arnold, J.A., MacCall, B., Weinberger, A.J., Shkuratov, Y., 2018. Interpolating light-scattering properties of irregularly shaped, absorbing particles. Opt Lett 43, 4308–4311. https://doi.org/10.1364/ol.43.004308